INFORMATION TO USERS

This material was produced from a microfilm copy of the original document. While the most advanced technological means to photograph and reproduce this document have been used, the quality is heavily dependent upon the quality of the original submitted.

The following explanation of techniques is provided to help you understand markings or patterns which may appear on this reproduction.

1. The sign or "target" for pages apparently lacking from the document photographed is "Missing Page(s)". If it was possible to obtain the missing page(s) or section, they are spliced into the film along with adjacent pages. This may have necessitated cutting thru an image and duplicating adjacent pages to insure you complete continuity.
2. When an image on the film is obliterated with a large round black mark, it is an indication that the photographer suspected that the copy may have moved during exposure and thus cause a blurred image. You will find a good image of the page in the adjacent frame.
3. When a map, drawing or chart, etc., was part of the material being photographed the photographer followed a definite method in "sectioning" the material. It is customary to begin photoing at the upper left hand corner of a large sheet and to continue photoing from left to right in equal sections with a small overlap. If necessary, sectioning is continued again – beginning below the first row and continuing on until complete.
4. The majority of users indicate that the textual content is of greatest value, however, a somewhat higher quality reproduction could be made from "photographs" if essential to the understanding of the dissertation. Silver prints of "photographs" may be ordered at additional charge by writing the Order Department, giving the catalog number, title, author and specific pages you wish reproduced.
5. PLEASE NOTE: Some pages may have indistinct print. Filmed as received.

Xerox University Microfilms
300 North Zeeb Road
Ann Arbor, Michigan 48106

Reproduced with permission of the copyright owner. Further reproduction prohibited without permission.

UNIVERSITY OF ALBERTA

EXPERIMENTAL STUDY OF MODELOCKED FIBER LASERS

By

Valerie Hughes ©

A thesis submitted to the Faculty of Graduate Study and Research in partial fulfillment of the requirements for the degree of **Master of Science**.

Department of Electrical and Computer Engineering

Edmonton, Alberta
Fall, 2005

Library and
Archives Canada

Published Heritage
Branch

395 Wellington Street
Ottawa ON K1A 0N4
Canada

Bibliothèque et
Archives Canada

Direction du
Patrimoine de l'édition

395, rue Wellington
Ottawa ON K1A 0N4
Canada

0-494-09192-4

Your file Votre référence
ISBN:
Our file Notre référence
ISBN:

NOTICE:
The author has granted a non-exclusive license allowing Library and Archives Canada to reproduce, publish, archive, preserve, conserve, communicate to the public by telecommunication or on the Internet, loan, distribute and sell theses worldwide, for commercial or non-commercial purposes, in microform, paper, electronic and/or any other formats.

The author retains copyright ownership and moral rights in this thesis. Neither the thesis nor substantial extracts from it may be printed or otherwise reproduced without the author's permission.

AVIS:
L'auteur a accordé une licence non exclusive permettant à la Bibliothèque et Archives Canada de reproduire, publier, archiver, sauvegarder, conserver, transmettre au public par télécommunication ou par l'Internet, prêter, distribuer et vendre des thèses partout dans le monde, à des fins commerciales ou autres, sur support microforme, papier, électronique et/ou autres formats.

L'auteur conserve la propriété du droit d'auteur et des droits moraux qui protège cette thèse. Ni la thèse ni des extraits substantiels de celle-ci ne doivent être imprimés ou autrement reproduits sans son autorisation.

In compliance with the Canadian Privacy Act some supporting forms may have been removed from this thesis.

While these forms may be included in the document page count, their removal does not represent any loss of content from the thesis.

Conformément à la loi canadienne sur la protection de la vie privée, quelques formulaires secondaires ont été enlevés de cette thèse.

Bien que ces formulaires aient inclus dans la pagination, il n'y aura aucun contenu manquant.

Canada

Reproduced with permission of the copyright owner. Further reproduction prohibited without permission.

To my mother, Dolly,
who provided an excellent home and environment
for scholarly growth;

To my husband, Aaron
who has been there to encourage me to achieve my best.

Abstract

This thesis discusses theoretical and experimental investigations of modelocked fiber ring lasers as well as the development of an interferometric autocorrelator. Various modes of pulsed operation are investigated for two types of passively modelocked fiber lasers. Further, the tunability of an actively modelocked fiber laser is investigated.

Generation of bound solitons, bunches of solitons and noise-like pulses were observed for both a stretched additive pulse modelocked (APM) erbium doped fiber (EDF) laser and a figure-8 nonlinear optical loop mirror (NOLM) EDF laser.

The stable operation of a high repetition rate, dispersion-tuned, harmonically modelocked EDF laser is also reported. Tunable multi and single wavelength operation was observed over the gain-bandwidth of the EDF.

An interferometric autocorrelator based on second harmonic generation (SHG) in a nonlinear crystal was successfully implemented. For pulses generated by the actively modelocked fiber laser, pulse width and chirp were characterized using this autocorrelator.

Based on the work described, significant insight was gained, and recommendations are made regarding future work in the area of modelocked fiber lasers.

Acknowledgement

I would like to take this opportunity to express my sincere gratitude to certain stellar individuals without whom this thesis could not have been completed.

Thanks to my supervisor Dr. Ray DeCorby, whose wisdom and guidance has proven to be a valuable resource during my stay at TRLabs. I would also like to thank him for taking a chance on me and accepting me as a graduate student.

Thanks to Dave Clegg for his vast knowledge and invaluable experience in the laboratory. His guidance in the lab has made me a stronger engineer.

Thanks to Ponnampalam Nakeeran, Tom Clement and Garth Hanson, for always being there to assist me whenever I needed an extra pair of hands or just someone to take over for me when I was tired.

Thanks to TRLabs and my supervisor, Dr. Ray DeCorby, for the much-appreciated financial assistant.

And finally, thanks to my family for their continuing support and to my husband for staying positive even when things seemed dire.

Table of Contents

List of Figures

List of Abbreviations

AM	Amplitude modulation
APD	Avalanche photodiode
APM	Additive pulse modelocking
BBO	Barium borate
CCM	Coupled cavity modelocking
CPM	Colliding pulse modelocking
CW	Continuous wave
DSF	Dispersion shifted fiber
EDF	Erbium doped fiber
EDFA	Erbium doped fiber amplifier
EDFL	Erbium doped fiber laser
Er	Erbium
FROG	Frequency resolved optical gating
fs	Femtoseconds (10^{-15} seconds)
FWHM	Full width at half maximum
GVD	Group velocity dispersion
He-Ne	Helium-Neon
Ho	Holmium
IR	Infrared
KLM	Kerr lens modelocking
LASER	Light amplification by stimulated emission of radiation
LHCP	Left hand circularly polarized
MFD	Mode field diameter

mm	Millimeter (10-^{3} meter)
NA	Numerical aperture
NALM	Nonlinear amplifying loop mirror
Nd	Neodymium
Nd-YAG	Neodymium – Yttrium Aluminum Garnet
nm	Nanometer
NOLM	Nonlinear optical loop mirror
NPE	Nonlinear polarization evolution
NPR	Nonlinear polarization rotation
ns	Nanoseconds (10^{-9} second)
PBS	Polarizing beam splitter
PC	Polarization controller
PM	Polarization maintaining
ps	Picoseconds (10^{-12} seconds)
RF	Radio Frequency
RHCP	Right hand circularly polarized
SAM	Self amplitude modulation
SHG	Second harmonic generation
Si	Silicon
SMF	Single mode fiber
SPM	Self-phase modulation
TDM	Time division multiplexing
TPA	Two photon absorption
μm	Micrometer (10^{-6} meter)

WDM	Wavelength division multiplexer
XPM	Cross-phase modulation
Yb	Ytterbium

List of Symbols

c	Speed of light in vacuum ($3\text{x}10^8$ m/s)
D_λ	Dispersion
δ	SPM coefficient
$\delta\omega$	Spectral broadening
Δ	Mode spacing
ϕ_{NL}	Nonlinear phase shift
γ	SAM coefficient
γ_{th}	Gain coefficient (minimum)
λ	Wavelength
n	Refractive index
τ	Pulse width
ω	Frequency

1 Introduction

"When the first lasers were operated, I and other scientists close to the research were surprised at how easy it turned out to be. We had assumed that, since lasers had never been made, it must be very difficult. But once you knew how, it was not at all difficult. Mostly what had been lacking were ideas and concepts."
- Arthur L Schawlow, 1981 Nobel Prize for Laser Spectroscopy (Bertolotti, 1983)

The development of the LASER (light amplification by stimulated emission of radiation) was the first important step in the establishment of the fiber optics industry. Lasers are the basic building blocks for the generation of short light pulses. Since the invention of the laser in the 1960s, the duration of the shortest pulse has shrunk by six orders of magnitude, going from the nanosecond (10^{-9} [s]) regime to the femtosecond (10^{-15} [s]) regime. Pulses in the femtosecond (fs) regime are referred to as ultrashort pulses and they have revolutionized many areas of research, some of which will be discussed later in this chapter. First, some of the highlights in the progression of short-pulse generation since the advent of the laser in the early 60s are discussed.

1.1 Historical overview

The first laser was realized by Maiman [1] in 1960 and was based on a ruby crystal pumped by a Xenon flash discharge. It created a laser pulse of fluctuating intensity lasting between a microsecond (10^{-6} [s]) and a millisecond (10^{-3} [s]). Later that year, Javan [2]made the first Helium-Neon (He-Ne) laser. This was the first laser to emit a steady beam, a so-called continuous wave (CW) laser.

Other researchers saw the potential in Maiman's work and decided to take steps in furthering this research. They began incorporating different substrates and rare earth ions such as Erbium (Er), Neodymium (Nd), Ytterbium (Yb), Holmium (Ho), Praseodymium (Pr) and even Uranium. This lead to the invention of the Neodymium - Yttrium Aluminum Garnet (Nd-YAG) laser in 1964[3].

In 1961 Hellwarth [4] proposed the concept of Q-switching, a process in which the laser is forced to emit pulses with duration on the order of several times the round trip propagation time of light in the laser cavity.

Next came the proposal of achieving shorter pulses by the concept of modelocking. By constructive interference, a short pulse is formed when many longitudinal modes are held in phase in a laser resonator. There are various techniques that have been employed, usually grouped under two categories: "active" or "passive" modelocking. Active modelocking uses a modulator inside the laser resonator, whereas passive schemes use a saturable absorber, often a thin semiconductor film, to lock the relative phase. Active modelocking of a He-Ne laser was first demonstrated by Hargrove *et al.* [5] in 1964. The pulse duration was well above 1 ns since the gain profile of the active Ne atom is narrow. Shortly after in 1965, Mocker and Collins [6] showed that the saturable dye used for Q-switching of ruby lasers could also be used to modelock these lasers. They demonstrated the first case of passive modelocking. Then in 1966, Demaria *et al.* [7] achieved pulses shorter than 1ns by modelocking an Nd-glass laser. The first pulses shorter than 1 ps were obtained by Shank and Ippen [8] in 1974. They demonstrated the first femtosecond (300 fs) pulses using a tunable broad gain dye laser media in combination with a saturable dye absorber.

The early 80s saw two important advances in the generation of stable femtosecond pulses. First came the novel modelocking technique known as colliding pulse modelocking (CPM), which was discovered by Fork *et al.* [9] in 1981. This enabled sub-100 fs pulses to be produced by a dye laser. The second advance occurred in 1984, when Fork *et al.* [10] showed that the group velocity dispersion (GVD) within the laser cavity could be continuously adjusted and optimized by introducing a prism sequence into the cavity. In 1985, Valdmanis *et al.* [11] reported pulse durations as short as 27 fs from a CPM dispersion compensated dye laser. In 1987, Fork *et al.* [12] reported a repetitive train of 6 fs pulses employing similar GVD compensation.

In the mid 80s, while the battle to achieve shorter pulses continued and new modelocking techniques were being developed, Mollenauer [13] came up with the soliton laser. The soliton laser consisted of two cavities; one cavity consisted of a synchronously pumped, modelocked colour center laser, which is coupled through a semitransparent mirror to the second cavity. The second cavity consisted of a length of single mode polarization maintaining fiber, and a beam splitter, microscope objective combination, which was used to couple the colour center laser into the polarization maintaining fiber, as shown in Fig.1.1. The operation of the laser was later explained by Haus *et al.* [14],[15], as an interference phenomenon between the pulses circulating in the two sub-resonators and their summation at the semitransparent mirrors (M_0). Through proper phase matching, a net pulse shaping is produced analogous to that of a saturable absorber. This process was called additive pulse modelocking (APM).

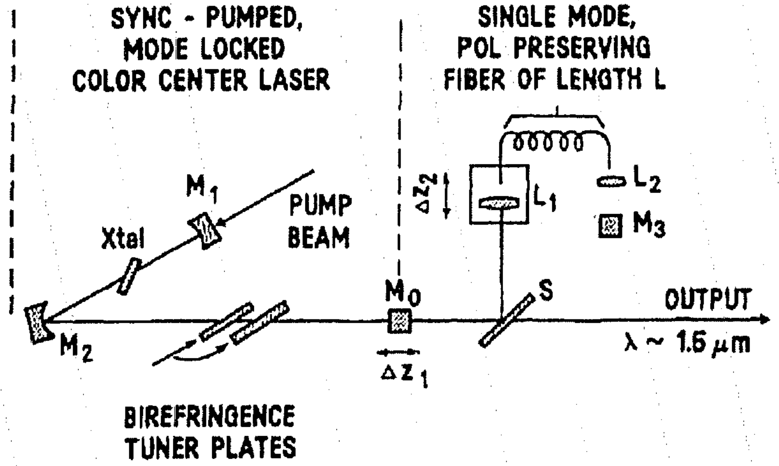

Fig. 1-1: Schematic of the soliton laser. Typical reflectivities: M_0 ~ 70%, S~50%, (M_1, M_2, M_3 ~ 100%). Birefringence plates: sapphire, 1 and 4 mm thick[13].

The 1980s also saw a renewed interest in solid-state laser media. This led to the development of the Titanium Sapphire (Ti-Sapphire) laser by Moulten [16] in 1982. The broad emission spectrum showed potential to support light pulses of only a few femtoseconds in duration. In 1991, Spence *et at.* [17] discovered that these lasers can be modelocked without the use of a saturable absorber. This modelocking technique was termed "self-modelocking" or "Kerr-lens modelocking" (KLM). This modelocking technique led to the demonstration of 6.5 fs pulses from a Ti-Sapphire laser by Jung *et al.* [18] in 1997.

The foundation for fiber lasers was laid in the 1960s, when researchers started experimenting by incorporating rare earth ions into glass hosts. Early work focused mainly on Neodymium doped silica fiber lasers. Doping of silica fibers with Erbium ions was not achieved until the 1980s. Since that time Erbium doped fiber lasers (EDFL) have received much attention because of the lasing wavelength of 1550 nm, which coincides with the low loss window of standard fiber. The first EDFL was reported by Mears *et al.* [19]. This was the first observation of CW lasing of a three level system at room temperature. They also demonstrated the first Q-switched operation of an EDFL using an intracavity acousto-optic modulator. They were able to produce 60 ns pulses.

Development in the field of EDFL has been continuously growing since the first demonstration in the mid 80s. The performance and the pulse characteristics of EDFLs have been significantly improved, by employing various cavity configurations [20] and modelocking techniques [21]. Pulse duration as short as 63 fs was achieved by Tamura et al. [22] using a "stretched pulse" APM EDFL. The stretched pulse technique is a process in which sections of negative and positive GVD fiber are used within the cavity to compensate for dispersion, similar to the technique proposed by Fork *et al.* for continually adjusting the GVD.

The achievable pulse width and energy from a fiber laser are not nearly equal to that of a Ti-Sapphire laser, however they do have many advantages that have motivated significant research over the past 20 years. Among the numerous advantages of fiber lasers are low losses and the possibility of pumping with compact, efficient diodes. The fiber itself provides the waveguide; hence the need for bulk optics is minimized. These lasers are also easily modelocked because of an enhancement of fiber nonlinearities due to high intensities and long interaction length. Fiber lasers are compact, robust and inexpensive sources of femtosecond pulses with numerous applications in the field of optics.

1.2 Applications of short pulsed lasers

Pulsed lasers have numerous applications in both research and industry and their uses are expected to broaden. These applications vary depending on wavelength, power and pulse width. Short pulse duration and high peak powers are the two main characteristics of ultrashort laser pulses that have been useful in the analysis of materials. They allow for time resolved experiments in which the transient response of materials can be observed on a [fs] scale [23][24]. Fabrication of passive integrated optical devices is another area in which pulse lasers are being employed. Femtosecond lasers have been shown to directly induce large refractive index changes in glasses and other dielectric materials [25]. Hence they have been used for fabrication of optical devices, such as Bragg gratings [26][27] and optical waveguides [28].

With the imminent arrival of practical, compact and cost effective femtosecond laser sources, real world application of ultrashort laser pulses in communications systems has become very likely. Short pulse lasers are ideal for use as sources in all optical switching based on the third order nonlinear Kerr effect, as they provide the large intensities that are required. Since the Kerr effect is an intensity dependent process, the device transmission is intensity dependent. The optical beam itself induces the switching depending on its intensity [29]-[32]. The large spectral bandwidth offered by short pulse lasers also makes them ideal for wavelength division multiplexed (WDM) and time division multiplexed (TDM) networks [33].

1.3 Project objective

There is great incentive to develop a new generation of femtosecond lasers that are compact, robust and easy to operate. High power fiber laser technology is considered to be a prime candidate for the transformation of ultrafast lasers from a scientific tool into an industrial tool.

Laser systems employing doped fibers provide certain advantages over conventional solid-state lasers. Fibers are flexible and can be rolled up into a tight spool making it possible to construct a very compact package. Additionally, the laser light is confined to the core of the fiber, providing a well-controlled beam shape. These lasers are also well suited to ultrafast applications, as they have a large amplification bandwidth and can be mode-locked to generate ultrashort pulses.

The objective of the current project was to realize and study modelocked fiber ring lasers. To this end the theory and experimental results of modelocked fiber ring lasers, given in literature, were tested. As well, the different modes of operation of fiber ring lasers were investigated. Additionally, an experimental facility for charactering femtosecond pulses was established.

This thesis outlines the design, implementation, and characterization of two-stretched APM erbium doped fiber lasers, an actively modelocked fiber ring laser and an interferometric autocorrelator for the characterization of femtosecond pulses.

1.4 Thesis layout

Although several interesting concepts were investigated and many experiments carried out in the lab, only the issues directly related to the objective of the project will be discussed, therefore limiting the writing to six brief chapters.

Chapter two and three provides a brief discussion of the laser theory that is relevant to the experimental part of the thesis. Chapter four and five discusses the experiments carried out towards the objective and the results from the experiments, respectively. Chapter six presents some concluding remarks and suggestions for some future work on this project, followed by a list of references and appendices with project related support information.

2 Theoretical aspects of short pulse lasers

2.1 Basic laser theory

There are a number of interesting principles that come into play in the operation of the modelocked Erbium doped fiber laser. This chapter briefly introduces the main principles relevant to understanding the operation of such a laser.

The generation of light in an Erbium doped fiber (EDF) can be described using a three level lasing model, since the Er^{3+} ions exist primarily in one of three energy levels (Fig. 2-1). The energy levels are labeled with respect to the ground level E_1. E_2 is the metastable state, where the term metastable implies that the lifetimes for transitions from this state to the ground state are very long compared with the lifetimes of the higher energy states. E_3 is the pump level; the pump band is fairly narrow, and so the pump wavelength must be exact to within a few nanometers.

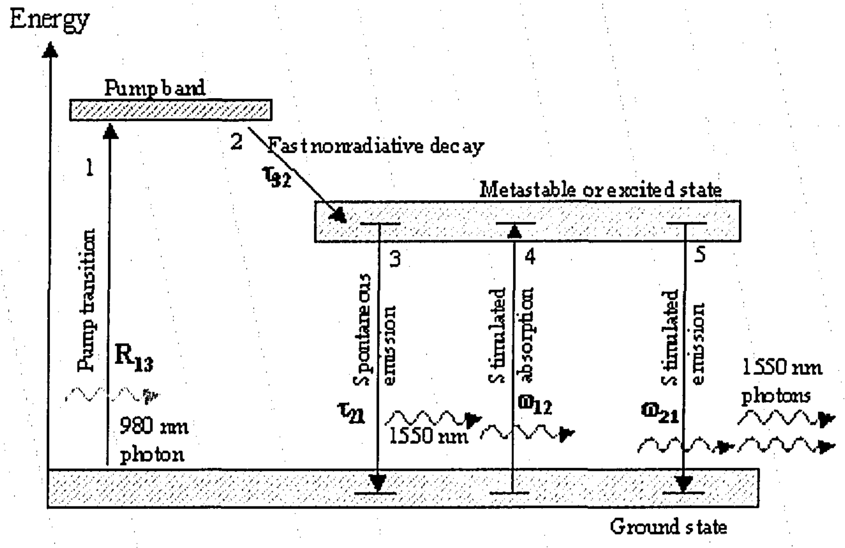

Fig. 2-1: Simplified energy-level diagram of various transition processes of Er^{3+} ions in silica glass [34]

Typically, a pump laser emitting 980-nm photons is used to excite ions from the ground state to the pump level (process 1). These excited ions decay (relax) very quickly (typical delay time is 1us for Er in Silicate glasses) from the pump band to the metastable band (process 2). During this decay, the excess energy is released as phonons (or equivalently thermal energy) in the fiber. Within the metastable band, the electrons of the excited ions tend to populate the lower end of the band due to thermodynamic considerations. Some of the ions sitting at the metastable level can decay back to the ground state in the absence of an external influence (process 3). This process is known as spontaneous emission and adds noise to the system.

When a signal photon with energy corresponding to the band-gap energy between the ground state and the metastable state passes through the system, two other types of transitions take place. First, it is possible for photons to be absorbed by ions in the ground state, which raises these ions to the metastable level (process 4). This is known as stimulated absorption. Second, a photon can trigger an excited ion to drop to the ground state, thereby emitting a new photon of the same energy, wavelength and polarization as the incoming signal photon (process 5). This process is known as stimulated emission and it is the mechanism providing amplification in an EDFL. The widths of the metastable and ground state levels allow high levels of stimulated emission to occur in the 1530-to-1560 nm range.

2.2 Basic laser resonator configuration

Amplification of light in a section of pumped EDF is achieved by feeding the output back into the input of the EDFA to form an optical resonant cavity. Allowing some of the light within the resonator to escape as usable light results in a potential source of EDF laser light.

There are two basic resonator designs for fiber lasers, the traveling wave ring resonator [35] and the standing wave Fabry-Parot resonator [35]. This section will focus on the traveling wave ring resonator depicted in Fig. 2-2.

It should be noted that there is no external input signal (at the lasing wavelength) applied to the cavity, although external pump light is injected. The lasing signal is essentially initiated by a small amount of spontaneous emission created upon initial pumping. If the gain and phase conditions are met, lasing within the cavity will occur, producing continuous light.

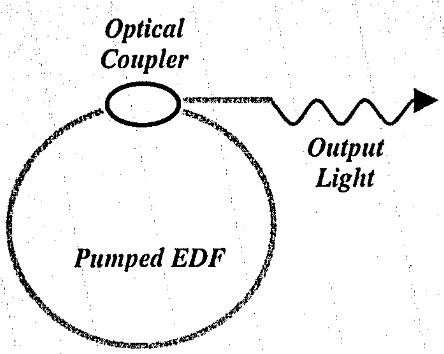

Fig. 2-2: Traveling wave ring resonator.

2.2.1 *Gain conditions for laser operation*

For a traveling wave ring resonator, the round trip gain must be equal to or greater than the round trip losses. The minimum gain coefficient value γ_{th} required for lasing is given by [35]:

$$\gamma_{th} = L - \frac{\ln R}{l} \qquad (2.1)$$

where: R = effective fractional power reflectivity of the coupler or ($R = 1\text{-}C$), C = output power coupling ratio, L = the total lumped fractional intensity loss per round trip, l = the total round trip distance (one round-trip equals the total ring circumference)

2.2.2 *Phase condition for lasing*

The phase requirement for laser operation is that an integer number of resonating wavelengths must fit within one round trip of the laser's resonant cavity. For an EDF ring laser, since the length of the cavity is very long relative to the resonant wavelength, there are many wavelengths, referred to as longitudinal modes, which satisfy the phase condition.

For a multi-longitudinal mode operating ring resonator, the expected frequency spacing *df* between modes is given by:

$$df = \frac{c}{nl} \qquad (2.2)$$

where c is the speed of light in vacuum, n is the optical refractive index and l is the cavity length (ring circumference).

The typical amplification range (gain bandwidth) for EDF spans over 30nm, from 1530 nm to 1560 nm as depicted in Fig. 2-3, implying that many longitudinal operating modes can possibly satisfy the gain and phase conditions for lasing. Hence EDF lasers have the potential to be highly multi-mode lasers. The light generated within each mode is coherent (intra-modally coherent) but it is incoherent between different modes (inter-modally incoherent). Each of these modes oscillate independently, with no fixed relationship, in essence like a set of independent lasers all emitting light at slightly different frequencies. The individual phase of the light waves in each mode is not fixed and may vary randomly.

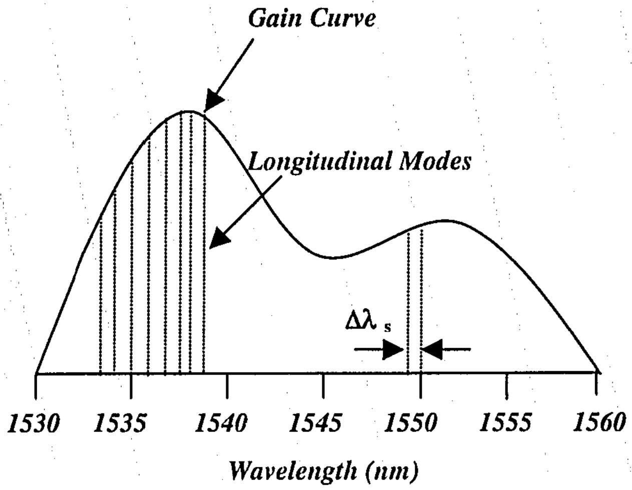

Fig. 2-3: Gain curve depicting the many longitudinal modes that could satisfy the gain and phase requirements for lasing. $\Delta\lambda_s$ is the wavelength spacing between modes.

For a continuous wave laser, this multi-modal behavior is undesirable and various measures [36] can be taken to ensure that the laser operates at only one of the many possible longitudinal modes. Modelocked lasers take advantage of the large gain bandwidth and this multi-modal behavior to produce ultrashort, high-energy pulses. If instead of oscillating independently, each mode operates with a fixed phase between it and the other modes, the modes will constructively interfere with one another, producing intense bursts or pulses of light. Such a laser is said to be modelocked. The main techniques used for modelocking fiber lasers will be discussed in Chapter 3. First, a few other important concepts that are important for a complete appreciation of modelocking are discussed.

2.3 Dispersion

A dispersive medium is characterized by a frequency-dependent refractive index, absorption coefficient, and phase velocity, so that plane waves of different frequencies travel in the medium at different velocities and experience different attenuation. Since a pulse of light is essentially a sum of monochromatic waves of varying frequencies (through Fourier theory), each frequency component is modified differently as it propagates in a dispersive medium.

If a pulse is characterized by a spectral width $\Delta\lambda_0$, then each wavelength component will propagate with a unique group velocity, resulting in temporal broadening of the pulse. This is called group velocity dispersion (GVD). For a Gaussian envelope pulse, the amount of temporal broadening is given by [37]

$$\tau(z) = \tau_0 \left[1 + \left(\frac{z}{z_0} \right)^2 \right]^{\frac{1}{2}} \tag{2.3}$$

$$Z_0 = \frac{c\pi\tau_0^2}{\lambda_0^2 D_\lambda} \tag{2.4}$$

where z is the propagation distance, λ_0 is the center wavelength, τ_0 is the pulse width, and D_λ is the material dispersion (GVD). If $D_\lambda > 0$, the GVD is said to be anomalous and if $D_\lambda < 0$ the GVD is said to be normal.

If the instantaneous frequency within the pulse envelope changes with time as a result of GVD, such a pulse is said to be a chirped pulse. If an unchirped pulse passes through a medium of normal GVD, the instantaneous frequency becomes higher towards the trailing edge of the pulse. Thus the leading edge of the pulse has a frequency lower than the center frequency (downshifted) and the trailing edge has a frequency higher than the center frequency (upshifted). In other words, the higher frequencies arrive later than the lower frequencies. Similarly if an unchirped pulse passes through a medium with anomalous dispersion, the leading edge of the pulse will be upshifted and the trailing edge downshifted. So the overall effect is a broadened chirped pulse (Fig. 2-4).

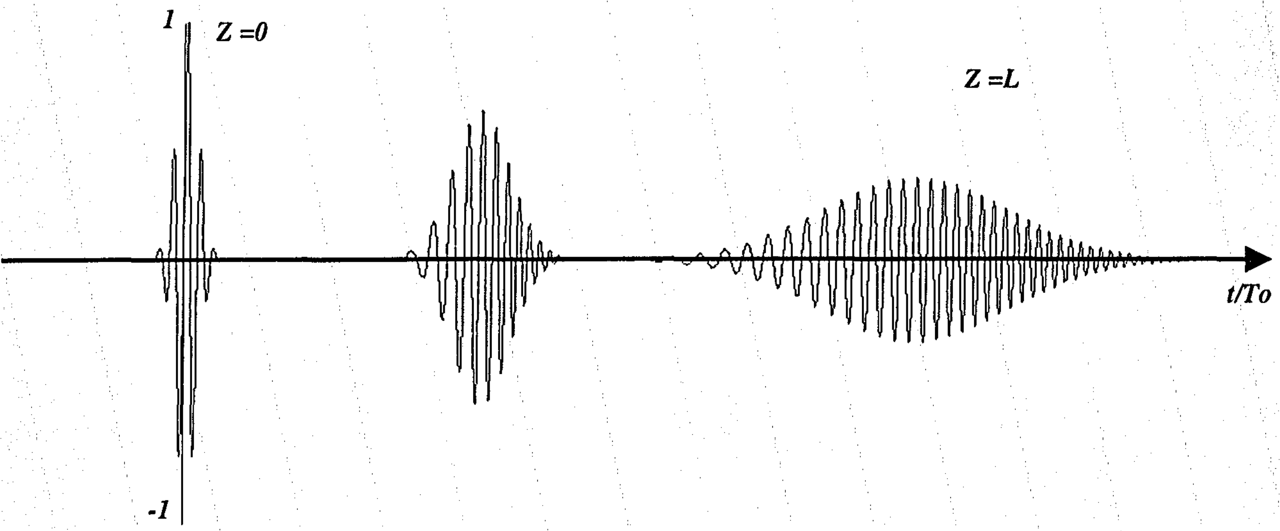

Fig. 2-4: Calculated temporal variation of the electric field of an optical pulse as it propagates along a length of fiber with anomalous dispersion. Note that as the pulse broadens in the time domain it also gets chirped. (see Appendix B for details on calculations)

A chirped pulse can be compressed by propagating it through another linear dispersive medium but with dispersion opposite to the first medium. However, using dispersion alone, a Gaussian pulse can only be compressed to a minimum pulse width given by [37]

$$\Delta\tau_{\min} = \frac{4\ln 2}{\Delta\omega_f} \tag{2.5}$$

$$\Delta\omega_f = \frac{2}{\tau_0}\sqrt{2\ln 2} \tag{2.6}$$

For a given spectral bandwidth ($\Delta\omega_f$), the minimum pulse width can be calculated using the time-bandwidth product (TBP). For a Gaussian pulse the minimum TBP is 0.441 and for a hyperbolic secant pulse (sech) the TBP is 0.315 [64]. Pulses with a time-bandwidth product close to the minimum value are said to be "transform-limited". Refer to Appendix A.2 for further details.

To compress a pulse to $\Delta\tau_{min}$, the following conditions must hold:

$$\alpha' L' = -\alpha L \tag{2.7}$$

Here, α' and L' are the dispersion and length of fiber used to compress the pulse, respectively, and α and L are the dispersion and length of fiber that lead to the broadened pulse.

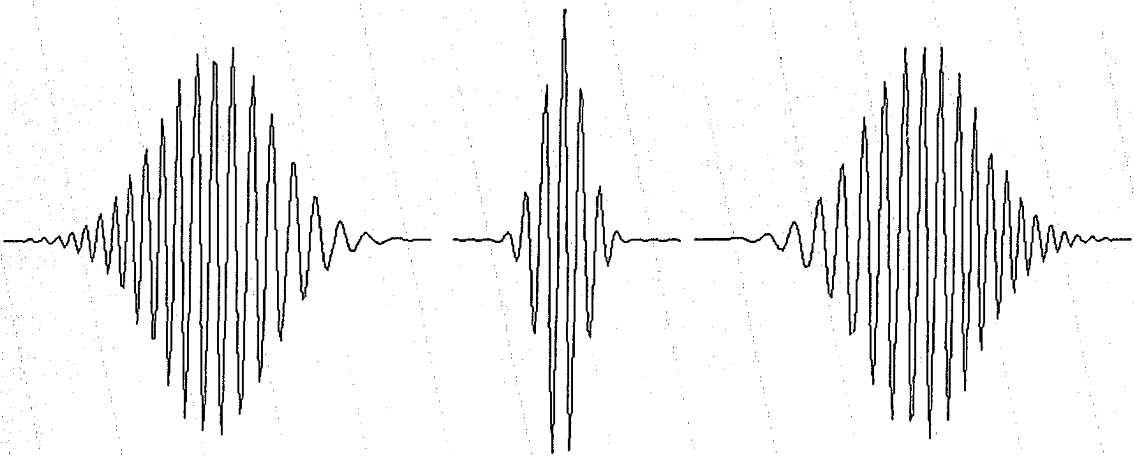

Fig. 2-5: Compression of a chirped pulse as it propagates through a linear dispersive medium. After compression to a minimum width, the pulse again undergoes broadening. (See Appendix B for calculation details.)

If the compressing fiber is longer than specified by (2.7) then the pulse will start to broaden again (Fig. 2-5). As mentioned earlier, a pulse cannot be compressed below the minimum pulse width given by (2.5) using linear optical effects (such as dispersion). However, further compression can be accomplished by first broadening the spectral content of the pulse (without any temporal broadening) and using dispersion of the proper sign. The effect of broadening the spectrum without broadening the temporal width is a nonlinear process called self phase modulation (SPM), which will be discussed in the next section.

2.4 Nonlinear Optics

The response of any medium is nonlinear for sufficiently intense electromagnetic fields. The induced polarization (***P***) (associated with the electric dipoles) is no longer linear in the electric field but becomes [38]:

$$P = \varepsilon_0 \left(\chi^{(1)} E + \chi^{(2)} E^2 + \chi^{(3)} E^3 \right) \tag{2.8}$$

where ε_0 is the vacuum permittivity, E is the electric field, and $\chi^{(j)}$ (j= 1, 2 ...) is the jth order susceptibility. The first term ($\chi^{(1)}$ E) in (2.6) represents the linear response and is the dominant contribution to ***P***. Its effects are included through the refractive index and the attenuation coefficient [39]. The second term ($\chi^{(2)}E^2$) represents the second order response and is responsible for nonlinear effects such as second harmonic generation and sum-frequency generation [39]. The third term ($\chi^{(3)}E^3$) represents the third order nonlinear response and is responsible for phenomena such as third harmonic generation, four-wave mixing, and nonlinear refraction [39]. Most of the nonlinear effects in optical fibers originate from nonlinear refraction, a phenomenon that refers to the intensity dependence of the refractive index. This effect is known as the optical Kerr effect.

2.4.1 Intensity dependent refractive index (optical Kerr effect)

The intensity dependent refractive index derives from the third order susceptibility and is given by (2.7)

$$n(I) = n_0 + n_2 I \tag{2.9}$$

where n is the linear refractive index, $I \sim |E|^2$ is the optical intensity and n_2 is the nonlinear index coefficient (the optical Kerr coefficient).

Many phenomena arise from the linear variation of refractive index with intensity; of particular interest to the work described here is self-phase modulation (SPM).

2.4.2 Self phase modulation (SPM)

The intensity dependent refractive index has a direct effect on the spectrum of any optical pulse, because the pulse has a time varying intensity. The propagation of a pulse described by the slowly varying amplitude approximation is given by [41]

$$E(L,t) = \frac{1}{2}\left[A(L,t)e^{j(\omega_0 t - KL)}\right] \tag{2.10}$$

where *A(L,t)* is the slowly varying envelope and L is the length of the Kerr medium. Further $KL = \frac{2\pi(n_0 + n_2 I(t))}{\lambda_0}L = \frac{2\pi n_0 L}{\lambda_0} + \frac{2\pi n_2 I(t) L}{\lambda_0}$; the second term represents the nonlinear phase shift caused by SPM.

SPM is a phenomenon that leads to spectral broadening of optical pulses as a result of the time dependent nonlinear phase shift. A temporally varying phase implies that the instantaneous optical frequency differs across the pulse. The time dependence of the different frequencies can be viewed as a frequency chirp. The chirp is induced by SPM and increases in magnitude with propagation distance [41]. In other words, new frequency components are continuously being generated as the pulse propagates down the fiber. These generated frequency components broaden the spectrum over its initial width. The maximum nonlinear phase shift experienced by a pulse is given by [41]

$$\phi_{NL}^{\max} = \frac{2\pi n_2 I_0 L}{\lambda_0} \tag{2.11}$$

where L is the propagation distance, λ_0 is the center wavelength, and I_0 is the peak intensity of the pulse. The maximum amount of spectral broadening for a pulse of duration τ_0 is given by [41]

$$\delta\omega_{\max} \cong \frac{\phi_{NL}^{\max}}{\tau_0} \tag{2.12}$$

Phase modulation can be converted into intensity modulation, for example by using the difference between the self modulated phases of two polarization components as a wave retarder placed between crossed polarizers. This is similar to what is done in additive pulse modelocking of fiber lasers, which will be discussed in Chapter 3.

SPM is often accompanied by cross phase modulation (XPM), a phenomenon that leads to coupling between two or more incident waves or modes through the fiber nonlinearity. This occurs because the effective refractive index of a wave depends not only on the intensity of that wave but also on the intensity of other copropagating waves [38].

2.5 Birefringence

A single mode fiber is not truly single mode; even a perfectly cylindrical single mode fiber supports two degenerate polarization modes. Small departures from a perfect cylindrical geometry or small fluctuations in the material anisotropy results in these modes becoming slightly non-degenerate. Therefore, in practice a fiber supports two slightly non-degenerate modes that are dominantly polarized in two orthogonal directions. Mathematically, the mode-propagation constant becomes slightly different for modes polarized in the x and y directions. This is referred to as modal birefringence. The degree of modal birefringence B is defined by [38]

$$B = K_0 \mid n_x - n_y \mid \tag{2.13}$$

where $K_0 = 2\pi/\lambda$, n_x and n_y are the effective mode indices in the two orthogonal polarization states. The axis along which the effective mode index is smaller is called the fast axis, as the group velocity is larger for light propagating in that direction. Similarly, the axis with the larger mode index is called the slow axis.

The relative strength of the birefringence is described by the beat length, i.e. the length of period in which the polarization state is reproduced. The beat length is given by (2.14) and for standard SMF28 fiber this length is approximately 2 – 10 m at 1550 nm [40].

$$L_B = \frac{2\pi}{B} \tag{2.14}$$

Elliptically polarized light can be resolved into its right and left hand circular polarization components of different intensities. If the light input to a fiber is elliptically polarized, cross phase modulation (XPM) [38] induces nonlinear coupling between the x and y electric field components creating nonlinear birefringence, which changes the state of polarization. This phenomenon is referred to as nonlinear ellipse rotation since it is manifested as a rotation of the polarization ellipse.

2.6 Kerr ellipse rotation or nonlinear polarization rotation

Since the refractive index depends on the intensity of light, elliptically polarized light sees an induced birefringence - the index is slightly higher for polarization along the major axis of the ellipse. This holds back the phase of that component of the E-field, and alters the ellipse slightly. The effect is to tilt the major axis of the ellipse slightly as shown in Fig. 2-6. The effect is continuous, since there is now a new birefringence along the new major axis. The net effect is that high intensity elliptically polarized light in a Kerr medium experiences a continuous rotation of the major axis of the ellipse. This is called Kerr ellipse rotation or nonlinear polarization rotation.

Another way to look at this is in terms of the right and left hand circularly polarized light (RHCP and LHCP respectively). Consider an elliptically polarized light made up of a strong right-handed circular light and somewhat weaker left-hand circular light. The right circular light will see a slightly larger index of refraction than the left, thus the right circular component will steadily drop back in phase, relative to the left-circular component. The result is a slow precess of the polarization ellipse as the light propagates [41].

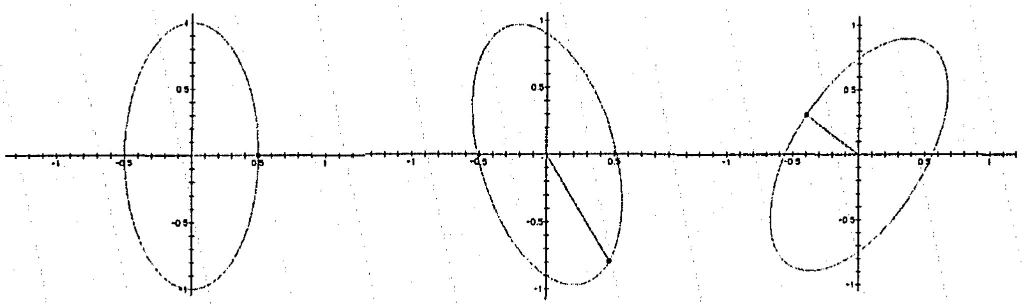

Fig. 2-6: Nonlinear polarization rotation of an ellipse as it propagates through a Kerr medium.

3 Modelocked fiber ring lasers

Modelocking is a powerful technique for obtaining femtosecond pulses. It is a process in which the longitudinal modes of a laser are forced into phase synchronism. The different modes add constructively in such a way that the laser produces a train of pulses. This is illustrated in Fig. 3-1.

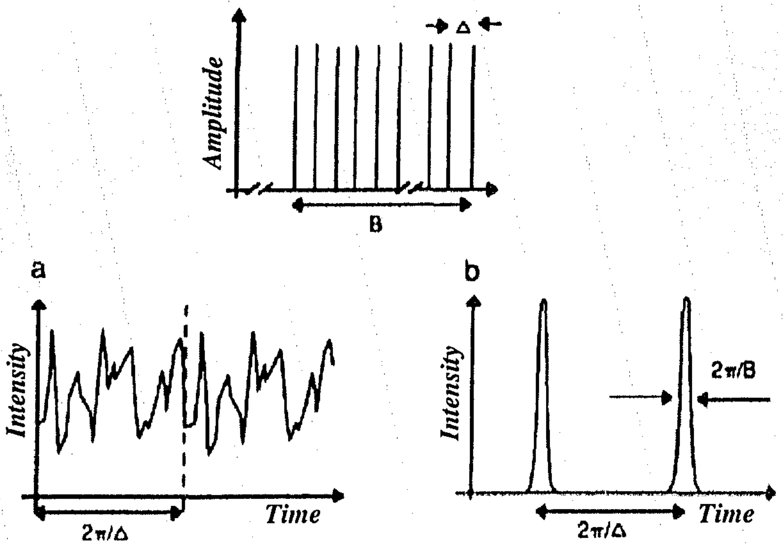

Fig. 3-1: A set of equally spaced modes, and the inverse Fourier transform of that spectrum. In (a) the modes have a random phase distribution. In (b), all the modes are "locked" to have a constant phase relationship. Δ = mode spacing, B = bandwidth, 2π/Δ = round trip time or repetition rate of the laser, and 2π/B = width of the burst of light [39].

The mode spacing (Δ) of the longitudinal modes is calculated by:

$$\Delta = \frac{c}{L_{opt}} \tag{3.1}$$

where $L_{opt} = nL$ for a ring cavity, L is the length of the cavity and n is the effective mode index of the medium. The number of modes (N) supported by a cavity is dependent on the gain bandwidth (B) and can be approximated by

$$N = B / \Delta \tag{3.2}$$

In order to obtain short pulses, a large number of longitudinal modes have to be available. Therefore a gain medium with a large bandwidth is necessary. Erbium doped fiber lasers have a gain linewidth of approximately 4 THz and are capable of supporting over 100,000 modes for a cavity approximately 10 m long. By comparison He-Ne lasers have a gain linewidth of approximately 1.7 GHz, reducing the number of longitudinal modes available by three orders of magnitude relative to the EDF lasers.

Modelocking is generally separated into two categories, called "active" and "passive" modelocking. In active modelocking, coupling between the cavity modes is achieved by using an amplitude or phase modulator to lock their phases. This requires modulation of either the amplitude or the phase of the optical field at a frequency that is an integer multiple of the mode spacing. In bulk laser cavities this is often accomplished by the use of an acousto-optic modulator. A Lithium Niobate electro-optic modulator is typically used in fiber lasers. In passive modelocking, an intensity dependent loss or dispersion mechanism (usually a saturable absorber) is used to lock the relative phase. The theory of the passive modelocking techniques used in fiber lasers will be the focus of this chapter. A brief discussion on active modelocking will also be given. For a detailed explanation of the theory of active modelocking, refer to [21],[42].

3.1 Passive modelocking of fiber ring lasers

Passive modelocking in fiber lasers generally employs either a semiconductor saturable absorber or some form of all-fiber modelocking. In the latter case, the nonlinear properties of the fiber act as an artificial saturable absorber. Examples include additive pulse modelocking (APM) by nonlinear polarization rotation/evolution [59] or use of a nonlinear optical loop mirror (NOLM) or nonlinear amplifying loop mirror (NALM) [82].

3.1.1 Passive modelocking with saturable absorber

Passive modelocking can be achieved by using a fast saturable absorber [21],[43], an absorber for which the relaxation time is short compared to the modelocked pulse duration, or by using a slow saturable absorber [21],[44], an absorber for which the relaxation time is long compared to the modelocked pulse duration. Fig. 3-2 will be used to illustrate some of these concepts.

A saturable absorber is used to obtain a self amplitude modulation of the light inside the cavity. The absorber introduces loss that is large for low intensities but significantly smaller for high intensities. Thus, a short intense pulse produces a loss modulation because the high intensity at the peak of the pulse saturates the absorber more strongly than the low intensity wings. This results in a reduction of the loss for short pulses, and a recovery that depends on the type of absorber used (slow or fast). In effect, the circulating pulse saturates the laser gain to a level that is sufficient to compensate for losses, however any other circulating low-intensity light experiences more loss than gain and thus dies out during the following round trip.

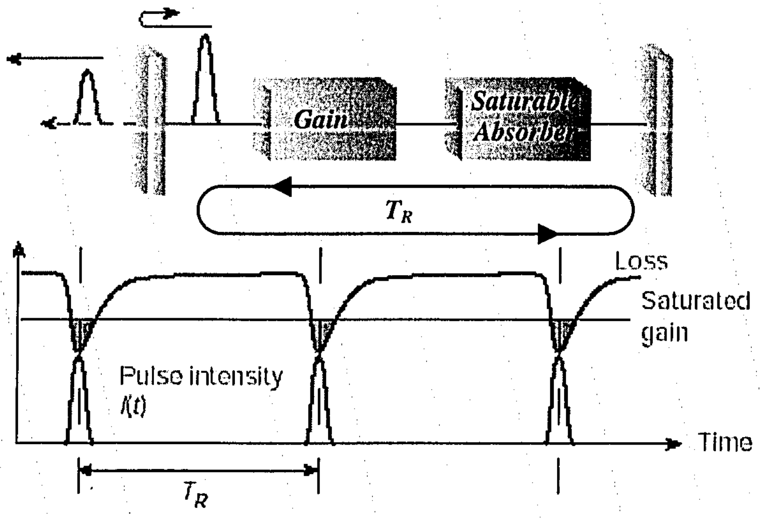

Fig. 3-2: Simplified schematic of a laser passively modelocked by a fast saturable absorber and time dependent loss and net gain. T_R = round trip time [60].

Generally, very short pulses can be obtained with passive modelocking using a fast saturable absorber. This is because the fast recovery time of the absorber results in a fast loss modulation, which in turn results in shorter and shorter pulses each round trip until some limit is met. One of the factors that sets this limit is the gain bandwidth; the spectral range of the gain limits the range of frequencies any pulse may have and so places a lower limit on the pulse duration (Fourier Theory).

Various semiconductor saturable absorber structures have been incorporated into fiber lasers to obtain modelocking with simple cavity designs. For example an InGaAs/GaAs-on-GaAs superlattice was used as a fast saturable absorber in an Erbium doped fiber ring laser [45]. Modelocking with polarization-maintaining (PM) EDF and a bulk InGaAsP saturable absorber was demonstrated to produce near transform limited femtosecond pulses [46].

3.1.2 Passive modelocking using APM by nonlinear polarization rotation

Additive pulse modelocking (APM) or coupled cavity modelocking (CCM) achieves fast saturable absorber action by exploiting the Kerr effect in an interferometric configuration. The principle of APM is pulse shortening by coherent addition of two versions of the same pulse, one of which has passed through a Kerr medium. This is illustrated using Fig. 3-3. The fiber in the feedback cavity acts as the Kerr medium and the coherent addition takes place at the output beamsplitter. The pulses returning from the feedback cavity into the main cavity constructively/destructively interfere with those pulses that are already in the main cavity. By properly adjusting the cavity parameters, it is possible to create a situation such that there is constructive interference near the peak of the pulses but destructive interference in the wings. This is possible because the peak and wings of the pulse acquire a different nonlinear phase shift in the fiber. Thus the peak of the circulating pulse can be enhanced while the wings are attenuated, which essentially shortens the pulse. The earliest realization of this was accomplished with two coupled resonators [13],[48], hence the name couple cavity modelocking.

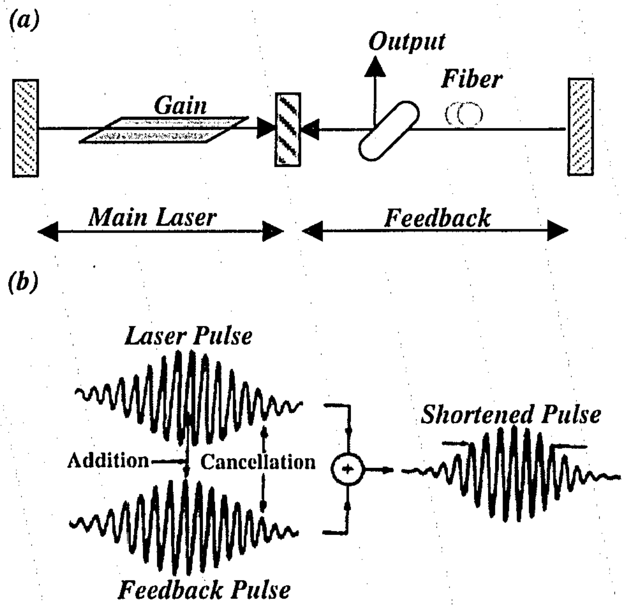

Fig. 3-3: A typical APM coupled cavity laser (a). At the output beamsplitter, the pulse of the main cavity [(b) top left] adds to the pulse of the auxiliary cavity [(b) bottom left], to result in a shortened pulse [(b) right]. [64]

This principle was later extended to fiber lasers in a single cavity interferometric configuration (Fig. 3-4). The cavity is a ring resonator with a Faraday isolator to force unidirectional operation. In addition to the isolator/polarizer, the ring is composed simply of an erbium doped fiber section and two polarization controllers that form the nonlinear Mach-Zehnder interferometer. These cavities use nonlinear polarization rotation (Fig. 3-5) to achieve additive pulse modelocking action. The polarization controller (PC1), (shown as the wave plate in Fig. 3-5) and the polarizer produce the APM action by first transforming linear polarization into elliptic polarization. Self phase modulation (SPM) and cross phase modulation (XPM) in the fiber (Kerr medium) rotates the ellipse. The state of the polarization is nonuniform across the pulse because the Kerr effect is intensity dependent. The intense peak (Fig. 3-5a) will be rotated more than the weak wings (Fig. 3-5b). The polarizer (analyzer) transforms the rotation of the ellipse into amplitude modulation; it lets the central intense part of the pulse pass through, but absorbs the lower intensity wings. In this way intensity dependent transmission is achieved, providing the saturable absorber action. This modelocking technique is referred to as polarization APM since the right and left circular polarization states acquire a differential phase shift and are added together at the polarizer. In an ideal system (perfectly isotropic fiber), in which the polarization axis would be maintained in linear operation, only one polarization controller (PC1) would be needed. The second polarization controller (PC2) receives the Kerr-rotated state, and converts it back to the desired polarization for the polarizer in the isolator.

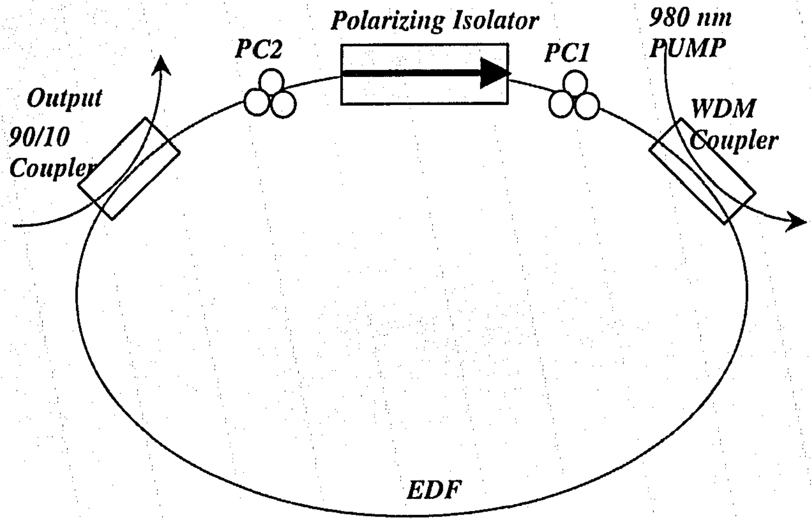

Fig. 3-4: Schematic of an all-fiber ring laser modelocked by P-APM. PC: polarization controllers, WDM: wavelength-division multiplexed coupler.

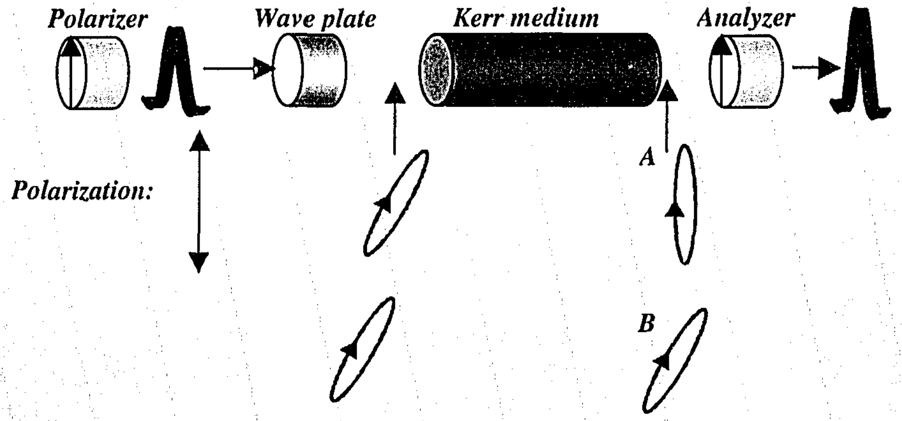

Fig. 3-5: The APM action through polarization rotation. A) high intensity, B) low intensity.

If constructed from typical fibers exhibiting normal GVD, the laser discussed above (Fig. 3-4) is known as a fiber soliton laser and there are inherent practical limits on the minimum pulse width of these lasers due to resonant instabilities [66]. Resonant instabilities exist when the period (the laser length) approaches $8Z_0$, where Z_0 is the soliton period. The soliton period is the distance over which the soliton accumulates a phase shift of 2π. This instability arises from the periodic perturbation of the pulse energy over the cavity length, due to gain and loss (including output coupling). This perturbation manifests itself in the formation of discrete sideband generation in the spectrum of these lasers [53]. This eventually limits the pulse width, which limits the pulse energy based on the soliton area theorem. The theorem states that the product of the peak amplitude (A_0) and pulse width (τ) is fixed by the average dispersion and nonlinearity. The soliton area is given by [53] equation (3.3), where D is the contribution from GVD and δ is the SPM contribution from the Kerr effect. The energy of a soliton given by equation (3.4) is thus limited when either the peak power $|A_0|^2$ or the pulse width (τ) is limited.

$$A_0\tau = \sqrt{\frac{2|D|}{\delta}} \tag{3.3}$$

$$W = 2|A_0|^2\,\tau \tag{3.4}$$

Because of the interferometric nature of the APM action, the transmission of a pulse passing through an APM structure will have a sinusoidal dependence on the nonlinear phase shift [67]. This dependence places a limit on the transmission, implying the possibility of "saturating" the APM action [67]. The APM action or self amplitude modulation (SAM) can be accurately represented by (3.5), where γ represents the SAM coefficient and it is proportional to the gain and Kerr coefficient [67], and a represents the pulse which is equal to $a = A_0 \sec h\left(\frac{t}{\tau}\right)$, in the case of a soliton laser. A_0 is the peak amplitude and τ is the pulse width.

$$\sin(\gamma|a|^2) \tag{3.5}$$

The "energy gain" of a pulse passing through an interferometer [67] is given by (3.6). Finding the maximum of (3.6) gives the upper limit of the energy gain, which places an upper limit on the peak power.

$$\int_{-\infty}^{\infty} dt\,|a|^2 \sin(\gamma|a|^2) \tag{3.6}$$

The maximum of (3.6) is found when $\gamma | A_0 |^2 \sim 0.6\pi$ [67]. This limit on the peak power $|A_0|^2$ implies a limited pulse energy based on the soliton area theorem. Hence if the pump power is increased to obtain higher peak powers, the peak power of the soliton will eventually reach the limit imposed by (3.6), "saturating" the APM action. Since the number of circulating pulses is defined by the ratio of the stored intracavity energy to the soliton energy [68], saturation of the APM leads to a quantization of the pulse energy. That is, the single pulse per round trip breaks up into multiple, uncontrolled pulses. Thus in these lasers, low energy, multiple pulses of relatively long durations (>300 fs) are most often observed [69]. There are two possibilities of achieving shorter pulses in a single-pulse operating regime. The first approach is using shorter cavities or cavities with low anomalous GVD with the gain adjusted to be low enough so that the energy of one single quantized soliton fully depletes the gain [53]. The second approach is a reduction in the nonlinearity. There are limitations to shorter cavities, one of which is imposed by the minimum length of fiber necessary for adequate gain. Reduction in the nonlinearity and controlled GVD scheme is a preferred solution. For femtosecond fiber lasers, the "stretched" pulse laser has been the most successful approach to nonlinearity reduction (Fig. 3-6).

The operation of this laser is very similar to the soliton laser described earlier. Consider a pulse starting at the first polarization controller, it travels along the optical fiber (mostly SMF-28) and suffers anomalous dispersion. This causes the pulse to become broadened and chirped, so that the highest frequencies arrive first with lower frequencies following. As the pulse stretches in time, the intensity drops. Once the pulse leaves the anomalous dispersion fiber, it enters the EDF amplifier segment, which has normal dispersion. As the pulse travels through this segment, it is amplified and the opposite dispersion causes it to compress and the intensity goes up concomitantly. Around the middle of the fiber, the pulse is at its shortest and highest intensity. After this point, the continuing normal dispersion makes the pulse progressively more stretched and chirped. Entering the anomalous dispersion fiber segment once again, the dispersion is reversed, and the pulse compresses once more until it is returned to its original position. If the lengths of the two fiber segments are approximately matched, the pulse will return with it original duration.

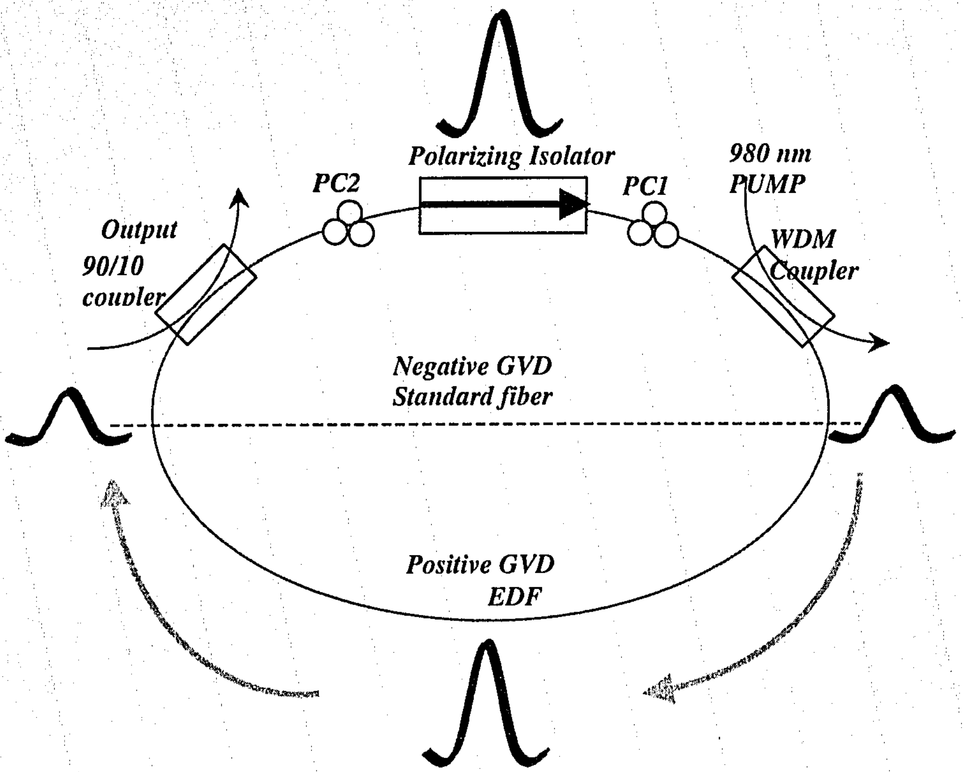

Fig. 3-6: Schematic of a stretched pulse APM erbium doped fiber ring laser, sections of large positive and negative dispersion fiber causes the pulse to be alternately stretched and recompressed as it propagates around the cavity.

If the nonlinear phenomenon of ellipse rotation is added and APM action is achieved. Where the pulse is at its shortest duration in the cavity and hence its highest intensity, there is a concentration of the polarization rotation effect. In this way the net average peak power in the laser is lowered and as a result the net nonlinear phase shift per pass is lower; hence APM saturation is delayed and higher pulse energies are possible.

3.1.3 Passive modelocking using APM by NOLM / NALM

A fiber Sagnac interferometer consists of a 2X2 coupler with two output ports connected by a length of optical fiber. Such a setup is shown in Fig. 3-7. There are two main types of Sagnac interferometer; the nonlinear-optical loop mirror (NOLM) and the nonlinear-amplifying loop mirror (NALM). These are employed in numerous applications, two of which include optical switching and modelocking of fiber lasers. This section discusses the operation of these interferometers.

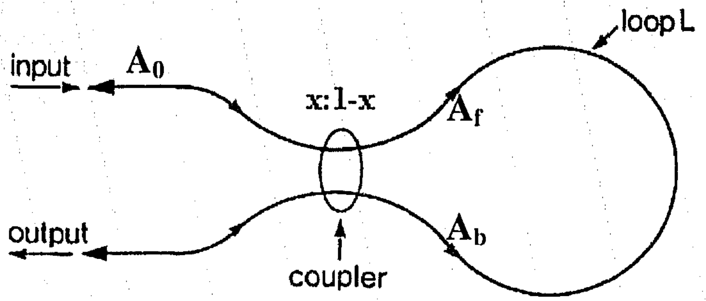

Fig. 3-7: A fiber Sagnac interferometer, A_0=input amplitude, A_f= amplitude of forward propagating field, A_b= amplitude of backwards propagating field.

A single input field entering the interferometer is split into two counterpropagating fields at the coupler. If the coupler splitting ratio is x:1-x, then a fraction x of the input power travels through the fiber loop in the clockwise direction, and the remaining fraction, 1-x, propagates in the counterclockwise direction through the loop. The transmittivity is dependent on the coupling ratio, the input intensity and the differential nonlinear phase shift between the counterpropagating beams, acquired as a result of the coupling ratio. The phase shift is acquired as a result of the interplay between SPM and XPM. The equations that govern the behaviour of the interferometer can be found in Appendix A.

For example if x = 0.5, the transmittivity is zero and the Sagnac interferometer acts as a perfect mirror reflecting 100% of the input field. This holds true for low input powers and when the loop is made up of highly birefringent fiber (i.e. polarization maintaining fiber). If the input intensity of the counter propagating beams is low, then the beams do not acquire the necessary differential phase shift required for transmission. Hence, when they interfere at the coupler all of the light is reflected back to the input. For x = 0.5, even at high input intensities the nonlinear phase shift acquired for the counterpropagating beams would be equal resulting in no relative phase difference between the beams. Hence the Sagnac acts as a perfect mirror. However by using low-birefringence fiber and a polarization controller to rotate the polarization at one end of the fiber loop, the transmission properties of the interferometer can be altered and it is made to act like a switch. This occurs through nonlinear polarization rotation, which depends on the orientation of the polarization ellipse. In short, the state of the polarization at the output fiber will be different for the counter propagating beams even though the splitting intensities are the same. When the Sagnac loop is used in this fashion it is referred to as a polarization rotation NOLM [70] and it has fast saturable absorber properties. The transmission properties can also be changed by asymmetrically placing an amplifier at one end of the fiber loop. A Sagnac interferometer that operates in this fashion is called a NALM. For low input intensities the NALM operates in the linear regime and light coupled into one port is amplified and reflected back to the input. However at high input powers, the counter propagating beams will acquire a differential phase shift as one beam is amplified at the input and hence it will acquire a higher nonlinear phase shift in propagating around the loop. Hence the transmittivity becomes a function of input power. Refer to Appendix A for further details.

Instead of using an amplifier in the loop, the same operation can be obtained by asymmetric coupling, $x \neq 0.5$. This is known as a conventional NOLM. The mechanisms involved are SPM and XPM which induces different phase shifts for the unequally split counter-propagating beams. At high input powers the nonlinear refractive index leads to a change in the optical path length and a relative phase shift for the counter-propagating beams. The asymmetric coupling at the input means that the clockwise propagating beam will experience a higher delay and phase shift than the counter clockwise propagating one. The phase shift causes destructive interference when the fields return to the coupler, which affects the ratio of the reflected and transmitted light exiting the interferometer. The result is an intensity dependent transmission; refer to Appendix A for details.

The NOLM attached to a unidirectional fiber ring forms a figure-8 shaped cavity (see Fig. 3.8). The NOLM is made up of a section of SMF28, a polarization controller that compensate for the stress birefringence of the fiber, and a variable coupler. The variable coupler allows for fine adjustment of the peak switching intensity and adjustment of the coupling ratio. The external linear loop consists of a section of EDF that provides the gain for the laser, a WDM coupler that provides the pump signal for the EDF, a polarization independent isolator to allow for unidirectional propagation and an output coupler. As pulses propagate around the linear loop, they are amplified and then split into two at the coupler. These pulses travel through the NOLM, where they are effectively shortened due to constructive/destructive interference effects when they combine at the coupler. The high intensity portions of the pulse are transmitted while the low intensity portion are reflected and rejected by the isolator.

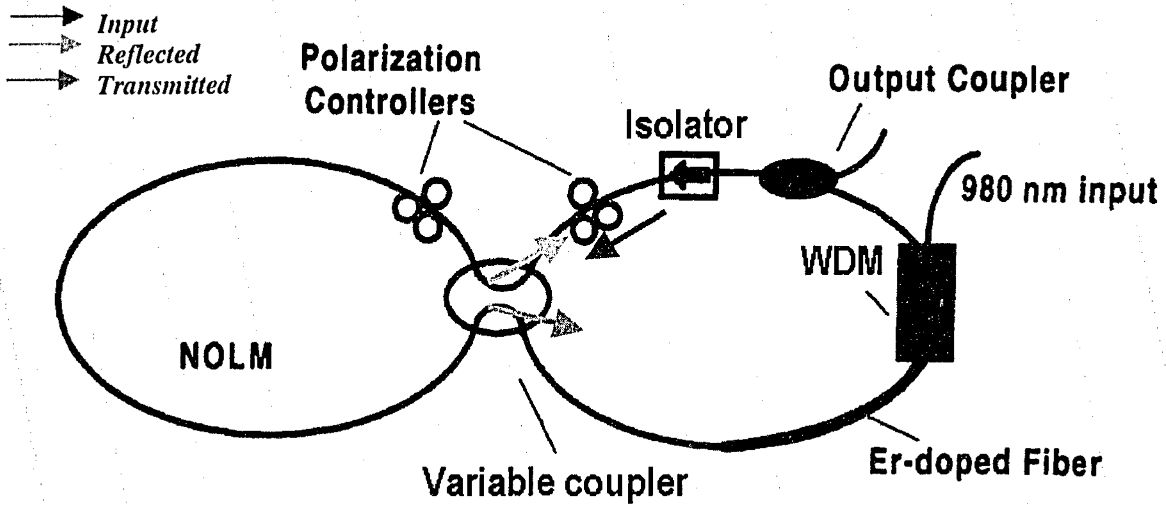

Fig. 3-8: Schematic of a figure-8 modelocked fiber laser employing a NOLM as the pulse shortening mechanism [50].

3.2 Modes of Operation of stretched pulse fiber lasers

The three main modes of operation observed for stretched pulse fiber lasers are normal single short-pulse, multiple-pulse and the noise-like pulse regime. The mode of operation depends on the polarization controller settings and the cavity parameters [73]. Pulsed operation can be obtained only if the cavity parameters are suitable. The pump power has to be increased beyond the threshold and modelocking is achieved by carefully tuning of the polarization controllers. This is a very delicate balance and careful adjustments of these parameters have to be made in order to obtain the short-pulse regime. Gong, *et al.*[73] investigated the regimes of operation for a passively modelocked fiber ring laser and they found that the threshold for the normal single-soliton regime was the lowest. This was followed by bound-solitons, and finally the threshold for noise-like pulses is the highest. They also found that the threshold for bound solitons was the same as the pump power corresponding to two single-soliton pulses existing in the cavity. The single-soliton regime is analogous to the short-pulse regime for the stretched pulse laser and two single-soliton pulses existing in the cavity is analogous to the multiple-pulse mode of operation for the stretched pulse laser. The current section briefly describes the different modes of operation while the experimental realization of these modes investigated for the stretched pulse NPR and NOLM laser will be discussed in Chapter 5.

3.2.1 Normal soliton operation

To obtain the soliton mode of operation, the net cavity dispersion has to be net negative and close to zero. If this dispersion condition is met, soliton operation is obtained by increasing the pump power above the self-starting threshold. This mode of operation is first recognized by simultaneous generation of multiple soliton pulses in the cavity. Once soliton operation is obtained the pump power can be reduced to a value below the self-starting threshold while maintaining the solitons. However below some level of pump power, modelocking is lost and the laser operates in the CW mode.

As mentioned earlier, for pump powers above the self-starting threshold many pulses exist in the cavity. This is known as the multiple-soliton state and is sometimes referred to as the bunched state [73]. In this state the solitons are usually separated by tens of picoseconds. A change in the pump power or polarization controller settings can change this state [73]. A reduction in pump power usually causes a transition from this state to the single-soliton state whereas an increase in the pump power can lead to a change in the pulse separation or can change from this state to the bound-soliton state, which will be discussed in the next section. Adjusting the polarization controller can change the pulse separation in such a way that the pulses are uniformly spaced in the cavity. This is a special case of multi-soliton operation known as passive harmonic modelocking [73].

3.2.2 Bound-soliton operation

The interaction of slightly overlapped soliton pulses can lead to the formation of bound solitons with a discrete and fixed separation [84]. If the pump power is well above threshold, the bound-soliton state can be achieved with careful adjustment of the polarization controllers. Bound-solitons behave as a unit and have properties that are similar to single-soliton pulses. They never alter their pulse separation even in the presence of small perturbations such as pump power changes and polarization changes [73].

The pulse separation can take several discrete values, which are multiples of the fundamental separation. This separation is typically in the picosecond regime [73],[77]. The autocorrelation trace of two bound-solitons is shown in Fig. 3-9. Notice that the height of the side peak is only half that of the main peak and that the separation is approximately 938 fs. This is an indication that the two bound-solitons pulses are symmetrical [73]. The autocorrelation trace for three bound-solitons separated by 1.15 ps is shown in Fig. 3-10.

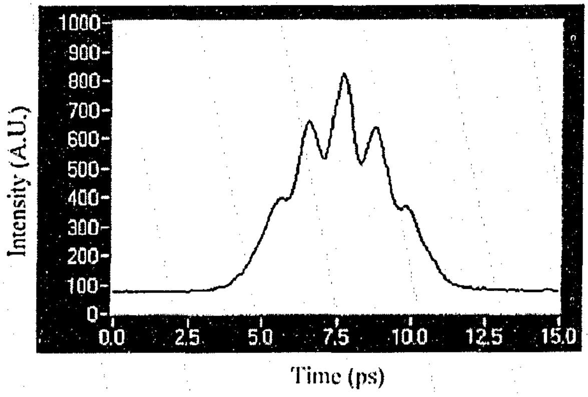

Fig. 3-9: Intensity autocorrelation trace of two bound-solitons [73].

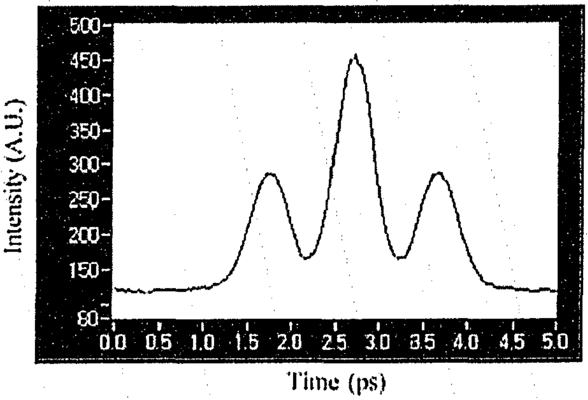

Fig. 3-10: Intensity autocorrelation trace of three bound-solitons [73].

3.2.3 *Noise-like operation*

If the pump power is increased beyond the threshold for bound-solitons and the polarization controller settings are appropriately adjusted, the noise-like mode of operation can be obtained. Another criteria for obtaining noise-like pulse is that the birefringence in the cavity has to be significant [75],[76]. The characteristics of this mode of operation are that it produces pulses with broad smooth spectra and narrow intensity autocorrelation traces that have peak to background ratios of 2:1 [75] as shown in Fig. 3-11.

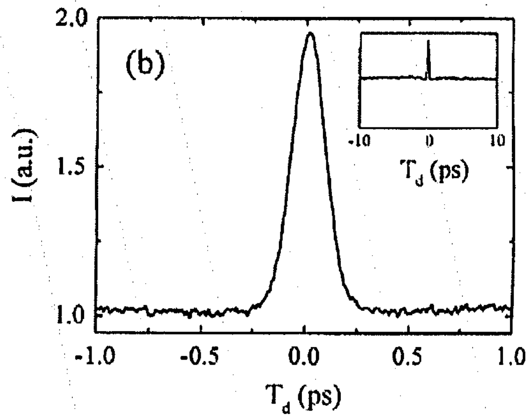

Fig. 3-11: Background free intensity autocorrelation trace for noise-like mode of operation [75].

A long-range autocorrelation trace shows that the narrow peak in Fig. 3.18 is actually a depiction of the low coherence of the output in this mode of operation [76]. Fig. 3-12 shows the long-range scan for the noise-like mode of operation. It shows a narrow coherent peak riding on a broad pulse.

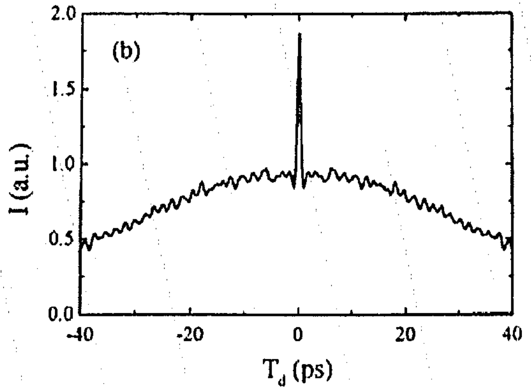

Fig. 3-12: Calculated autocorrelation trace for a noise-like mode of operation [75].

Another characteristic of this mode of operation is that the width of the narrow peak in the autocorrelation is unchanged after it propagates through a long length of dispersive medium [75]. This was attributed to the fact that the phase distortion caused by the fiber dispersion is relatively weak compared with the initial noise of the pulses and therefore has very little effect on the coherence.

In cavities where the net dispersion is small, adjusting the polarization controllers can switch between the noise-like mode and the single-pulse mode. Horowitz *et al.* demonstrated that for noise-like operation the polarization controllers were set midrange between the maximum and minimum transmittivity of the polarizer for low power signals [75].

3.3 Design of a stretched pulse NPE fiber ring laser

This section examines some of the theoretical aspects, such as the modes of operation and the challenges of the experimental implementation of a stretched pulse APM and a NOLM laser.

A simplified block diagram of a stretched pulse NPE laser is shown in Fig. 3-13.The laser consists of a gain medium section, a dispersion compensation section, a modelocking section and an output coupler.

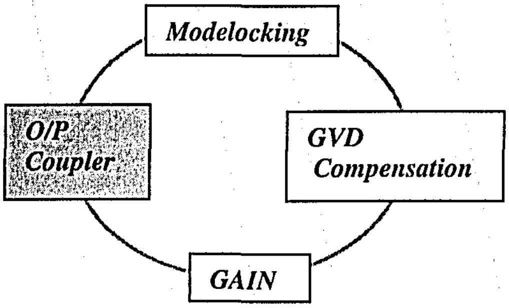

Fig. 3-13: Simple block diagram of a stretched pulse modelocked laser

3.3.1 Gain

Various single mode Erbium doped fibers (EDF) were investigated as the potential gain medium for the laser (refer to Chapter 5). The length of EDF used was determined by considering the total cavity loss and ensuring that the gain of the pumped

EDF was in excess of this loss (gain condition for CW lasing). Using an EDFA setup, the gain of the EDF was experimentally determined. The loss was estimated by taking into account the coupling losses from connectors and the losses in the modelocking section. A loss of approximately 10 dB was estimated.

The EDF is pumped in order to produce population inversion in the fiber (gain). A 980 nm diode laser producing up to 200 mW of pump power was used for this purpose. A wavelength division multiplexer (WDM) was used to couple the pump power into the fiber ring.

3.3.2 Dispersion Compensation

Standard single mode SMF28 fiber was used to provide dispersion compensation for the EDF. The dispersion was calculated and found to be –0.022 ps^2/m for SMF28 and 0.0127 ps^2/m for the EDF (see Appendix A for dispersion calculations). Based on these numbers and using (2.5), the appropriate length of SMF28 was chosen.

3.3.3 Modelocking and output coupler

A free space optical setup was designed to act both as the modelocking element and the output coupler. Recall from section 3.1.2 that a fiber laser modelocked by APM is a nonlinear interferometer with two output ports formed by the final polarizer (Fig. 3-5). The right and left hand circular polarization states are added at this polarizer such that the peak of the pulse passes through while the wings of the pulse are in orthogonal polarization and are rejected by the polarizer. Through the use of bulk components as shown in Fig. 3-14, the APM rejection port can be accessed as the output port of the stretched pulse laser, instead of using a fiber coupler to extract energy from the ring. This improves the laser performance by reducing the cavity loss and has been found to result in higher output powers. The pulses from the rejected port are of relatively high quality if the nonlinear phase shift required for modelocking is small [51]. The rejected pulse is usually longer than the intracavity pulse, but the rejected output power can be as much as 50% of the intracavity power when the laser is biased to the point where there is a large loss for low intensities [51].

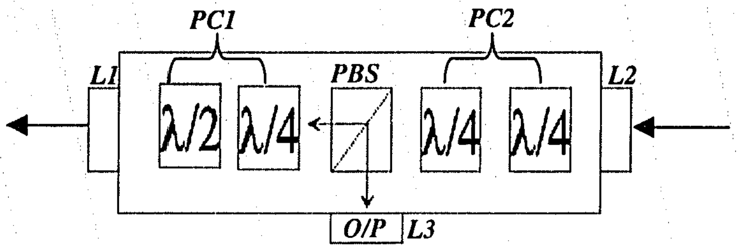

Fig. 3-14: Block diagram of APM section using bulk optics. PBS - polarization sensitive beam splitter (APM port), PC1 & PC2 – polarization controllers 1 and 2 and O/P is the output (APM rejection port). L1,L2 and L3 are collimating lenses.

The PBS acted as both the polarizer and the output port of the laser. The first polarization controller (PC1) takes the linearly polarized light from the PBS and converts it into an elliptically polarized state for propagating through the fiber. The second polarization controller (PC2) takes the Kerr rotated state from the fiber and converts it back to the desired polarization prior to the PBS. This controller is used to bias the laser so that the low intensity parts of the pulse acquire large losses.

Finally, an isolator is used to provide unidirectional propagation within the laser cavity. Lasers in a unidirectional ring configuration have been shown to self-start more easily by reducing spurious reflections off polished fiber ends or bulk elements [52]. A polarization independent fiber isolator was chosen, but a free space isolator could also be used if placed in the free space section.

3.3.4 *Implementation of the laser*

A complete schematic of the experimental setup of the stretched pulse APM laser is shown in Fig. 3-15. The lengths of fiber used were varied corresponding to cavity lengths from 4 to 20 meters, until the optimum output was achieved (refer to Chapter 5). When determining the cavity length, the phase condition for lasing, discussed earlier, had to be considered. The cavity had to be long enough so that many longitudinal modes would fit within one round trip of the cavity. However the cavity could not be too long or stable modelocking would become difficult, as will be discussed in Chapter 5.

The order in which each component is placed in the ring relative to the direction of operation is important. The pulse dynamics were experimentally investigated in [22]&[66] to determine the optimal location for the output APM port and the direction in which the ring should be operated. A stretched pulse laser was operated in the forward direction similar to Fig. 3-15 as well as in the reverse direction by reversing the order of the bulk components and the direction of the isolator. The pulse dynamics were investigated [22] for both directions of operation at 3 different locations in the ring: before the modelocking section, after the modelocking section and between the SMF28 fiber and the EDF. In both directions of operation, the optimum point for the output was immediately after the EDF, since the pulses had the broadest bandwidth and highest energy here. In the reverse direction, detrimental pulse shaping and structure of the spectrum was observed. This was possibly due to soliton effects due to high powers in the negative dispersion (SMF28) fiber located immediately after the gain (EDF) medium. However in the forward direction, clean smooth pulses were observed. It was concluded that a stretched pulse laser should be operated in the forward direction with the output APM port placed immediately after the gain fiber to keep the regions of highest intensity within the positive GVD fiber.

In this configuration, the amplifier (EDF) was pumped in the counter-direction. This was to ensure that there was minimal residual 980 nm light in the output. Any pump in the output would skew the results from the autocorrelation experiment, which will be discussed in Chapter 4. Counter-directional pumping showed an increase in the gain, as predicted from theory [34]. Theory also predicts a degraded signal to noise ratio with counter-directional pumping. However, this was not investigated as there did not appear to be a significant effect on the pulse quality (i.e. the pulses were quite stable). If pumped co-directionally, employing a second WDM to act as a filter could eliminate any residual 980 nm. However this would add another component to the ring and thus increase the intracavity losses and the cavity length.

The placement of the isolator is not as crucial; it could be placed before or after the SMF28 fiber. A bulk isolator placed in the free space section can also be used [53].

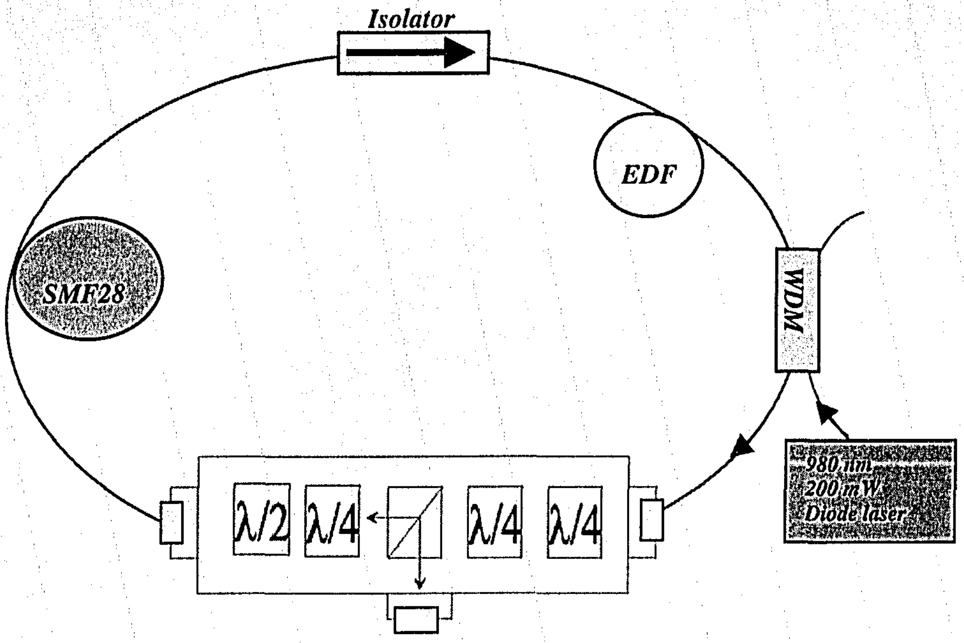

Fig. 3-15: Schematic of the experimental configuration for a stretched pulse APM fiber laser.

3.3.5 Components

In this section, the individual components that were used in the laser are described. Fig. 3-16 shows a picture of the laser with the individual components clearly labeled.

3.3.5.1 Free space section

The bulk optics free space section is shown in Fig. 3-17. The light was coupled out of the fiber into free space and back into the fiber again using Fiberports manufactured by Optics For Research (OFR). These are ultra-stable miniature micropositioners that allow for fine adjustment of an aspheric lens embedded in the assembly. They allow for coupling between a collimated free space beam and a fiber. The aspheric lens in the fiber port is antireflection (AR) coated at the wavelength of interest (1550 nm). The waveplates are OFR zero-order retarders, with all surfaces AR coated. The retarders are mounted in a rotation cell with engraved angle index. The quarter-waveplate and half-waveplate form the first polarization controller. If the quarter-wave was set at an angle between 0° and 45°, it converted the linearly polarized light from the PBS into elliptically polarized light. The angle of the half-waveplate was then set to rotate the ellipse so that it could be aligned relative to the slow and fast axes of the fiber. Two quarter-waveplates form the second polarization controller. This controller rotates the plane of polarization of the ellipse coming out of the fiber so that the peak of the pulse passes through the PBS while the wings are rejected. A half-waveplate could be used instead of two quarter-waveplates; however using two quarter-waveplates gave more flexibility in biasing the laser. The PBS is an OFR IR polarization beamsplitter. The p-polarized component was transmitted while the s-polarized component was reflected at 90°. The dispersion in the free space section was assumed to be negligible relative to the dispersion of the various fibers in the ring.

3.3.5.2 Fibers

Nufern EDF555 erbium doped fiber, with an emission-band around 1535 nm, was one of the EDFs used to provide the gain. It has a numerical aperture (NA) of 0.20 and a mode-field-diameter (MFD) of 4.6 at 980 nm and 7.4 at 1550 nm. The peak absorption is 8.7 dB/m at 1530 nm and GVD was estimated to be 0.0127 ps^2/m at 1550 nm. In order to compensate for the GVD of the EDF, corning SMF28 fiber was used. It has a GVD of -0.022 ps^2/m at 1550 nm.

There was one other type of fiber used within the cavity; Flexcor1060. This is the fiber used for the pigtails on the WDM. It has an NA of 0.14 and MFD of 5.9 at 980 nm and 9.9 at 1550 nm. The GVD for this fiber is relatively low; it was approximated to be 0.007 ps^2/m at 1550 nm wavelength.

3.3.5.3 Optical pump and WDM coupler

The optical pump was a 980 nm wavelength, 200 mW CW EDFA pump laser, packaged by TRLabs. This unit housed a SDL Optics high power 980 nm semiconductor diode laser module. To transfer the pump energy from the laser to the cavity requires a WDM. A SIFAM 980/1550 coupler was used. It has an insertion loss of 0.02 dB between the input and the outputs and isolation greater than 12 dB between the output ports. The fiber type used for the pigtails was Flexcor1060. Although the dispersion of the Flexcor1060 was fairly low, it had to be taken into account when determining the lengths of SMF28 required to balance the dispersion within the cavity.

As can be seen from Fig. 3-16, there are two WDMs used in the cavity. This allowed us to test the laser with both co-directional and counter-directional pumping. The second WDM was needed to eliminate any residual 980 nm light from the output when pumping co-directionally. This WDM was later removed, as it was concluded that counter-directional pumping gave the best results.

3.3.5.4 Isolator

The isolator permits light to pass through in one direction (marked with an arrow on the device). A MP Fiberoptics Inc. polarization independent fiber isolator was used. It has an insertion loss of 0.44 dB and isolation of 58 dB. The fiber type used for the pigtail was SMF28. Again this length of SMF28 had to be taken into account when balancing the dispersion in the laser cavity.

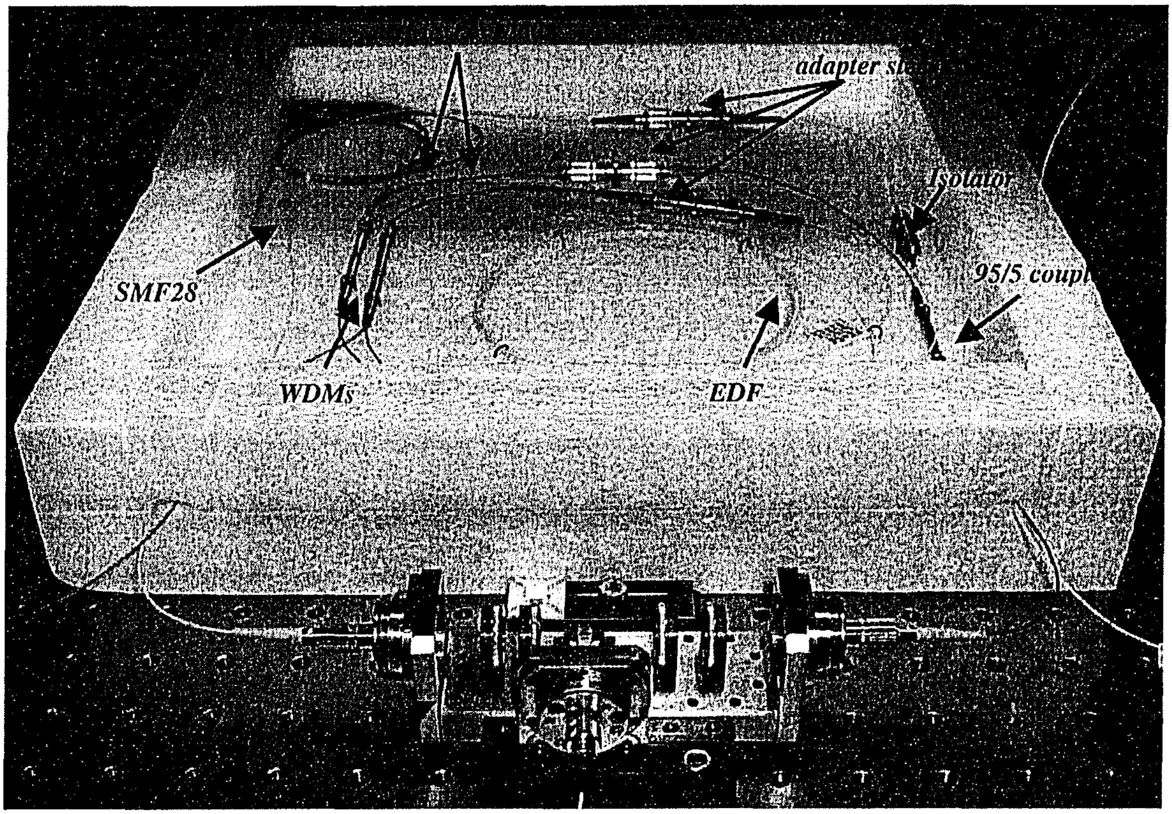

Fig. 3-16: Picture of the stretched pulse laser with the individual components labeled.

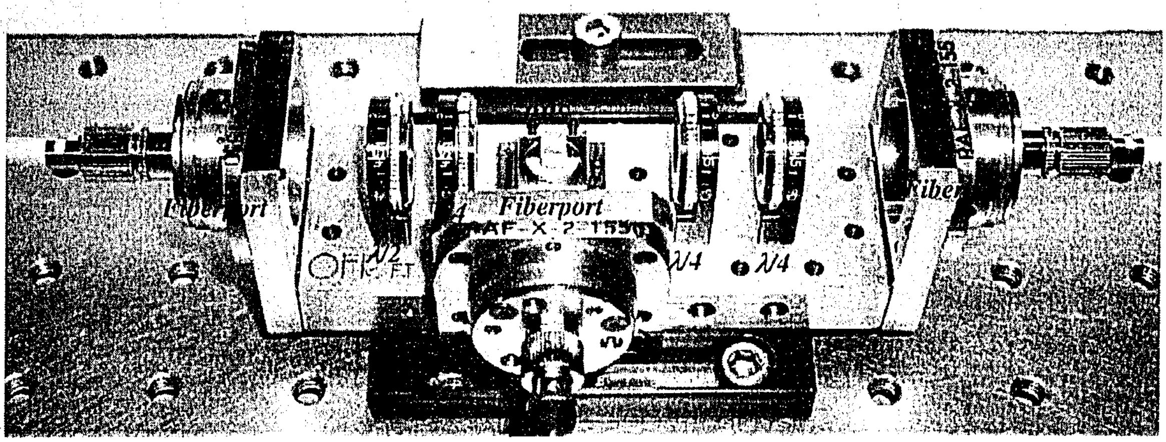

Fig. 3-17: Bulk optics modelocking section of the laser consisting of 3 fiberports, a polarizing beamsplitter, 3 quarter waveplates and a half waveplate that forms the polarization controllers.

3.3.5.5 Additional components

A 95/5 coupler was used as a diagnostic tool to investigate the pulse within the cavity prior to the free space section. This coupler acted as eyes inside the cavity and allowed us to optimize the various lengths of fiber and the waveplates settings for maximum output. It was later removed when the cavity was nearly optimized.

Finally instead of splicing the fibers together, connectors and adapter sleeves were used to connect the fibers. This increased the losses but offered the benefit of allowing easy changes to the fiber lengths.

3.4 Design of a figure-8 laser using a NOLM

The design considerations for a NOLM laser are very similar to those for the stretched pulse laser discussed in Section 3.3. The linear ring is very similar to the one in Fig. 3-15, minus the free space section. All of the components are the same with the addition of a 20% output coupler and a fiber polarization controller placed inside the loop as can be seen in Fig. 3-18.

3.4.1 Gain

The gain section is identical to that of the stretched pulse laser discussed in section 3.2.3. Nufern555 single mode EDF was used to provide the gain, and the length was chosen such that the gain exceeded losses in the cavity. The EDF was pumped using a 980 nm diode laser via a WDM.

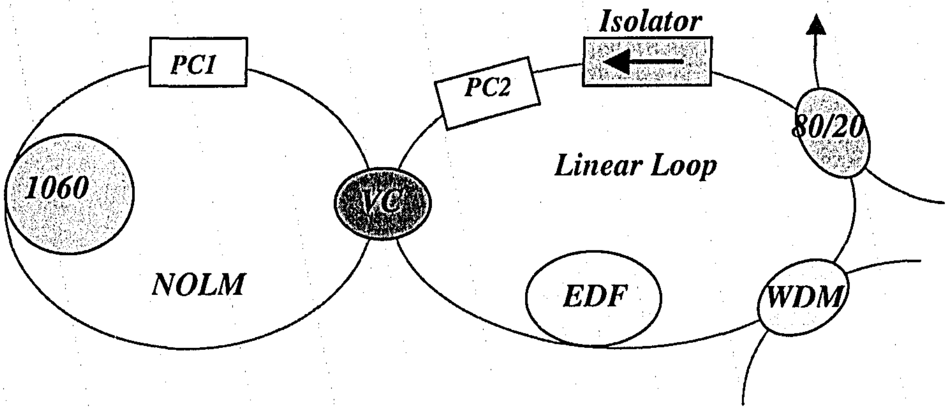

Fig. 3-18: Schematic of the experimental configuration for the stretched pulse figure-8 NOLM laser. PC1 and PC2 – polarization controllers, EDF – Erbium doped fiber, VC – Variable coupler, 1060 – Flexcor1060 fiber and WDM – Wavelength division multiplexed coupler.

3.4.2 Dispersion compensation

Lengths of SMF28 from the fiber pigtails of the output coupler, isolator, and variable coupler provided the dispersion compensation. The length of Flexcor1060 in the NOLM and the pigtail from the WDM were also taken into account when considering the dispersion.

3.4.3 Modelocking

The APM action for this laser is provided by the NOLM. Recall from section 3.1.2 that the principle of modelocking by APM is pulse shortening by the addition of two versions of the same pulse. A laser modelocked by APM is thus essentially a nonlinear interferometer. In the NOLM, a variable coupler provides the interferometric action. The addition of the two counter-propagating pulses takes place at the output of the NOLM where the two arms meet at the variable coupler.

The length of the Flexcor1060 was chosen such that the total dispersion of the laser cavity would be slightly net negative (anomalous), i.e. almost balanced. This essentially creates a stretched pulse fiber laser with a NOLM. Recall from section 3.1.2 that the pulse energy in fiber lasers is limited by excessive nonlinearity, which arises from the soliton dynamics and overdriving the NPE. The stretched pulse technique addresses the soliton dynamic issues and the NOLM addressed the overdriving the NPE. The NOLM operates with a nonlinear phase shift accumulated only in the nonlinear loop; as a result, overdriving the NPE can be avoided by using a shorter nonlinear loop.

Typically, dispersion shifted fiber (DSF) is used in these lasers in an attempt to keep the total dispersion as small as possible [73]. Flexcor1060 was used here, as DSF was not available. The dispersion of Flexcor1060 is approximately 0.007 ps^2/m, which is low relative to SMF28. The length of the NOLM was also much shorter than most other lasers of this type, thereby indirectly reducing the net cavity dispersion. Recall from section 3.13 that the use of low birefringence fiber in the NOLM can lead to nonlinear polarization rotation. By shortening the NOLM this effect is reduced and it ensures that the dominant nonlinear effects are SPM and XPM.

The remaining components are the isolator, polarization controllers and the output coupler. A polarization independent isolator was used to provide unidirectional propagation. Fiber polarization controllers were used to compensate for birefringence in the fiber. Finally an 80/20 fiber coupler was used for the output.

3.4.4 Components

This section takes a detailed look at the individual components used in the NOLM laser. Fig. 3-19 shows a picture of the laser with the individual components clearly labeled. Most of the components used in this laser are identical to the ones used in the stretched pulse NPE laser discussed in section 3.2.2, therefore these components will not be repeated.

All of the fibers used in this laser are identical to the ones used in the stretched pulse NPE laser discussed above. The lengths of fibers used were varied depending on which EDF was used as the gain medium and the length. Furthermore the optical pump, WDM and isolators are also identical to the ones discussed in section 3.2.3.

The output coupler and variable coupler are unique to this laser. The output coupler is a Fiberconn Technology 80/20 1X2 coupler. It has a maximum insertion loss of 1.11 dB and minimum return loss of 55 dB. The fiber used in the coupler is SMF28. The pigtails on this component were cut back to ½ m on each side in an attempt to keep the ring relatively short and reduce the dispersion. The variable coupler used is a Canadian Instrumentation and Research 2X2 variable fiber coupler. It is designed so that varying the micrometer can vary the coupling ratio from 0 to 98%. The type of fiber used for this coupler is also SMF28. The pigtails on this coupler were also cut back so as to keep the dispersion low, especially in the NOLM section of the laser.

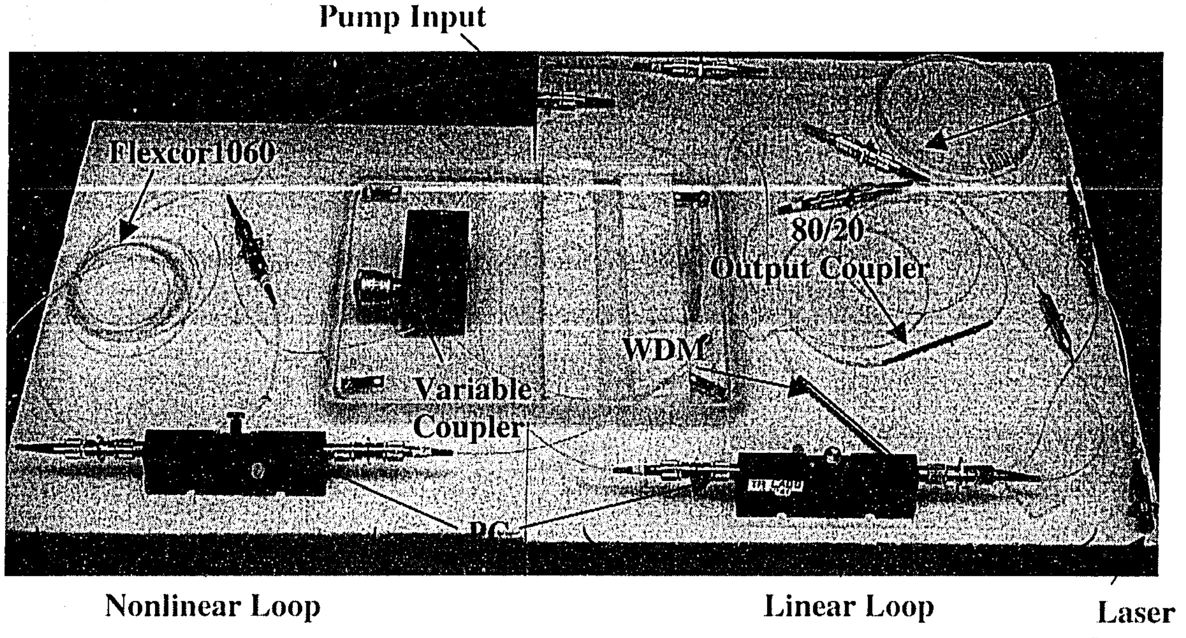

Fig. 3-19: Picture of the stretched pulse figure-8 fiber laser with NOLM. The individual components are labeled. PC – Polarization Controller.

3.5 Active modelocking of fiber ring lasers

Active modelocking in fiber ring lasers typically employs either an amplitude (AM) or phase (PM) modulator in order to "lock" the modes of the laser together. AM modulation will be the focus of this discussion. For details on PM modulation and other active modelocking techniques refer to [85].

In AM modulation, the amplitude of the intracavity optical field is modulated at a frequency f_m that is equal to or an integer multiple of the mode spacing Δ. In the time domain the modelocking process can be described using Fig. 3-20. Assume that the laser begins to oscillate in the form of a short pulse that circulates inside the cavity, passing through the modulator on each round trip just at the instance when the modulator transmission is high but loss is low [38]. The modulator provides a time dependent periodic loss which is modulated at f_m. As well, since the laser generates more light at the loss minima [38] the intracavity field is also modulated at the same frequency, thus producing a train of pulses.

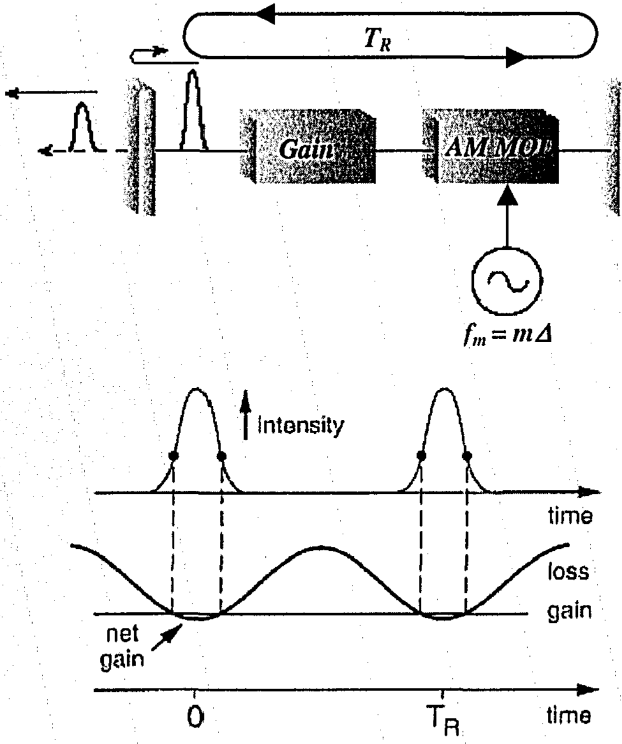

Fig. 3-20: Simplified schematic of a laser actively modelocked by an AM modulator. The lower figure shows the pulse in the time domain and the time dependence of the gain. T_R is the round trip time or repetition rate of the laser. [21]

For the frequency domain description of active modelocking, each of the oscillating modes in the cavity are said to acquire modulation sidebands as a result of the modulator [85]. The modulation frequency is equal (or very close) to the mode spacing or an integer multiple of it. Hence the modulation sidebands from each mode fall on top or very close to one of the other modes in the cavity. Each of these sidebands will tend to "injection-lock" the mode with which it is in resonance [85]. Thus modulation will tend to "modelock" each mode to one or more of its neighboring modes.

Active modelocking when the modulation frequency is an integer multiple (m) of the mode spacing is called harmonic modelocking [85]. Harmonic modelocking couples together sidebands which are spaced m mode intervals apart, and can lead to the production of up to m individual pulses circulating around the cavity, separated by equal time intervals of T_R/m [85]. Harmonic modelocking is typically used to increase the repetition rate, and/or to shorten the modelocked pulses [21].

3.6 Design of an actively modelocked fiber ring laser

A schematic of the actively modelocked laser that was designed is shown in Fig. 3-21. The laser was built with non-polarization maintaining fiber optic components. Two isolators were used to provide unidirectional propagation and to prevent reflections from the modulator. Active modelocking was realized by periodic modulation of the cavity loss using a Mach-Zehnder modulator driven by a sinusoidal radio-frequency (RF) signal from a synthesizer. A polarization controller (PC) was used at the input of the modulator, since it was sensitive to polarization. Pumping 10 m of 3M EDF with a 980 nm diode laser at 100 mW provided the cavity gain. Two wavelength division multiplexed couplers were used to allow for both forward and reversed pumping, and finally, the output was taken using a 20% coupler. The pigtails in the cavity consisted of 9 m of SMF28 and 3 m of Flexcor1060, making the total cavity length approximately 22 m.

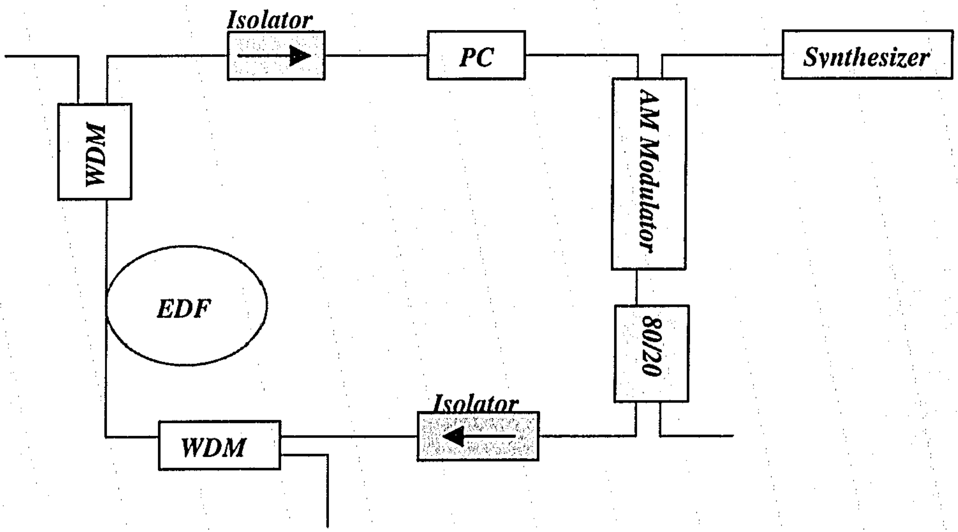

Fig. 3-21: Schematic of experimental configuration for the actively modelocked fiber ring laser.

The details of the individual components are identical to the ones discussed for the stretched pulse lasers with the exception of the EDF and the modulator, which are unique to this laser. 3M C-band EDF, with an emission band around 1535 nm, was used to provide the gain in the cavity. It has a NA of 0.26 and a MFD of 5 μm at 1550 nm. The peak absorption is 6-8 dB/m at 1530 nm and the GVD was estimated to be 0.08 ps^2/m. A 20 GHz UTP $LiNbO_3$ Mach-Zehnder electro-optic modulator was used to provide the amplitude modulation. The insertion loss of the modulator was estimated to be approximately 3 dB.

Unlike the passively modelocked cavities, the length of this cavity was significantly longer and the dispersion was much higher. Typically cavities of this type are tens to hundreds of meters long and the dispersion is largely positive [86],[87]. In these cavities dispersion is used, (instead of wavelength selective elements such as fiber Bragg gratings) to achieve wavelength tunable operation. Li and Chan [87] showed that once the laser is modulated at the fundamental or one of its harmonics, the emission wavelength of the laser can be tuned by changing the modulation frequency. They also show that if modulated at the proper harmonic the laser can produce not only single wavelength tunable pulses, but also multi-wavelength tunable pulses. This was investigated and the results are shown in Chapter 5.

4 Design and test of an interferometric autocorrelator

The femtosecond time scale is beyond the range of standard electronic instruments such as oscilloscopes. The absence of fast photodetectors with a large enough bandwidth has led to the development of alternate techniques for measuring the temporal characteristics of femtosecond pulses.

There are purely electronic methods [63] of recovering the pulse envelope, but they are limited to pulses in the order of hundreds of femtoseconds. Alternative all-optical methods are available, one of which is based on the autocorrelation technique. This technique is most flexible as it is not limited to a particular range of pulse duration. Autocorrelation is a measure of how similar a pulse is to a delayed version of itself, as a function of the delay. It is typically used in characterizing random signals and is somewhat limited since phase information is not easily extracted. Nevertheless, it is widely used because of its relative simplicity.

The Fourier transform of an autocorrelation function is known as a power spectral density. This is analogous to a magnitude plot from a Fourier series. Without the corresponding phase plot, the time domain waveform can only be estimated. As such, pulses with very different pulse shapes can have very similar autocorrelations. Thus, autocorrelation can be used to estimate pulse duration only by assuming a pulse shape. The pulse duration is estimated from the ratio between the FWHM of the autocorrelation and that of the assumed pulse shape.

There are two autocorrelation techniques that can be used to characterize ultrashort pulses: intensity autocorrelation and interferometric autocorrelation. These are also sometimes called fast and slow autocorrelation, respectively. The intensity autocorrelation [64] does not provide any phase information but allows for a straightforward estimate of the pulse duration. Conversely, the interferometric autocorrelation yields the pulse duration as well as providing some information about the pulse phase.

4.1 Interferometric autocorrelation

Mathematically the correlation function is usually described given two time dependent functions *F(t)* and *F'(t)*. If one function *F'(t)* is already known, the other function can be obtained by the measurement of *G(τ)* (the first order correlation) and is given as:

$$G(\tau)=\int_{-\infty}^{\infty} F'(t)F(t-\tau)dt \tag{4.1}$$

In measuring ultrafast laser pulses, an appropriate test function F'(t) is not available, so the pulse is used as its own test function. Since the pulse itself is the test function, this is called autocorrelation; the pulse is being correlated with itself. The laser pulse is split into two replicas *F'(t)* and *F(t-τ)*, to be compared within an interferometric setup able to construct the autocorrelation function. The arm imbalance between the two paths inside the interferometer (Fig. 4-1) provides the delay τ in the mathematical expression. The optical pulse is split into two pulses of equal power (ideally) by a symmetric beamsplitter. The pulses are delayed with respect to each other by a variable delay. At the output of the interferometer, the pulses are combined and sent collinearly to the detector. In the femtosecond regime, any finite angle between the pulses is accompanied by a geometrically induced relative delay across the beam.

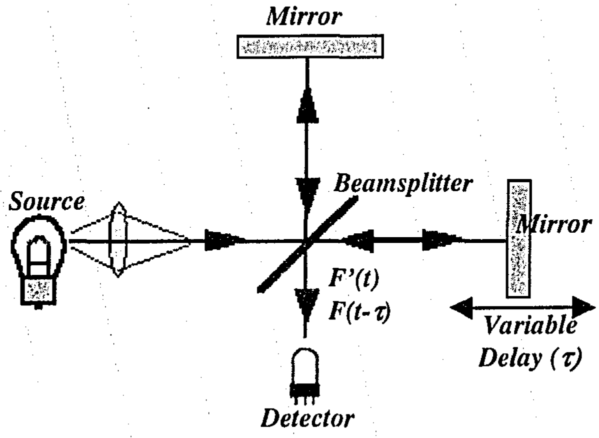

Fig. 4-1: Basic interferometric autocorrelation setup (Michelson interferometer). The path-length in one arm is varied by a moving mirror. The pulse is split by the beamsplitter, the two versions of the pulse propagate through different path lengths, then are recombined at the beamsplitter, and sent collinearly to the detector.

Usually the intensity *I(t)* of the pulse is to be characterized, where $I(t) \propto \left\langle E(t)E^{*}(t) \right\rangle$ and *E(t)* is the complex amplitude of the pulse. If a linear detector is employed, the interferometric output of the setup shown in Fig. 4-2 is given by[62]

$$g_1(\tau) = 1 + \left\{ \int_{-\infty}^{\infty} E(t)E(t-\tau)dt \right\} \cos(\omega_0 \tau) \qquad (4.2)$$

This is known as the first order autocorrelation and it gives an approximation of the pulse duration if a pulse shape is assumed. Fig. 4-2 shows a typical first order autocorrelation scan simulated using Matlab.

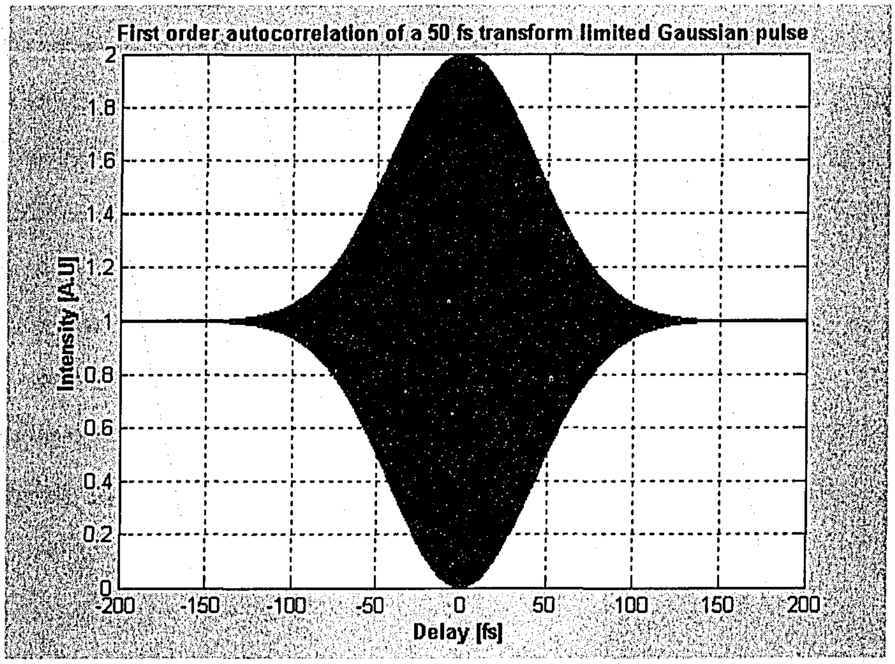

Fig. 4-2: First order autocorrelation 50 fs Gaussian pulse. (See Appendix B for calculation details.)

To acquire phase information, the second order autocorrelation needs to be examined. Mathematically this is expressed as follows [62] (refer to Appendix A for details):

$$g_2(\tau) = 1 + 2G_2(\tau) + \left\{ 4\int_{-\infty}^{\infty} E^3(t)E(t-\tau)dt \right\} \cos(\omega_0 \tau) + G_2(\tau)\cos(2\omega_0 \tau) \qquad (4.3)$$

where $G_2(t)$ is the fringe average or intensity autocorrelation.

Experimentally the second order autocorrelation function can be obtained using either two-photon absorption [63] or second-harmonic generation [64]. The two-photon absorption process that takes place in a semiconductor detector when excited at a wavelength below its bandgap can be used to generate the second order response. Only the high peak power from ultrashort pulses can produce a significant two-photon signal, which can be directly recorded on an oscilloscope as a function of the delay τ. Alternately, a phase-matched nonlinear crystal that is properly filtered to provide only the second harmonic generation field can be used to provide the second order signal. This harmonic field, recovered typically by a linear photodetector as a function of delay, will give the same result as the two-photon process.

When the amplitude and phase dependence of the fields are substituted into equation (4.3) and the second order autocorrelation function is decomposed, some interesting properties of the interferometric autocorrelation are revealed [64]. An important conclusion is that the peak to background ratio for the interferometric autocorrelation is 8 to 1 (Fig. 4-3) when all of the terms of the autocorrelation are recorded.

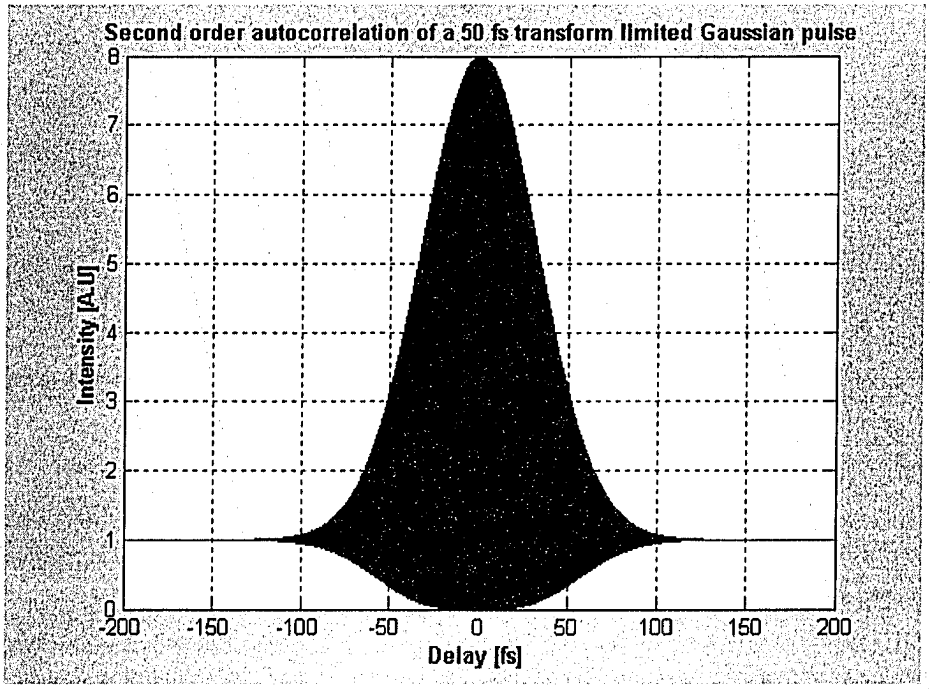

Fig. 4-3: Second order autocorrelation 100 fs pulse. (See Appendix B for calculation details).

It is known that at zero delay the autocorrelation signal is at a maximum as the pulses are perfectly overlapped. For a delay increment of half the light period, the two fields add with opposite phase resulting in a near zero signal (destructive interference). For delay times of more than the total pulse length, the two pulses are no longer overlapping and the autocorrelation shows a constant background signal. This demonstrates that the interference pattern or fringe (intensity pattern) provides a direct and accurate self-calibration of the measurement

There are other methods of charactering femtosecond pulses such as frequency resolved optical gating (FROG) [64] and third harmonic generation interferometry [49]. Typically these methods provide more information than the interferometric autocorrelation. However, they are more complicated and more difficult to implement. For more details on these methods, refer to the [64].

4.2 Design considerations for the autocorrelator

The major considerations when designing an autocorrelator are as follows: the configuration of the interferometer (collinear or noncollinear), the scanning mechanism for the delay, and the detection scheme.

There are typically two detection methods that can be used when designing an interferometric autocorrelator: two-photon absorption in a semiconductor photodiode or second harmonic generation in a nonlinear crystal. The two-photon absorption method is attractive as it does not require phase matching, which is necessary when using a nonlinear crystal. Furthermore, by using a photodiode the second order response and the transformation of light into an electric signal is combined into one solid-state device. However finding the appropriate commercial photodiode can prove to be difficult as the active area of the detector must be fairly thick, as will be discussed later. On the other hand there are various proven nonlinear crystals that are appropriate for this type of application. Both schemes were investigated and will be discussed in the following sections.

4.2.1 Configuration

The noncollinear configuration can only give the intensity autocorrelation while the collinear configuration gives either the interferometric or intensity autocorrelation. For the reasons discussed earlier, an interferometric autocorrelation was preferred and hence the collinear configuration was used.

4.2.2 Scanning mechanism

The delay arm of the interferometer is typically scanned either very rapidly using a shaker or loudspeaker, or very slowly using a linear motor. The slow scan using a linear motor was implemented here. When working in the femtosecond regime, rapid scanning can sometimes be troublesome as it can cause slight misalignment of the interferometer resulting in erroneous results. Using a slowly scanning linear motor eliminates this possibility.

4.2.3 Suitable photodiode/detector

The detector used should be made of a material that has a bandgap (E_g) in the range of ($h\upsilon$,$2h\upsilon$). This is to ensure that the photodiode has a small one-photon response but a large two-photon response at the wavelength of interest. A Si photodiode is an excellent candidate for 1550 nm wavelength [55]. Silicon has an E_g of approximately 1.12 ev, which is about 1.4 $h\upsilon$ at 1550 nm. A Si avalanche photodiode (APD) was tested to determine its suitability for use as a two-photon absorber. It was hoped that the internal gain provided by the APD would result in larger two-photon photocurrent and therefore improved sensitivity.

4.2.4 Nonlinear Crystal

Based on availability and cost, a Barium Borate (BBO) crystal was chosen as the second harmonic crystal for use in the autocorrelator. To determine its suitability for use in the autocorrelator, various calculations were performed in order to find the phase matching angle, thickness and efficiency of this crystal. The calculation details can be found in Appendix A. The phase matching angle was found to be approximately 20^{o}, the optimum crystal length was found to be 7.8 mm and the efficiency was found to be $2*10^{-4} P^{(\omega)}$, where $P^{(\omega)}$ is the peak power of the fundamental or input signal.

4.3 Implementation of the Autocorrelator

The schematic of the interferometric autocorrelator that was implemented is shown in Fig. 4-4. The output pulse train from the laser is coupled into the autocorrelator using a collimator. To ensure equal delay in each arm, special care had to be taken to ensure that the two beams passed through the same thickness of glass. Hence, two identical nonpolarizing beamsplitters were used to split and recombine the pulses. This ensured that the dispersion in each arm was the same. The displacement of the beam after passing through the beamsplitter was accounted for in the beamsplitter assembly (Fig. 4-6). Retro-reflectors were used instead of standard mirrors as they are more flexible to work with and more forgiving to slight misalignment of the beams. Two-photon absorption and second harmonic generation scales with the optical intensity (Refer to appendix A for details). Therefore a lens was used to focus the collinear beams onto the detector in an attempt to increase sensitivity. The delay was scanned using a linear motor mounted on a stage, which was controlled using labview. The autocorrelator was designed so that when the stage is in its center position, the two paths are approximately equal in length and the pulses from each arm are overlapped in time.

In this section the individual components that made up the autocorrelator are discussed. Fig. 4-5 shows a picture of the autocorrelator with the various components clearly labeled. The entire assembly was enclosed in a stainless steal box to reduce stray light levels.

4.3.1 Fiberport

The output from the laser is coupled into the autocorrelator using an OFR fiberport. The free space beam produced by the fiber port is well collimated with a diameter of 0.5 mm.

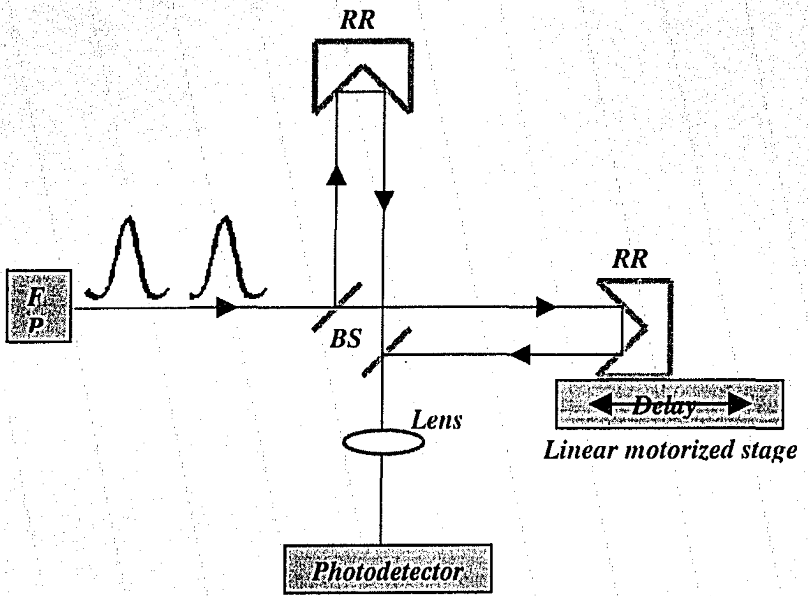

Fig. 4-4: Schematic of an interferometric autocorrelator. FP-fiberport (collimator), BS– beamsplitter and RR – retroreflector.

4.3.2 Beamsplitter

Lambda research optics non-polarizing 2 mm thick plate beamsplitters were used to split and recombine the beams. These beamsplitters were coated so that the s and p polarization components coincide in reflectance at 1550 nm. That is, the beamsplitter does not alter the state of polarization of the incoming beam. The beamsplitters were also antireflection coated at the same wavelength on the back face. The beam splitting and combining occurs at the dielectric layer. Fig. 4-6 shows the beamsplitter assembly with a closer look at the beamsplitter setup. The top beamsplitter splits the input beam while the bottom beamsplitter combines the beams reflected from the retroreflectors.

4.3.3 Photodetector/Nonlinear Crystal

A Hamamatsu Si APD was used as the two-photon absorber. The detector has a response from 400 nm to 1100 nm with a peak at 800 nm, thus making it an ideal candidate for two-photon absorption of 1550 nm as discussed in section 2.6.4.

A 5 mm type I BBO crystal cut at $\theta = 22.8^\circ$ and $\phi = 0^\circ$ was used along with a bandpass filter and Si detector for the second detection scheme.

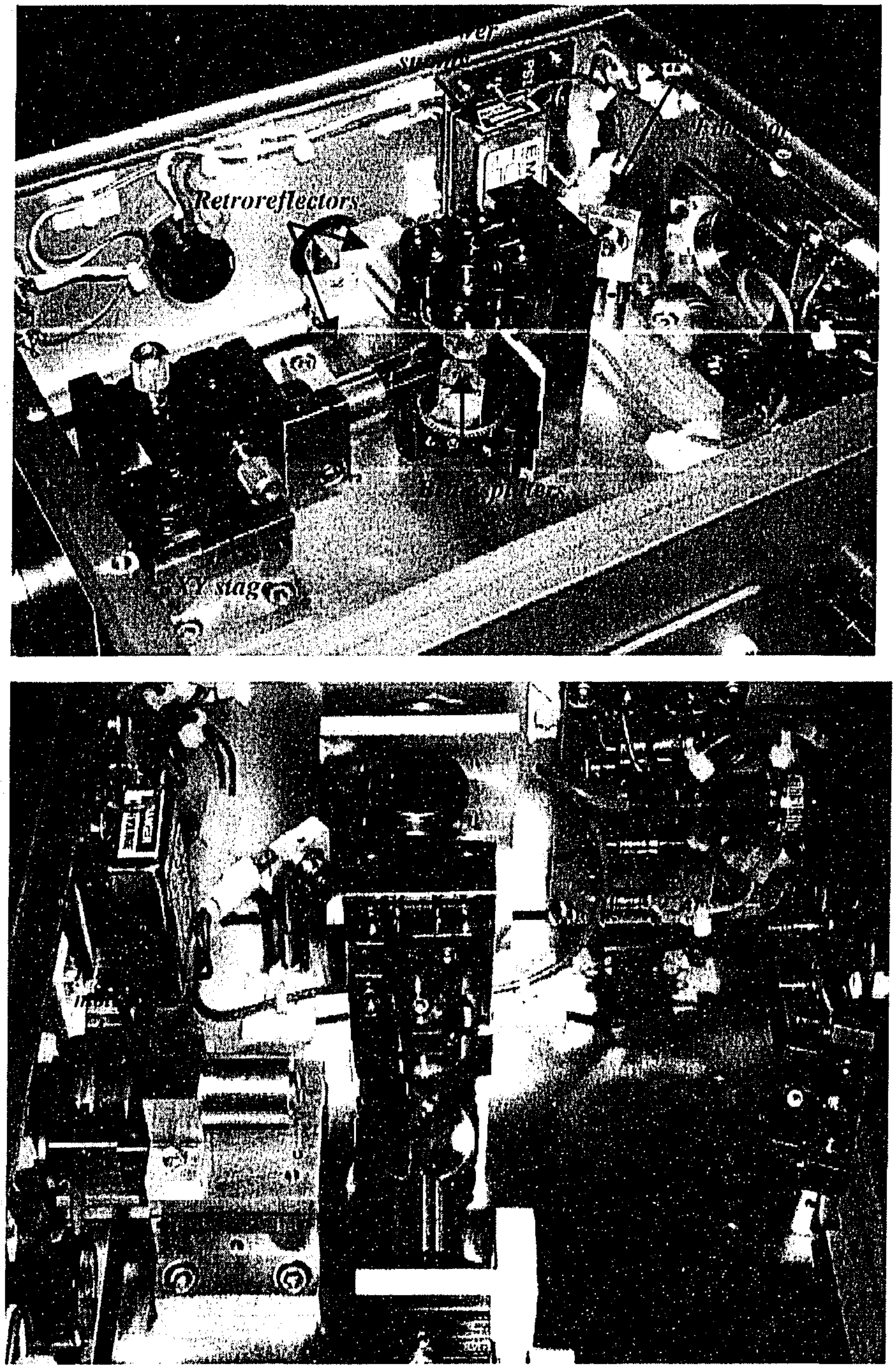

Fig. 4-5: Picture of the interferometric autocorrelator (top and side view) with the various components outlined.

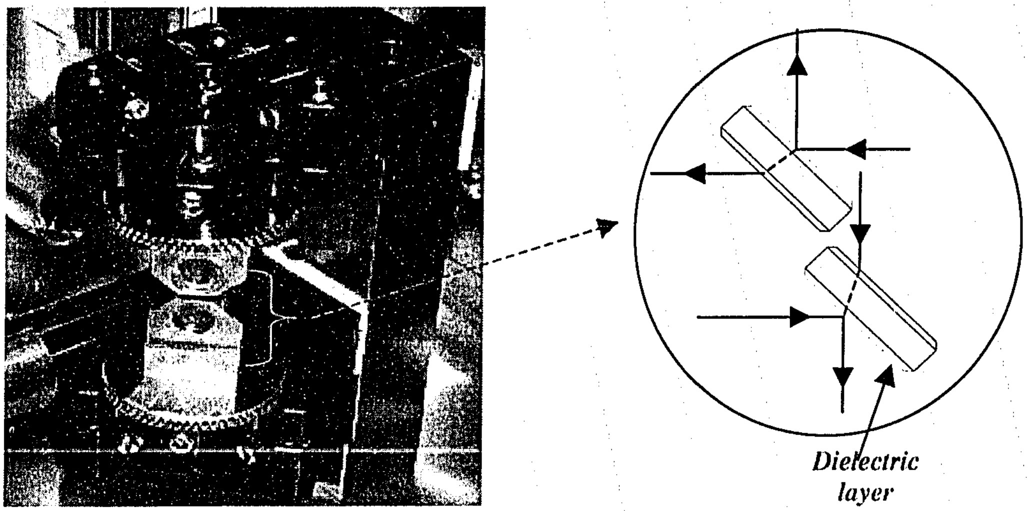

Fig. 4-6: Picture of the beamsplitter assembly. The beam is split at the top beamsplitter and then recombined at the bottom beamsplitter after propagating through the two arms of the interferometer.

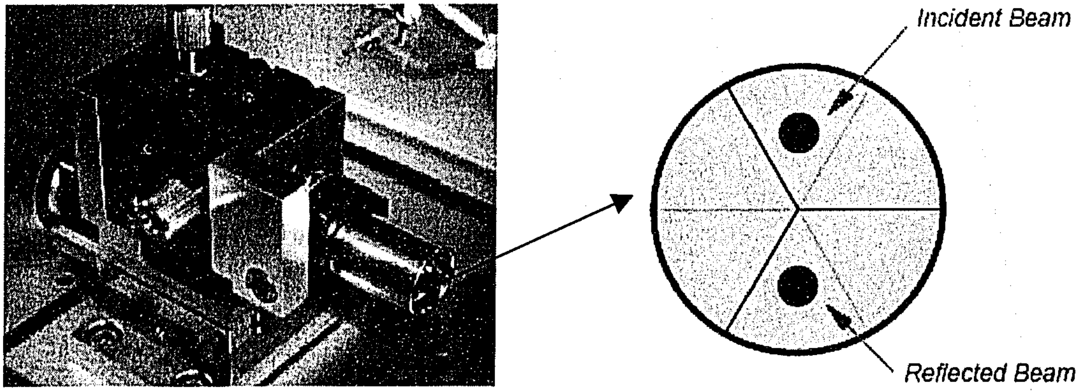

Fig. 4-7: Picture of the retroreflector and a schematic of the sub-apertures showing an incident beam hitting the center of the upper sub-aperture and reflecting off the lower sub-aperture.

4.3.4 Retroreflector

Edmund Industrial Optics 12.7 mm hollow retroreflectors were used in the two arms of the interferometer. These retroreflectors are constructed of three first surface mirrors assembled into a corner cube. This produces a hollow corner cube that is totally insensitive to position and movement. The result is that incident and reflected light will be parallel regardless of the angle of incidence. Fig. 4-7 shows a picture of the retroreflector and detailed view of the sub-aperture formed by the three mirrors. A beam that strikes the exact center of the upper sub-aperture will be reflected back from the center of the lower sub-aperture directly below the incident beam. The retroreflectors are mounted on translation stages. One is mounted on a one-axis stage in order to provide the required variable delay. The other is mounted on an XY stage to allow for ease of alignment.

4.3.5 Lens

The two-photon absorption current and second harmonic signal scales with intensity and is therefore greatly increased by focusing the light onto the detector or nonlinear crystal. An aspheric lens was used for this purpose. The lens focused the beam from the beamsplitter down to an approximate spot size of 36 μm on the detector/crystal

4.3.6 Scanning mechanism

A Newport/Klinger "Motionmaster" motorized micrometer actuator was incorporated with a translation stage to provide the required scanning. Fig. 4-8 shows the schematic of the actuator assembly installed in a translation stage along with a picture of the actuator. The actuator is controlled using Motionmaster drivers and Labview. When moving the arm a distance Δx, the beam has to cover a distance that is $2\Delta x$ longer or shorter than before. The distance is related to the change in delay Δt by $\Delta t = 2\Delta x/c$, where c is the speed of light.

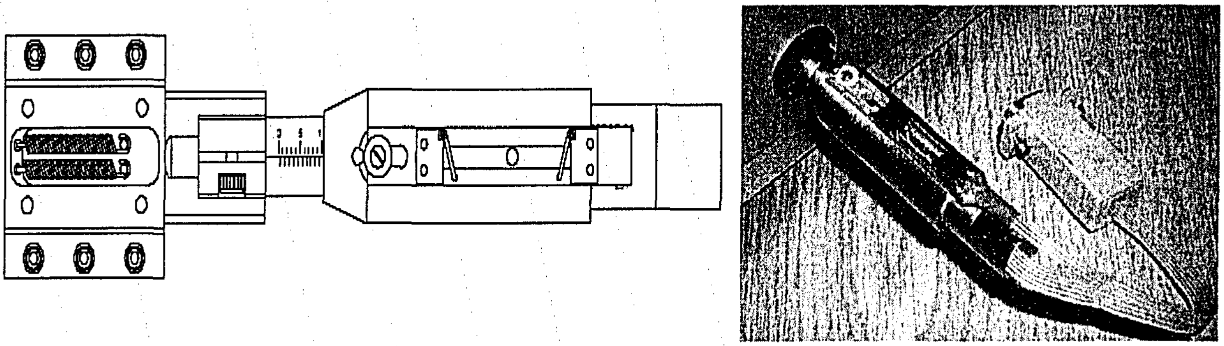

Fig. 4-8: Motionmaster motorized actuator assembly installed in a translation stage and the picture of the actuator connected to the autocorrelator.

4.3.7 Additional Components

The Silicon APD used required a very large bias voltage (150 V) and therefore an EMCO high voltage power supply capable of providing 0 to 200 V was used.

For ease of alignment the retroreflector on the fixed arm of the interferometer was mounted on a Newport compact XY precision translator with 1 μm resolution, as shown in Fig. 4-7. A Newport differential micrometer was connected to this translation stage to allow for fine adjustment in the Z direction.

Linear detectors (Judson Technologies Germanium (Ge) detectors) were used for the initial alignment of the autocorrelator. This allowed for alignment using a 1550 nm CW laser, which was convenient as all the optics were coated for 1550 nm. Finally, Thorlabs ultrastable kinematic ½" optics mounts were used to affix each of the optic devices.

4.4 Autocorrelation testing and verification

This section examines some of the experimental results from the autocorrelator and compares them to theory. Several lasers were used to assess the operation of the autocorrelator. A narrow linewidth CW laser was used mainly for alignment purposes. Subsequently a passively modelocked fiber laser, which was believed to be working in the noise-like regime (refer to Chapter 5 for details), and an actively modelocked fiber laser, also discussed in Chapter 5, were used to test the operation of the autocorrelator.

4.4.1 Autocorrelator Alignment

After assembly and careful alignment of the autocorrelator (refer to [54] for further alignment details), the autocorrelator was tested. The first step was to ensure that the beams were collinear. Using a narrow linewidth CW 1530 nm laser and a Ge (linear) detector in place of the Si (nonlinear) detector (depicted in Fig. 4-5), the delay arm was slowly scanned and the output photocurrent was monitored on a Newport model 1830-power meter (Fig. 4-9). Complete interference was observed with an extinction ratio of approximately 100. This confirmed that the beams from the two arms of the interferometer were indeed collinear as they hit the detector.

Next the 1530 nm CW laser was replaced with a pulsed laser. While the output was monitored on an oscilloscope (Fig. 4-9), the delay arm was scanned slowly (166 fs/s) over the entire 30 mm range of the stage. This allowed for the delay to be calibrated, such that the pulses from each arm overlap in time at the detector. Fig. 4-10 shows the output from the detector as seen on the oscilloscope, which is essentially the function $g_1(\tau)$ (see equation (4.2)). The width of the autocorrelation function $g_1(\tau)$ obtained from this scan is related to the coherence length of the laser pulse. This is not a unique measurement of the duration of the pulse but rather it serves as a first order estimate.

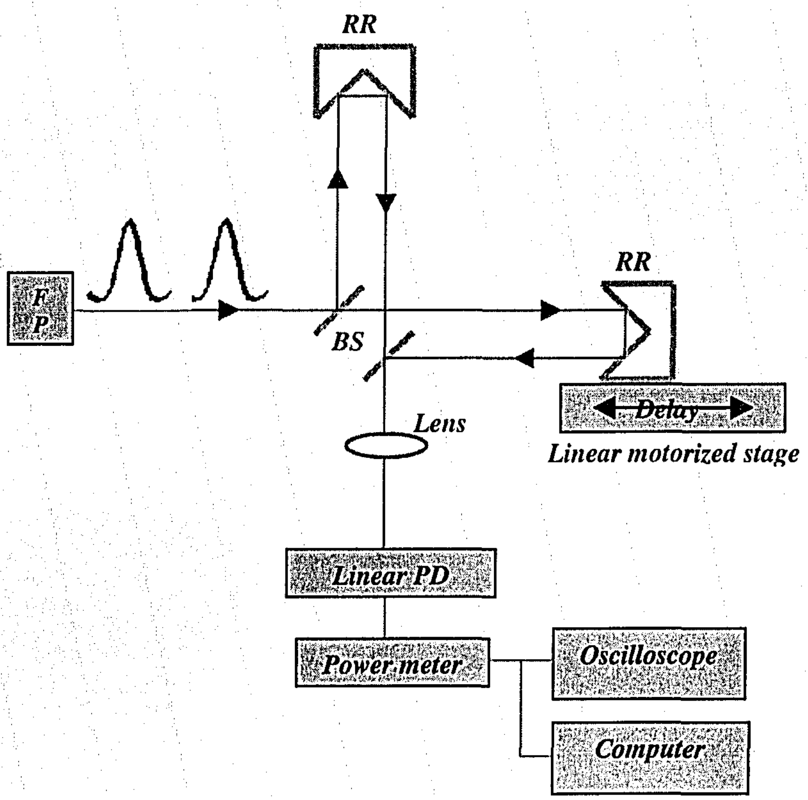

Fig. 4-9: Schematic of the autocorrelator setup. FP-fiber port, RR- retro-reflectors, BS-beamsplitter, PD-photodetector.

Fig. 4-10 (a) resembles a typical first order scan with the exception of the "wings" on the pulse. This is because the input beam was from a stretched pulse laser whose output is typically a pulse with "wings" [57]. Fig. 4-10 (b) shows the fringe pattern of the pulse. From this, the fringe spacing is measured to be approximately 5 fs, which is comparable to the calculated value of 5.16 fs. The fringe spacing *d* is calculated given the wavelength λ and the speed of light *c*, that is, $d = \lambda/c$.

The next step was to perform a second order scan, by replacing the Ge detector with a Si APD or a nonlinear crystal and filter combination. The Si APD was characterized in order to determine its suitability for use as two-photon absorber. The next section describes the results from the characterization experiment.

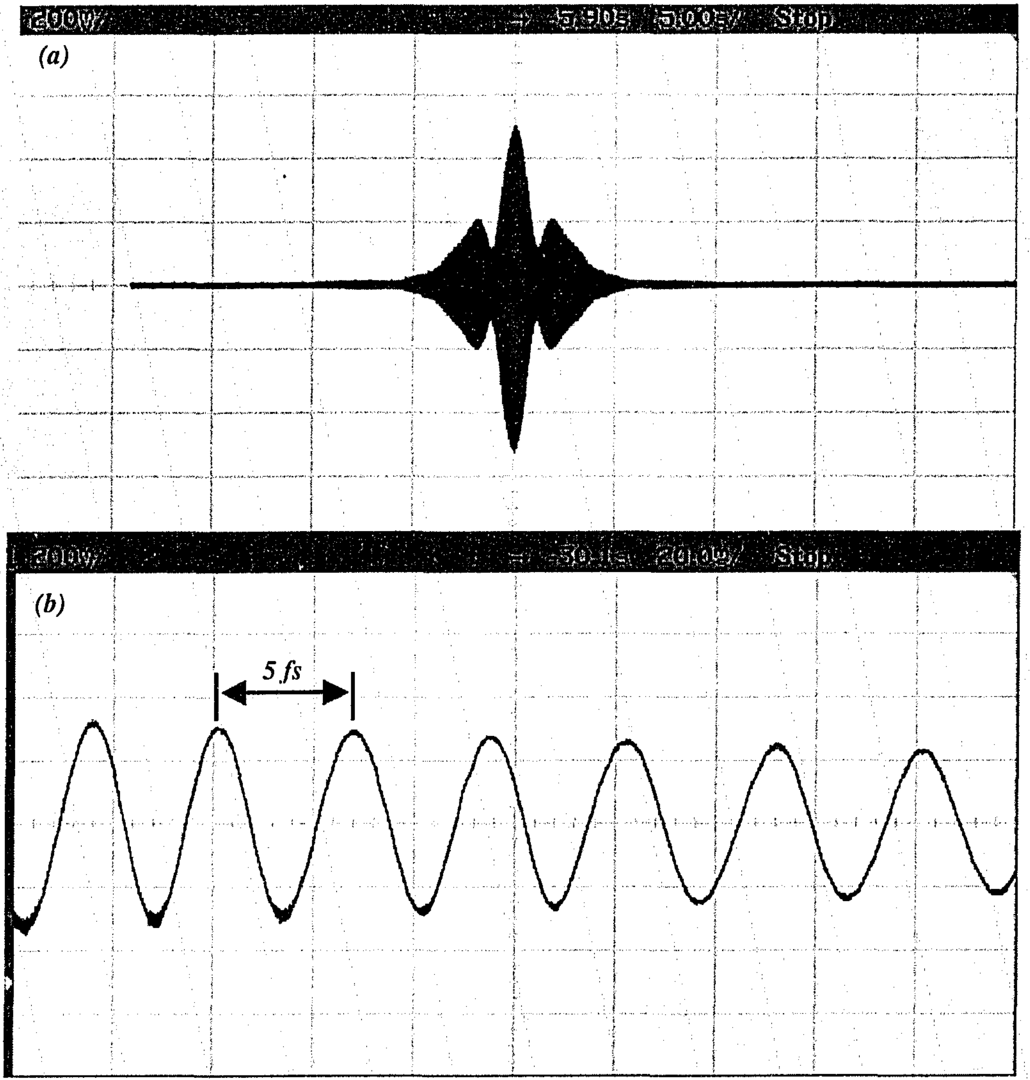

Fig. 4-10: (a) First order autocorrelation trace taken with a Germanium detector, (b) Interference fringe.

4.4.2 Autocorrelation using a TPA detector

A Si APD was tested by focusing the laser output onto the detector and measuring the response as a function of input power. An aspheric lens was used to focus the beam from the laser down to a spot size of 36 μm onto the detector (Fig. 4-11). This spot size was chosen because the beam incident on the detector in the autocorrelator is also 36 μm.

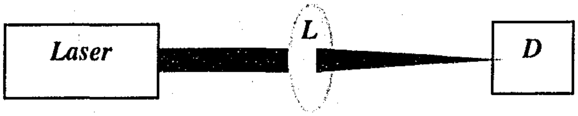

Fig. 4-11: Experiment configuration for charactering detectors. L-Lens, D-Detector

The squares in Fig. 4-12 represent the output photocurrent (I) of the Si APD measured as a function of the CW optical power (P), when the multiplication factor of the APD is set to 100. The solid curve is a theoretical fit, which can be expressed as *I[nA] = 3.17 + 1.94 P[mW] + 0.0021* P^2 *[mW^2]*. The first term originated from the constant background light. The second and third terms are induced by linear and two-photon absorption (TPA), respectively. Similarly the diamonds represent the output photocurrent measured as a function of the average power of the pulsed laser, when the multiplication factor of the APD is set to 100. The theoretical fit can be expressed as *I[nA] = 4.33 + 4.30 P[mW] + 0.211* P^2 *[mW^2]*. Note that the linear absorption current is larger than the TPA current when P is less than 20 mW. This effect is undesirable and must be eliminated.

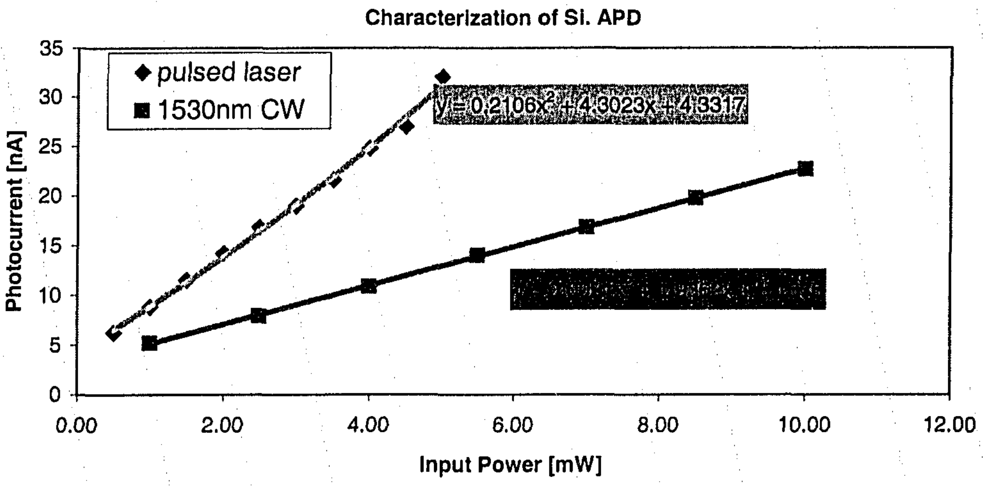

Fig. 4-12: TPA characteristics of Hamamatsu Si APD for 1530nm CW and 1550nm pulsed laser

The Hamamatsu Si APD appeared to be a suitable choice, although the TPA response was still low relative to the linear response for the range of input powers investigated. The small TPA response for the input powers investigated could be due to the fact that TPA depends upon the peak power, and degrades with higher repetition rates for a given average power [56]. The Hamamatsu detector was chosen as the two-photon absorber in the autocorrelator based on the fact that the TPA current exceeds the linear absorption current for average powers greater than approximately 20 mW. The intended use of this detector was to characterize a pulsed laser whose output peak power was anticipated to be much greater than 20 mW, thus linear absorption was not expected to be a problem. Fig. 4-13 shows the output from an autocorrelator scan (166 fs/s) using this detector and the stretched pulse laser discussed in Chapter 3. The results closely resembled the first order scan from Fig. 4-10 using the Ge detector. Apparently linear absorption was still dominant and must be eliminated from the autocorrelation trace in order to obtain a second-order autocorrelation.

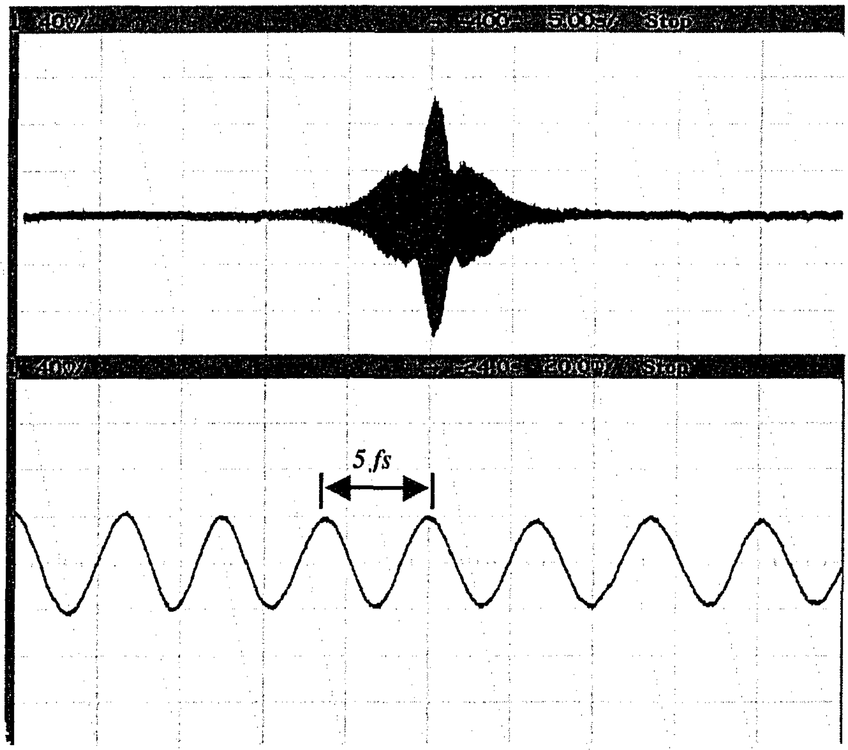

Fig. 4-13: (a) Autocorrelation traces using a Si. APD and stretched pulse laser, (b) Interference fringe

Based on these results, two-photon absorption in a photodiode was abandoned as the detection scheme and the nonlinear crystal was used instead.

4.4.3 Autocorrelation using a nonlinear crystal

The Si APD was replaced with a 5 mm BBO crystal, a bandpass filter that removes the fundamental, and a Si detector that detected the second harmonic signal (Fig. 4-14). The efficiency of the crystal was tested using a high power CW laser and it was found to be approximately two times less than the calculated value. This was attributed to possible misalignment of the crystal and the fact that the confocal focusing parameter assumed in the calculations could not be met exactly. Refer to Appendix A for further details.

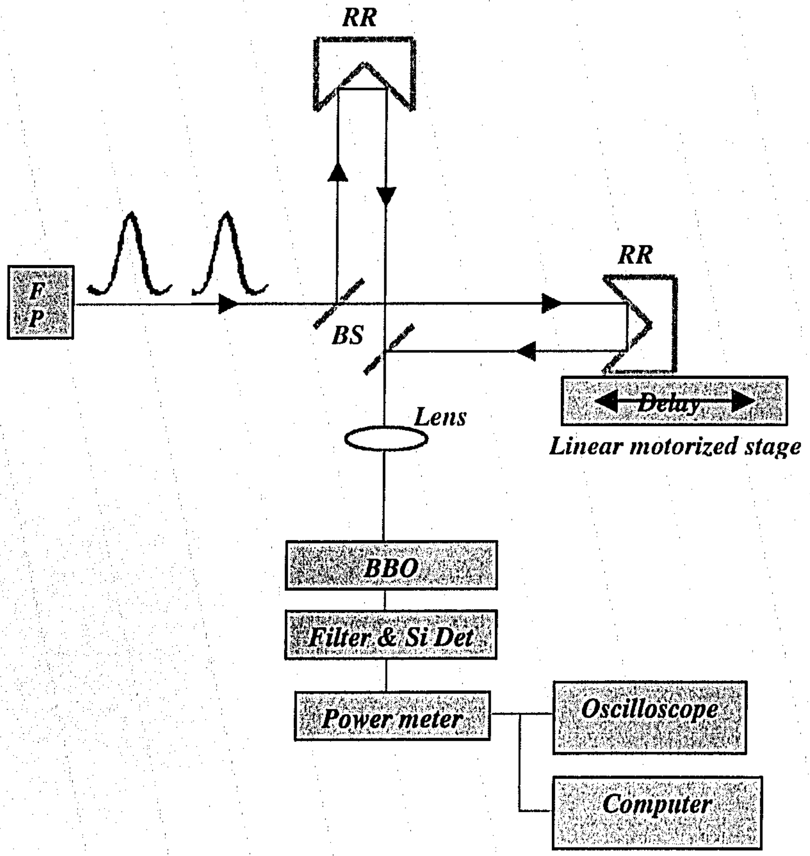

Fig. 4-14: Schematic of the autocorrelator setup. FP-fiber port, RR- retro-reflectors, BS-beamsplitter, BBO – second harmonic crystal.

The output from an autocorrelator scan (166 fs/s) using the configuration shown in Fig. 4-14 and the actively modelocked fiber laser, discussed in Chapter 5, is shown in

Fig. 4-15. Assuming a Gaussian profile, the pulse width at FWHM was estimated to be 10.6 ps ($\tau_G/1.414$). Fig. 4-16 shows the same laser output measured on an optical sampling oscilloscope; the pulse width was measured to be approximately 10.8 ps, in good agreement with the results from the autocorrelator.

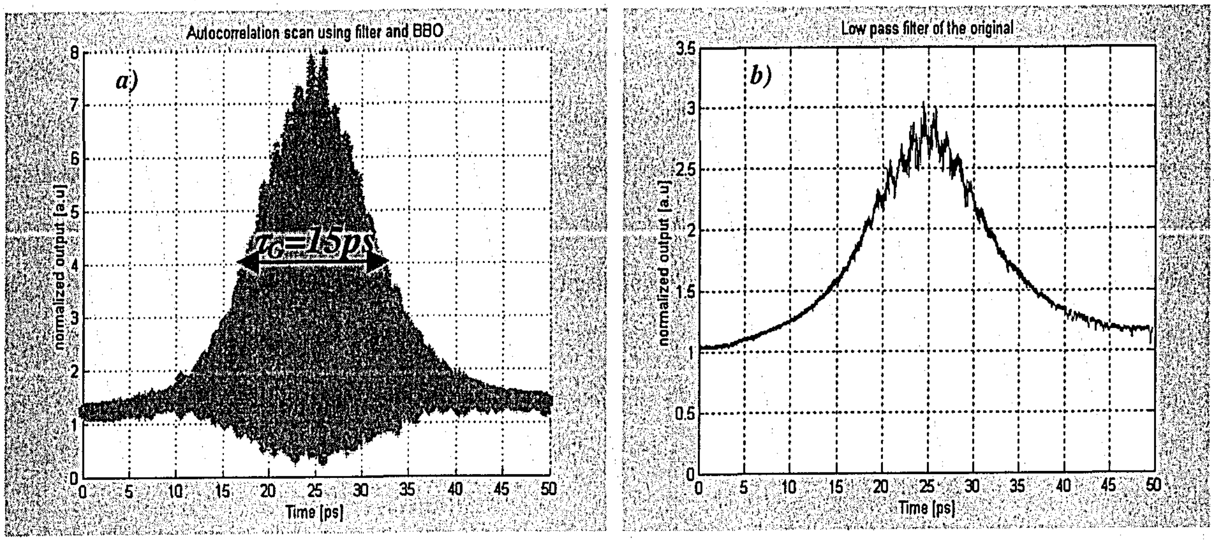

Fig. 4-15: (a) Autocorrelation scan using the second harmonic crystal, (b) Autocorrelation after passing through a low pass filter, which is equivalent to the intensity autocorrelation.

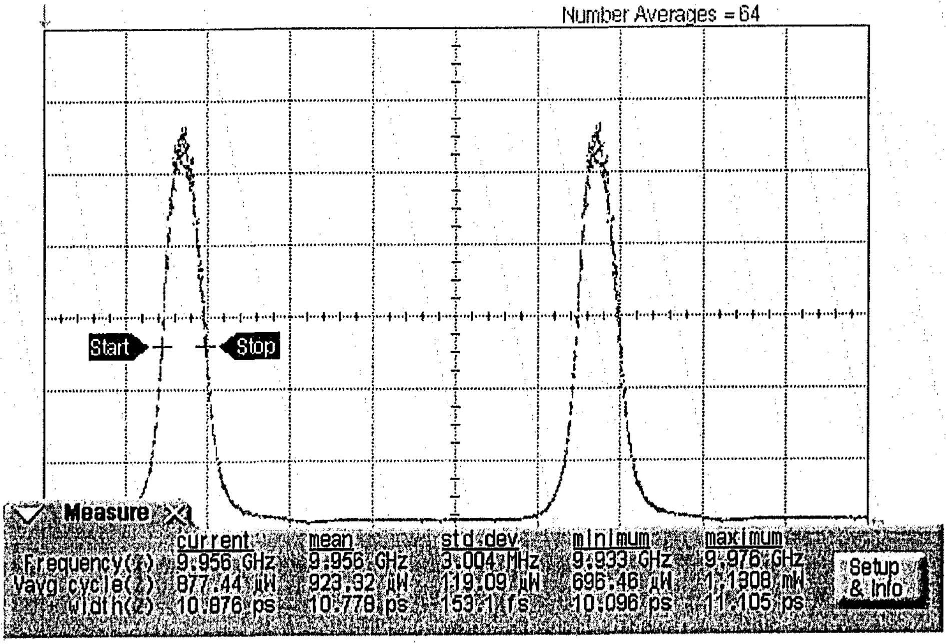

	current	mean	std dev	minimum	maximum
Frequency(2)	9.956 GHz	9.956 GHz	3.004 MHz	9.933 GHz	9.976 GHz
Vavg cycle(2)	877.44 μW	923.32 μW	119.09 μW	696.46 μW	1.1308 mW
+ width(2)	10.876 ps	10.778 ps	153.1 fs	10.096 ps	11.105 ps

Fig. 4-16: Laser output measured using the optical sampling oscilloscope. The pulse width was estimated to be approximately 10.8 ps.

Note that the peak to background ratio of the autocorrelation shown in Fig. 4-15(a) is not quite 8:1, as theory suggests. This is due to the fact that there is a slight power imbalance between the two arms of the interferometer. This imbalance arises in the beamsplitter, which does not split the power perfectly. The power imbalance was measure to be approximately 5%. A simulation was performed and it was found that for an imbalance of 5% the peak to background ratio is reduced. Fig. 4-17 shows the results from this simulation.

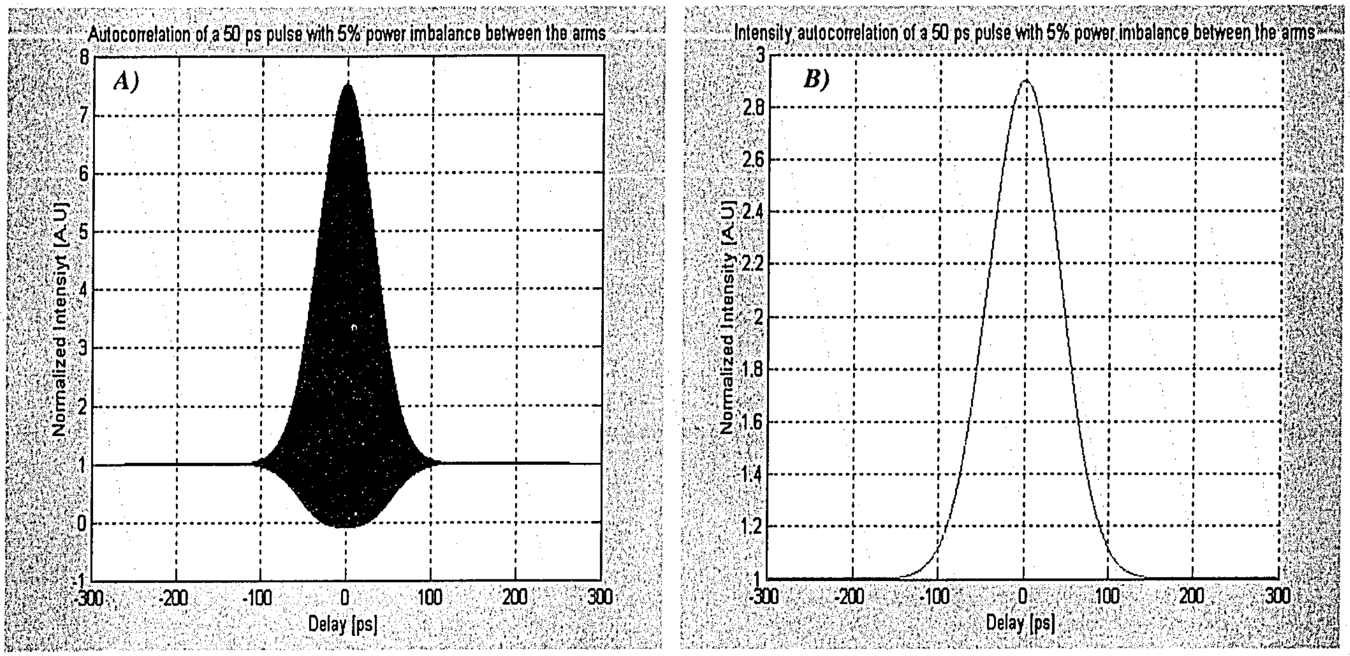

Fig. 4-17: Simulated autocorrelation scans for 5% power imbalance between the arms of the interferometer. A) Interferometric autocorrelation and B) Intensity autocorrelation.

Note that the level at which the interference pattern starts relative to the peak is exactly at 1 for the simulated autocorrelation (Fig. 4-17), whereas in the experimental scan, the interference starts at approximately 1.5 relative to the peak (Fig. 4-15). The level at which the interference pattern begins is an indication of the chirp or phase modulation of the pulse [64]. The interferometric autocorrelation of a linearly chirped Gaussian pulse ($E(t) = \exp[-(1+ia)(t/\tau_G)^2]$) was simulated in Matlab. Fig. 4-18 shows the result from this simulation for chirp parameters of 5 and 3. Comparison of Fig. 4-15 and 4-20 indicates a chirp parameter of approximately $a \leq 3$ for the experimental pulse.

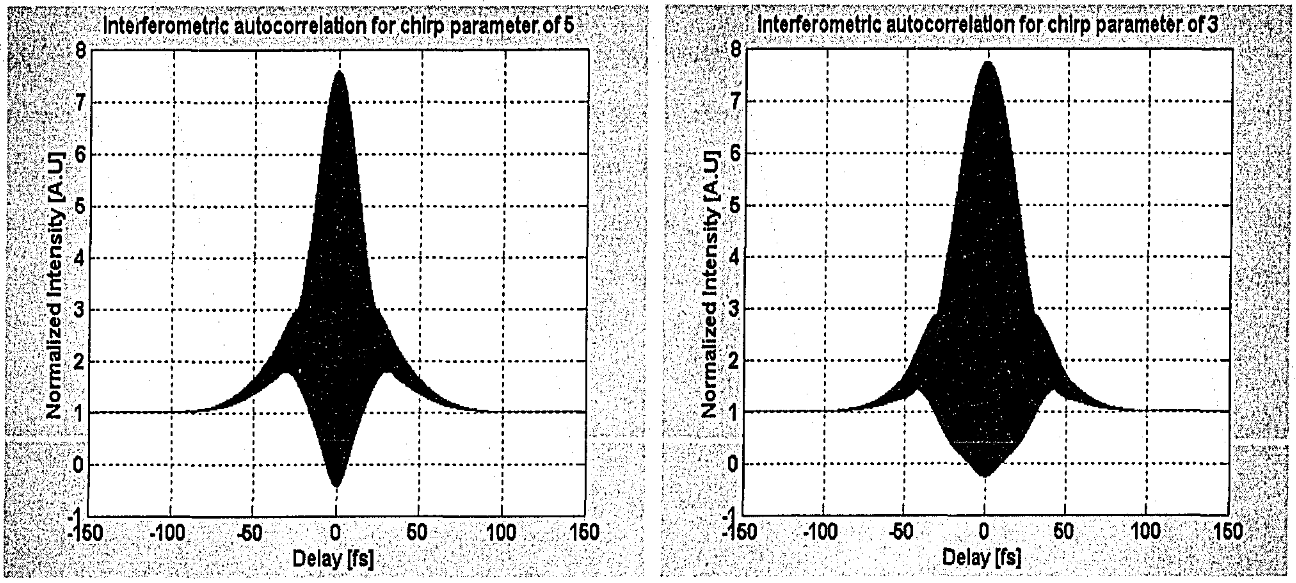

Fig. 4-18: Simulated autocorrelation scan for a Gaussian chirped pulse.

Another way to test the pulse for chirp is by filtering the autocorrelation signal after the detector. This can be done in hardware or equivalently by using digital filters. The interferometric output taken directly at the detector in Fig. 4-14 can be written as (refer to Appendix A for details):

$$S(\tau) = 1 + G_1(\tau)\cos(\omega_0\tau) + 2G_2(\tau) + 4F_1(\tau)\cos(\omega_0\tau) + F_2(\tau)\cos(2\omega_0\tau) \qquad (4.4)$$

where $G_1(\tau)$ is the response due to linear absorption (negligible), $G_2(\tau)$ is the intensity autocorrelation and $F_1(\tau)$ and $F_2(\tau)$ are autocorrelation functions which are defined in Appendix A. If the output signal from the detector is filtered by a lowpass filter, then the intensity autocorrelation $G_2(\tau)$ can be obtained. Conversely if the output is filtered by a bandpass filter whose center frequency is set at $2\omega_0$ and then envelope detected, this produces the autocorrelation function $|F_2(\tau)|$. When the pulse is chirp free, $G_2(\tau) = |F_2(\tau)|$. However when the pulse is chirped, the FWHM of $|F_2(\tau)|$ is smaller than $G_2(\tau)$ [62]. Therefore the chirp of a pulse can be estimated by comparing $G_2(\tau)$ and $|F_2(\tau)|$. Fig. 4-19a shows the interferometric autocorrelation trace obtained at the output of the detector, as represented by (4.4). Fig. 4-19b shows $G_2(\tau)$ and $|F_2(\tau)|$ which are obtained by filtering the interferometric autocorrelation signal. Assuming a Gaussian pulse shape, the pulse width is approximated to be 12.4 ps from the intensity autocorrelation. Note that the pulse is chirped, as the FWHM of G_2 is greater than $|F_2|$.

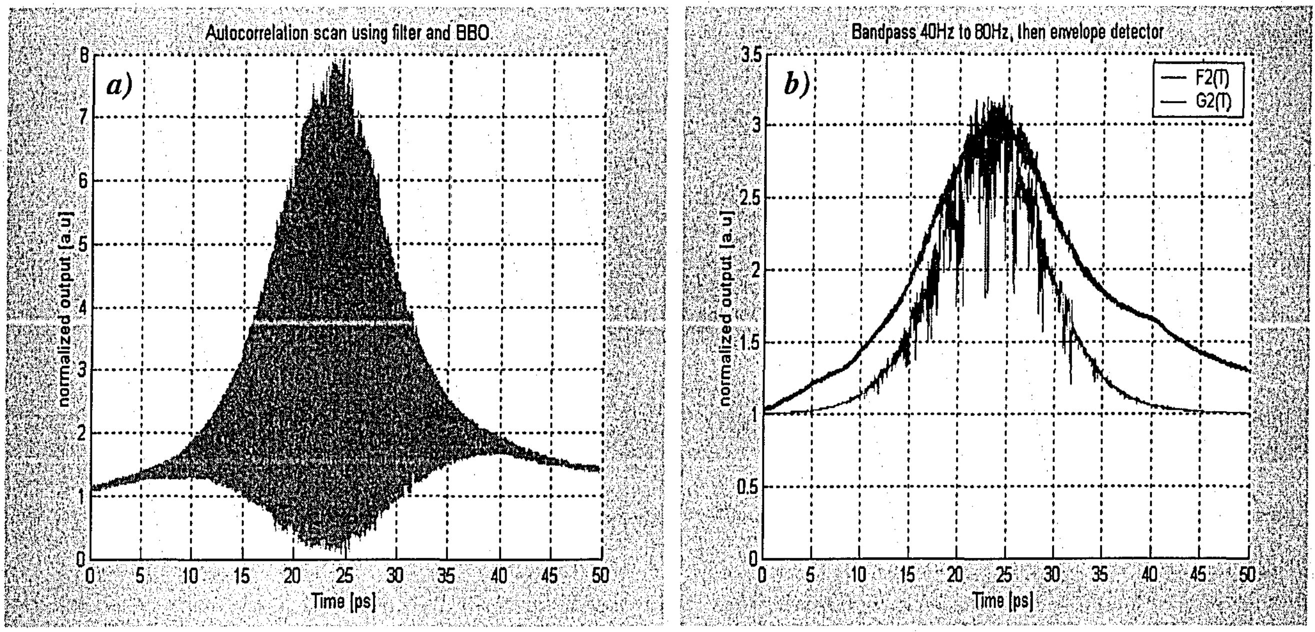

Fig. 4-19: (a) Interferometric autocorrelation and (b) Filtered autocorrelation (blue – lowpass filter and red – bandpass and envelope detected).

Hence the interferometric autocorrelation has proven to be an adequate tool for the characterization of ultrashort pulses. It provides information regarding both the pulse width and a qualitative estimate of the chirp.

4.5 Autocorrelation Summary

An interferometric autocorrelator was implemented and tested. A Si APD was tested to determine its suitability for use as two-photon detector. The Si APD was found to be unsuitable as the linear absorption was too high. A BBO nonlinear crystal and a bandpass filter combination was also tested and found to be the best choice.

The autocorrelator was used to measure pulses from an actively modelocked fiber laser (see Chapter 5). These pulses were long enough that a sampling oscilloscope could be used for independent experimental verification. The autocorrelator produces results that were in good agreement with the results measured by the sampling oscilloscope and also with simulation results. Chirp was also investigated and it was found that the autocorrelator could be used in conjunction with digital filters to give a qualitative estimate of the chirp.

5 *Experimental Results*

5.1 Stretched pulse NPR Laser

Nonlinear polarization rotation is dependent on the polarization state of the input beam relative to the polarization axes of the fiber. The importance of this is discussed in Section 5.1.4. In order to achieve stable modelocking and short pulses, the input beam into the fiber must be elliptically polarized and aligned in such a way that the angle between the major axis of the ellipse and the fast axis of the fiber is small [74],[80]. Hence, in an attempt to achieve modelocking, the first step was to align the input beam to one of the fiber axes.

5.1.1 Obtaining pulsed operation

A simplified version of the laser schematic is shown in Fig. 5-1. To align the input beam to the fiber axis, the λ/4 plate is removed from PC1. The partial schematic shows the main types of fiber and polarization optics that made up the cavity. Typically 2 m of EDF (NOI, Er-123, D ~ 0.0102 ps^2/m), 1.25 m of SMF28 and approximately 0.5 m of Flexcor1060 were used in the cavity. Note that, for simplicity, the couplers are not shown.

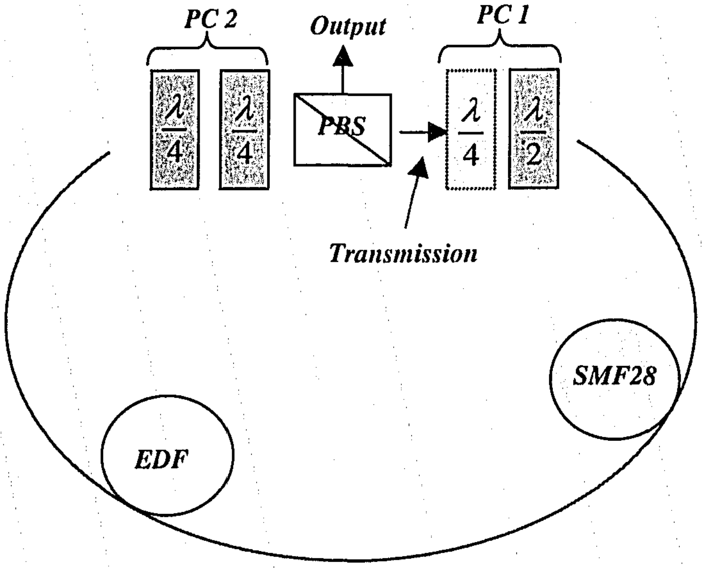

Fig. 5-1: Partial Schematic of the stretched pulse NPR laser. PBS – Polarizing beamsplitter, PC 1&2 – Polarization Controllers, EDF – Erbium doped fiber, and SMF28 – Regular single mode fiber.

The section of SMF28 fiber was assumed to be isotropic since the length does not exceed 2 m and standard SMF28 has low birefringence (refer to Section 2.5). Hence, if linearly polarized light is launched it should emerge at the other end with the same polarization and orientation since the effect of birefringence vanishes. Therefore it was assumed that all of the rotation takes place in the EDF section. To begin the alignment process, the pump power was slowly adjusted until the laser was running in CW mode. The linearly polarized beam from the PBS was then rotated by the $\lambda/2$ plate and launched down the fiber as shown in Fig. 5-2. The $\lambda/2$ plate was adjusted in 2^{o} increments in conjunction with PC2 while the outputs (rejection port of PBS and 5% coupler) were monitored. The waveplates were adjusted in this fashion until a maximum output and minimum transmission was obtained. At this point CW lasing essentially stopped. Recall that the saturable absorber action introduces a loss that is large for low intensities but significantly smaller for high intensities. Hence for the low power CW mode, the waveplates were adjusted so that the loss is maximized inside the cavity. This alignment was verified by rotating the $\lambda/2$ plate by 45^{o} from it previous position and monitoring the outputs. If the beam was indeed aligned to one of the fiber axes, then rotating the input $\lambda/2$ waveplate by 45^{o} was expected to produce a 90^{o} polarization state change at the input to the PBS, thus giving minimal output from the PBS and maximum internal transmission. In practice, rotation by 45^{o} resulted in an output power that was approximately zero but not completely extinguished. This was likely due to the fact that the SMF28 fiber is not actually isotropic, but slightly birefringent. Note that any bends in the fiber would add to the birefringence.

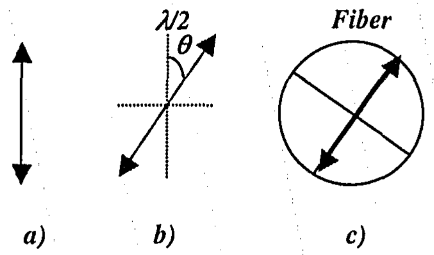

Fig. 5-2: Polarization state launched into the fiber. a) Linearly polarized output from PBS, b) Rotated linearly polarized output using the $\lambda/2$ plate rotated by θ, and c) Rotated linear polarization launched along one axis of the fiber.

Once the input was approximately aligned to one fiber axis, a λ/4 plate was placed between the PBS and the λ/2 plate at the input of the fiber. Note it could not be concluded (from the method described above) if the beam was aligned to the effective fast or slow axis. Rotating the λ/4 plate between 0° and 45° produced an elliptically polarized beam which was launched down the fiber at an angle determined by the setting of the λ/2 plate (see Fig. 5-3). Chang *et al.* [74] showed that along with the alignment to the fiber axis, the ellipticity of the launched light is also vital in producing short stable pulses. The ellipticity is defined as the ratio of the minor to major axis of the ellipse. The ellipticity and the ellipse angle, i.e. the angle between the major axis of the ellipse and the slow axis of the fiber, describe the state of the polarization. They found that stable modelocking could only be obtained for small ellipticity. Hence the λ/4 plate was only rotated in a small range from its zero position.

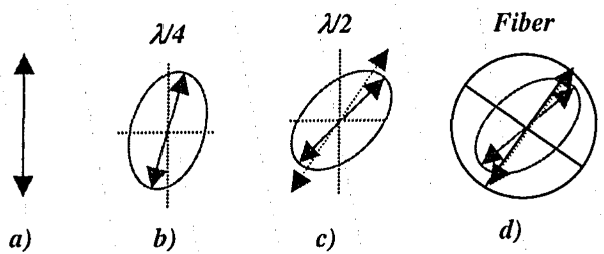

Fig. 5-3: Elliptical polarization state launched into the fiber. a) Linear polarization from PBS, b) Linear polarization converted to elliptical by rotation the λ/4 plate by a small amount, b) λ/2 plate rotates the ellipse and d) Ellipse launched relative to the fiber axis.

With PC 2 set to approximately 75°, λ/2 set to 47°, λ/4 set to 10° (all angles relative to the transmission axis of the PBS) and a pump power of 30 mW, the output spectrum from the rejection port of the laser is shown in Fig. 5-4. As can be seen from the presence of the CW lasing mode the output was not consistent with a stable pulsed mode operation. In order to stabilize the output, PC 2 was adjusted. As the pump power was increased, both the λ/4 and PC 2 plates needed to be adjusted in order to obtain a stable spectrum (i.e. one without any CW lasing mode "spikes"). The procedure for doing this was fairly systematic; the pump power was slowly increased until the spectrum went unstable. At this point, the increase in pump power was stopped and then PC 2 was adjusted until the spectrum was stable again. The pump power was then increased even further until the spectrum became unstable again, at which point PC 2 was adjusted until the spectrum was devoid of CW lasing modes.

Above a certain pump power, adjusting PC 2 was not sufficient to obtain a stable spectrum. At this point the λ/4 plate had to be adjusted in conjunction with PC 2. These adjustments to the waveplates were typically small. There was also a second limit to how much the pump power could be increased, since beyond some power no further adjustment to the waveplates would allow for a spike-free spectrum. This was likely due to high levels of peak pulse power in the cavity as a result of the increase in the gain when the pump power was increased. These high levels of peak power were speculated to result in a greater nonlinear phase shift than was required for modelocking. The laser usually accommodates for this by operating in a multiple pulse mode, as discussed in Chapter 3 and again later in this chapter. The laser could be made to operate in the single pulse regime again by decreasing the pump power until a stable spectrum was obtained.

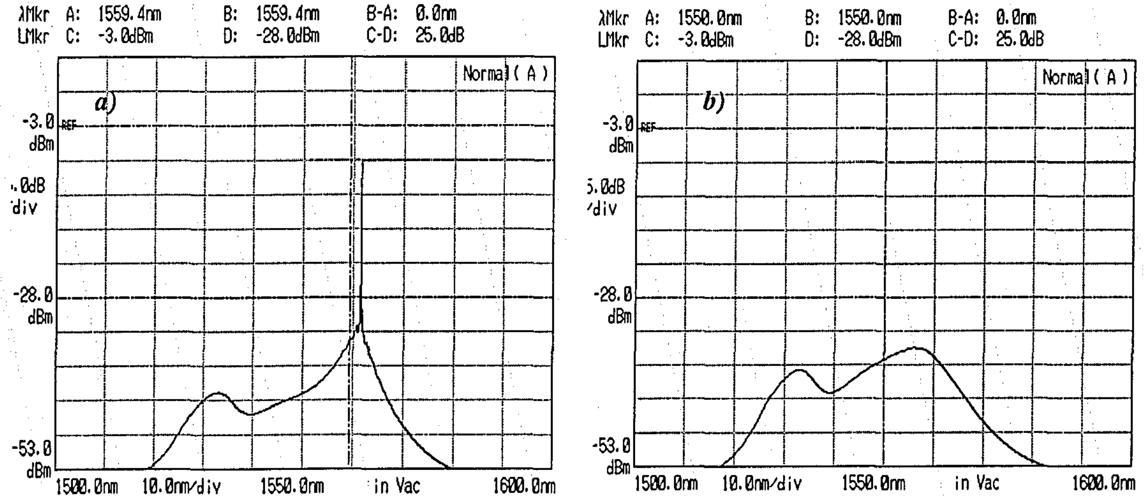

Fig. 5-4 Laser output spectrum with: a) λ/4 plate set to 10°, λ/2 set to 47°, and PC 2 set to 75° and, b) λ/4 plate set to 10°, λ/2 set to 47°, and PC 2 set to 50°. Pump Power = 30 mW.

5.1.2 Empirical optimization of the cavity

An experimental optimization was attempted using the configuration shown in Fig. 5-5. First the effect of varying cavity length was investigated. Two main parameters, stability of the spectrum and average output power, were considered.

The output of the laser was monitored over an extended period of time using a spectrum analyzer and a power meter. The length of the cavity was varied from a length of 4 m to 20 m. NUFERN555 EDF was used for this experiment. It has peak absorption of 8.7 dB/m at 1530 nm and estimated GVD of 0.0127 ps^2/m at 1550 nm. For each cavity length, the amount of EDF and SMF28 fiber used was chosen such that the total dispersion in the cavity was approximately zero. Table 5-1 summarizes the results from this experiment. For short cavity lengths the laser was very difficult to modelock and once modelocking was obtained, the average power was very low. This might be attributable to insufficient gain in the cavity, which was a result of the short lengths of EDF. As the cavity length and thus the amount of EDF was increased, so was the average power and stability.

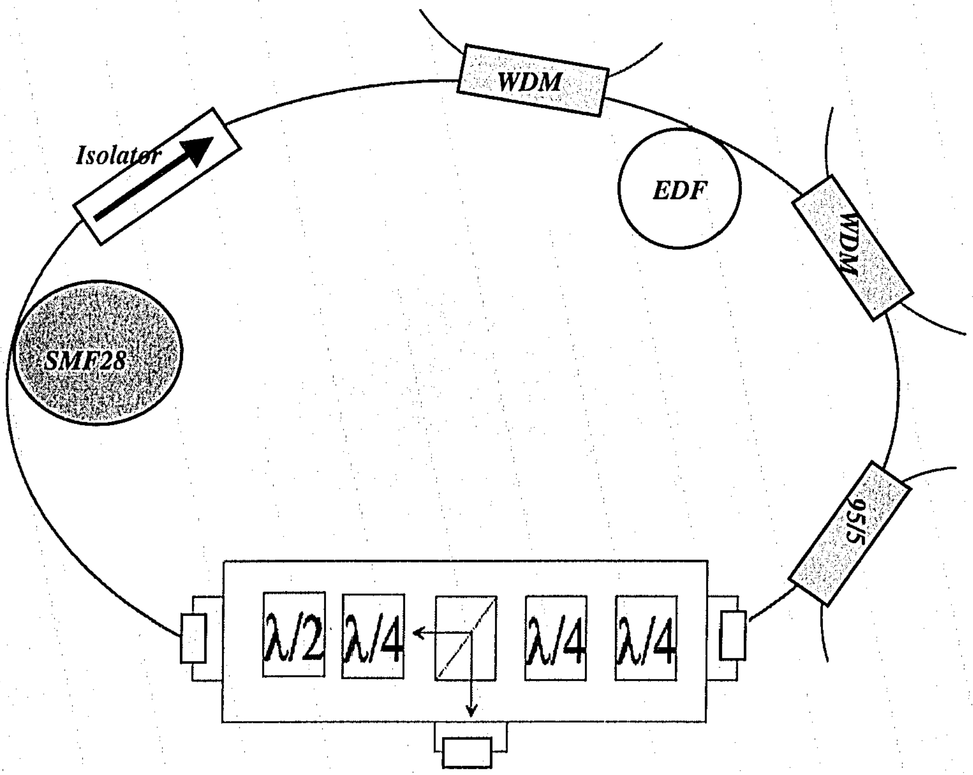

Fig. 5-5: Schematic of the cavity used for testing the stretched pulse laser.

It was observed that for cavity lengths longer than 13 m the laser was stable only for a few minutes. This was most likely due to vibrations or thermal drift, which would change the birefringence of the fiber, thus causing the laser to enter an unstable regime. Fig. 5-6 shows the output spectrum of the laser for a 15 m long cavity when it was initially modelocked and after it has been running for a few minutes. After numerous trials and based on the results in Table 5-1, a cavity length of 9 m was chosen for subsequent experiments. Results using shorter cavities will also be shown for comparison purposes.

Cavity Length	Average Power	Period	Stability of pulsed mode operation
4m (1.5m EDF and 0.5m SMF28 & 2m Flexcor1060)			Not possible to obtain pulsed mode
4.5m (2m EDF and 0.5m SMF28 & 2m Flexcor1060)	75 μW	22.5 ns	Stable
6m (3m EDF and 1m SMF28 & 2m Flexcor1060)	1 mW	30 ns	Stable
8m (4.5m EDF and 1.5m SMF28 & 2m Flexcor1060)	2 mW	40 ns	Stable
9m (5m EDF and 2m SMF28 & 2m Flexcor1060)	3.34 mW	45 ns	Very Stable
15m (10m EDF and 3m SMF28 & 2m Flexcor1060)	3.5 mW	75 ns	Stable for approximately 15 minutes

Table 5-1: Average power and stability data for varying cavity length.

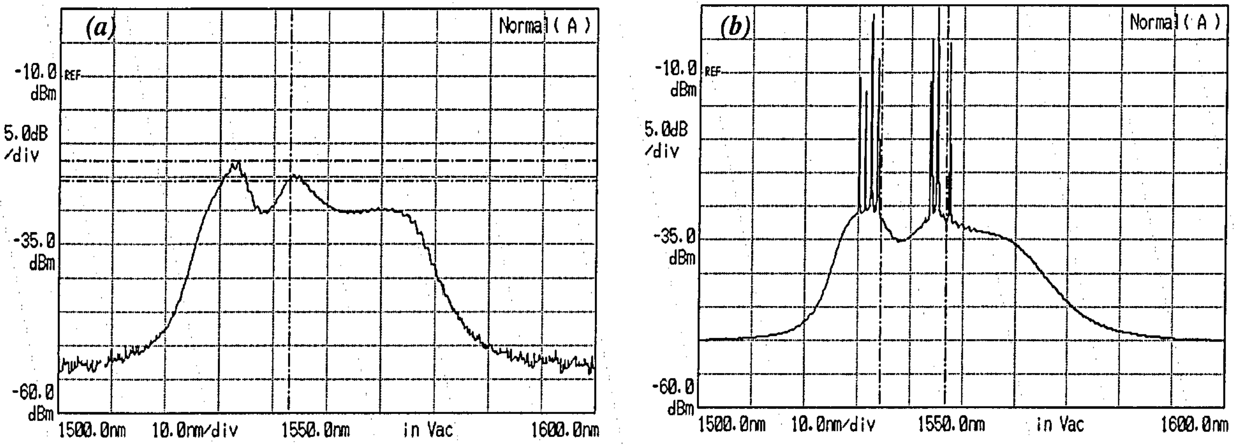

Fig. 5-6: Output spectrum from laser when cavity length = 15m. (a) Immediately after obtaining pulsed operation and (b) after a few minutes of stable pulsed operation.

This experiment was repeated using NOI Er-123 EDF. In this case, a cavity length of approximately 3.75 m, consisting of 2 m of EDF, 1.25 m of SMF28 and 0.5 m of Flexcor1060, was found to produce the best results. For this cavity configuration the laser was extremely stable in time and produced an average output power of approximately 4 mW.

5.1.3 Efficiency

For each of the optimized cavities discussed above, the efficiency of the configuration was tested for both types of EDF. This was done by varying the pump power and monitoring the output in both the CW and pulsed modes of operation. Pulsed operation was obtained by adjusting the polarization controllers. The threshold for lasing was found to be approximately 35 mW of 980nm pump power for the NUFERN555 EDF and 60 mW for the NOI Er-123 EDF. The output at full pump power (220 mW) in both the CW and modelocked case was comparable to other results reported for this type of laser [59]. The output power was approximately 40% of the power within the cavity, determined by tapping a small percentage of the cavity power using a 95/5 fiber coupler, comparable to the theoretical 50% that is suggested for this type of setup [51].

The pump power was set to 220 mW and the polarization controllers were adjusted to achieve stable pulsed operation. The pump power was then slowly lowered and the output power was monitored (Fig. 5-7). The spectrum of the laser for this setting of the polarization controllers is shown in Fig. 5-8. These results are from the configuration using 5 m of NUFERN555 EDF. The results were almost identical for the NOI Er-123, with the exception of slightly higher average output powers.

Self-starting pulsed operation in a single pulse regime was observed for pump powers as low as 35 mW and retained for pump powers as high as 220 mW with an average output power of 3.34 mW as shown in Fig. 5-7. For pump powers higher than 220 mW, the laser entered into the unstable regime as shown in Fig. 5-9, which will be discussed later in this chapter.

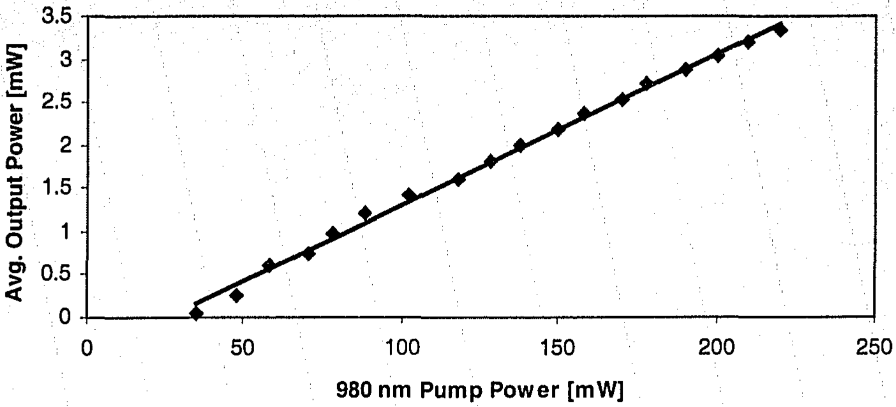

Fig. 5-7: Output power versus pump power when the laser is operating in pulsed mode for a given setting of the polarization controller.

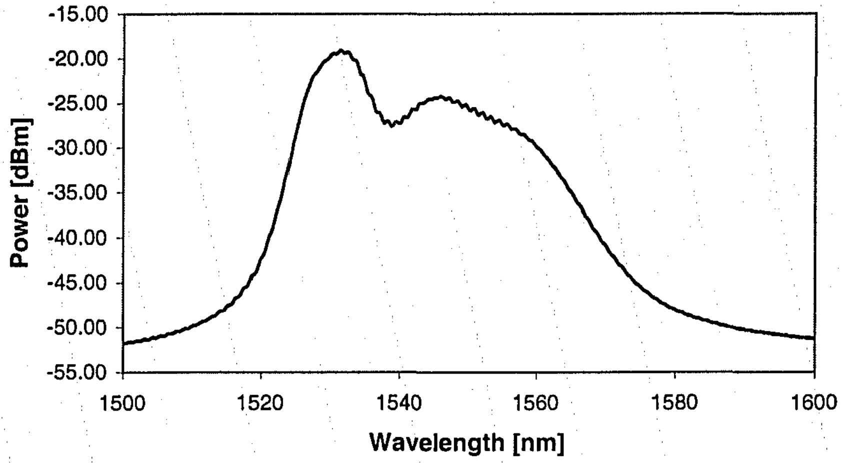

Fig. 5-8: Stable output spectrum for a given setting of the polarization controllers and pump power < 220 mW.

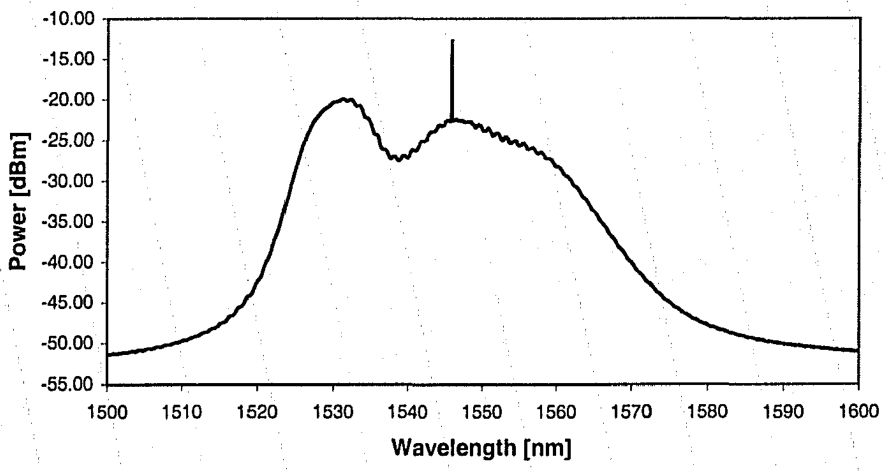

Fig. 5-9: Unstable output spectrum for pump power >220 mW.

With the pump power set to 220 mW, the polarization controllers were adjusted until CW operation was obtained (all waveplates set to zero). The pump power was then slowly lowered and the output power was observed as shown in Fig. 5-10. The frequency domain spectrum when operating in the CW regime is shown in Fig. 5-11.

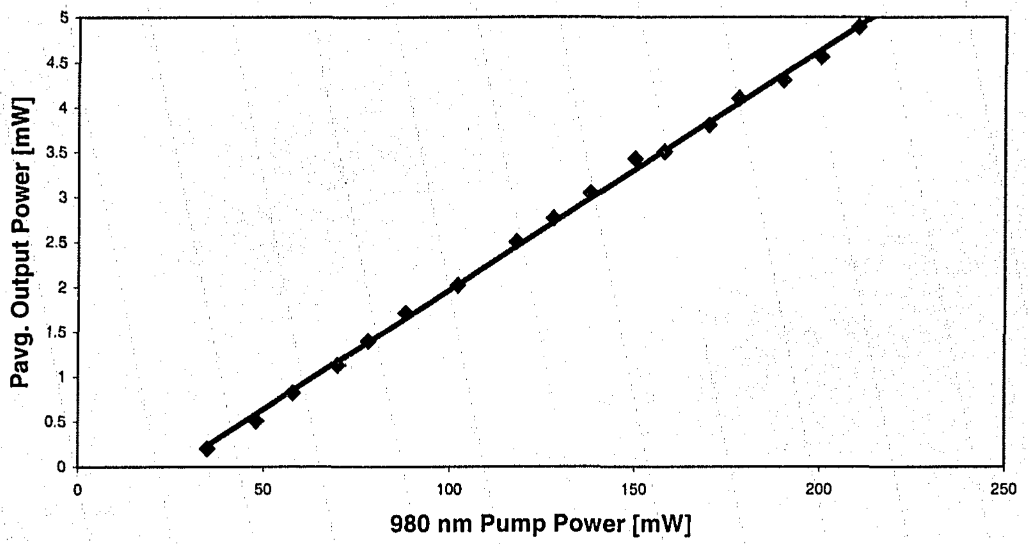

Fig. 5-10: Output power versus pump power when the laser is operating in the CW regime.

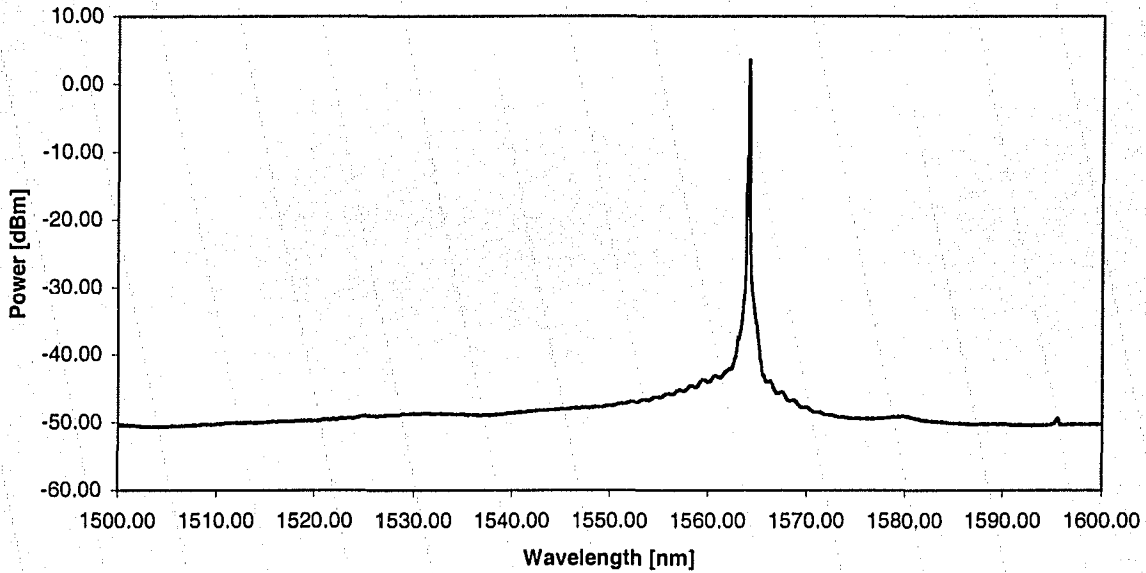

Fig. 5-11: Output spectrum when the laser is operating in the CW regime

5.1.4 Modes of Operation

As discussed in Chapter 3, stretched pulse fiber lasers tend to operate in one of three modes: single short-pulse (per cavity round-trip time), multiple-pulse or the noise-like pulse modes. This section examines the different modes of operation for the stretched pulse laser discussed above.

The pump power was increased beyond threshold and pulsed operation was achieved through careful adjustment of the polarization controllers. The pump power was then further increased until the spectrum became unstable. At this point the laser should be operating in the multiple pulse regime. The results shown in Fig. 5-12 are for a cavity approximately 5 m long, consisting of 3m of NUFERN555 EDF, 1.5 m of SMF28 and 0.5m of Flexcor1060. The total dispersion was approximately 0.0016 ps^2. The time domain output of the laser as seen on the oscilloscope and the spectrum are shown in Fig. 5-12. From the oscilloscope trace it can be seen that there were three pulses per round trip inside the cavity. The pulses were spaced approximately 10 ns apart and they repeat every period. Since the pulses were spaced uniformly in the cavity, this is known as a special regime of operation called passive harmonic modelocked operation. This technique can be used to increase the repetition rate of the laser but it is often difficult to produce stable equal amplitude pulse train unless special stabilization techniques are used [88].

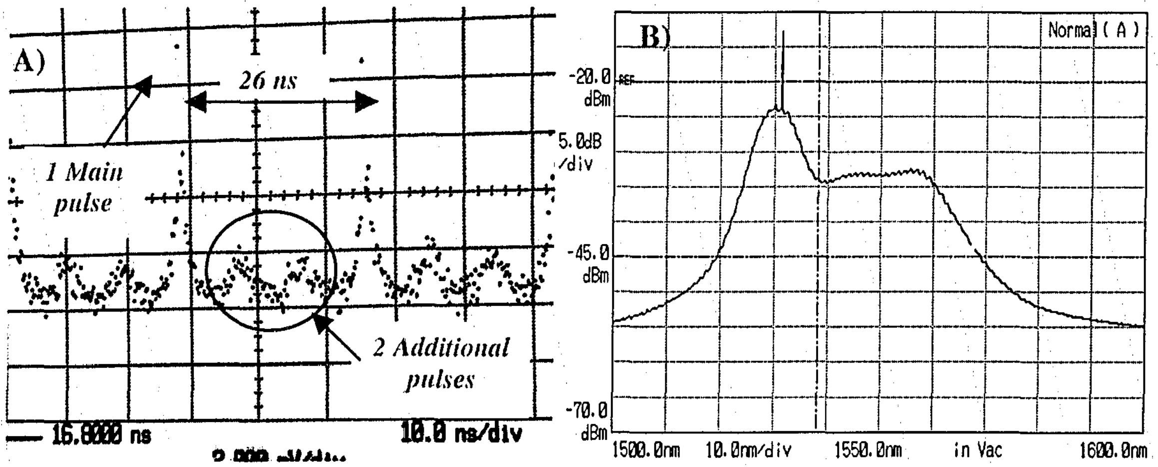

Fig. 5-12: A) Time domain output of the laser operating in the multiple-pulse regime with 3 single-pulses existing in the cavity per round trip. The period of the laser is 26 ns. B) Output spectrum for the laser operating in the multiple-pulse regime. Pump power = 80 mW

The interferometric and intensity autocorrelation trace for this mode of operation is shown in Fig. 5-13. Note that the peak to background ratio is not 8:1 for these traces. This perhaps indicates that the laser was operating in a noise-like multiple-pulse regime. The ratio for the interferometric trace was approximately 4:1 and for the intensity trace approximately 2:1, which is typical for noise-like pulses [75]. Multiple pulses did not show up in the autocorrelation trace, as the delay could only be scanned over a 30 ps range. This was a limitation of the translation stage used to scan the delay. The autocorrelation trace also indicates the instability of this mode of operation. Notice the random nature of the background signal compared to the one in Fig. 5-15 for the single pulse regime. This is an indication of the instability of the output power in this mode of operation.

The threshold for multiple-pulse operation is reportedly higher than that for single-pulse operation [73], hence if the pump power was reduced, the laser should enter the single-pulse regime. The output as seen on the oscilloscope and spectrum analyzer is shown in Fig. 5-14, for the case when the pump power was reduced. Notice that with the reduction in the pump power the additional pulses have been suppressed. Also notice the non-uniformity of the pulse train amplitude. This was attributed to pulse-to-pulse amplitude fluctuations. These fluctuations have been reported [92] to be due to the alignment of the polarizer relative to the birefringence axes of the fiber and the birefringence strength. The autocorrelation trace is shown in Fig. 5-15. Notice that the peak to background ratio for the autocorrelation trace is still not 8:1 indicating that this is not truly a short single-pulse mode.

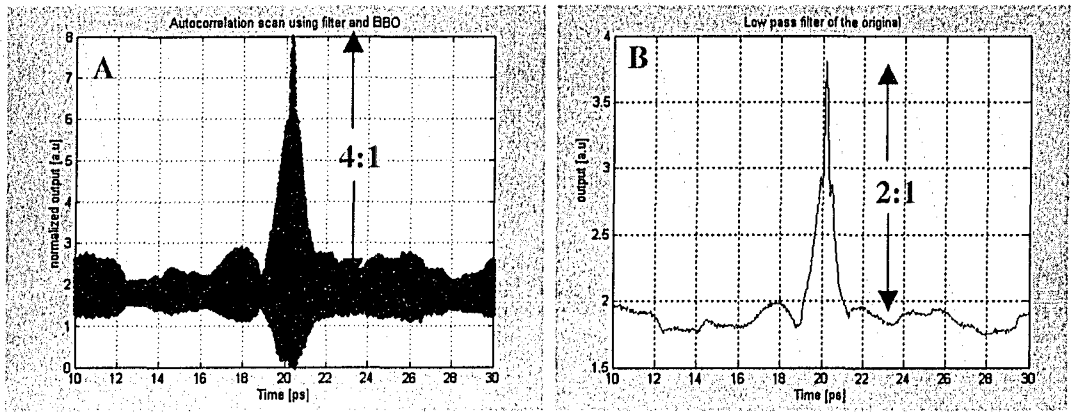

Fig. 5-13: A) Interferometric autocorrelation trace for multiple pulse regime with a peak to background ratio of 4:1 and B) Filtered interferometric autocorrelation (intensity autocorrelation) with a peak to background of 2:1.

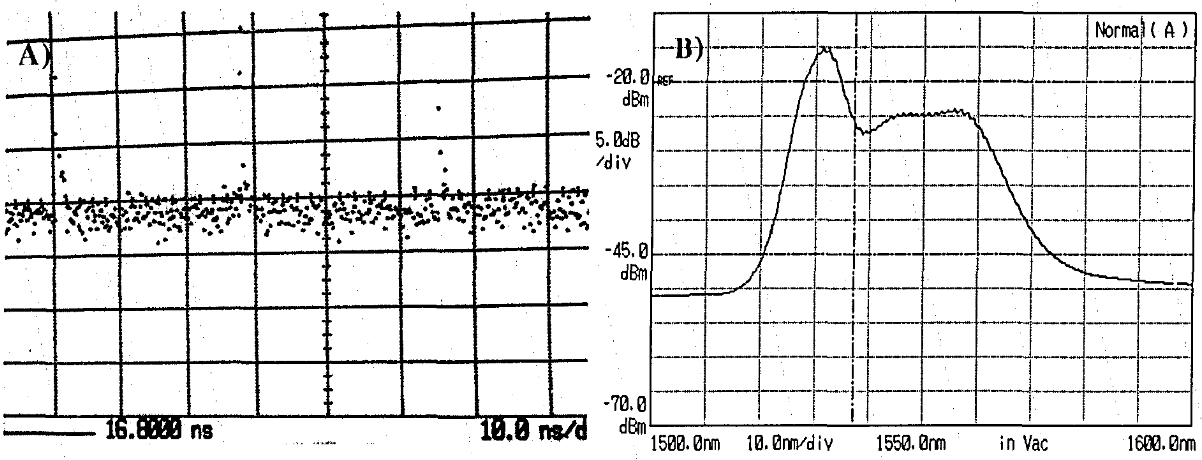

Fig. 5-14: A) Time domain output of the laser operating in the single-pulse regime (single pulse per round trip). The period of the laser is 26 ns. B) Output spectrum for the laser. Pump power = 65 mW.

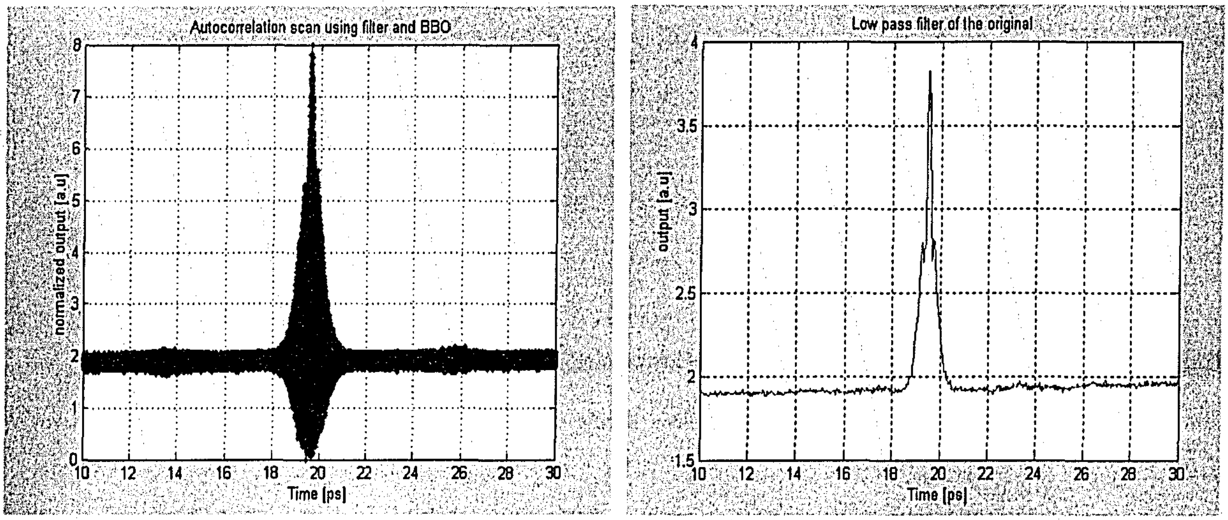

Fig. 5-15: A) Interferometric autocorrelation trace for single pulse regime with a peak to background ratio of 4:1 and B) Filtered interferometric autocorrelation (intensity autocorrelation) with a peak to background of 2:1.

Comparing the intensity autocorrelation traces for the single-pulse and multiple-pulse modes it can be seen that the pulse shapes and widths are almost identical with the exception of the background signal. The normalized intensity autocorrelation trace for the two modes of operation is shown in more detail in Fig. 5-16. The figure shows a main peak of identical width sitting on top of a pedestal for both modes of operation. This perhaps indicates that the laser is actually operating in the bound soliton regime [73] since the pulse did not change with a change in pump power. Another indication is that the pedestal (or side peaks) were half of the main peak, which is indicative of two bound-solitons [73]. Because of the slow detector rise time and the fact that bound solitons are spaced very closely together, this mode of operation cannot be seen on the oscilloscope. Gong *et al.* [73] found that the threshold of bound solitons is the same as the pump power for two single-soliton pulses existing in the cavity and that further increasing the pump power will result in multiple bound-soliton operation. For a pump power of 80 mW as shown in Fig. 5-13, the laser output resembles the output for the bound soliton regime where there was also three single-soliton pulses existing in the cavity per round trip. When the pump power was reduced to 65 mW, the multiple pulses were extinguished but the pump power was still high enough to maintain the bound-soliton state.

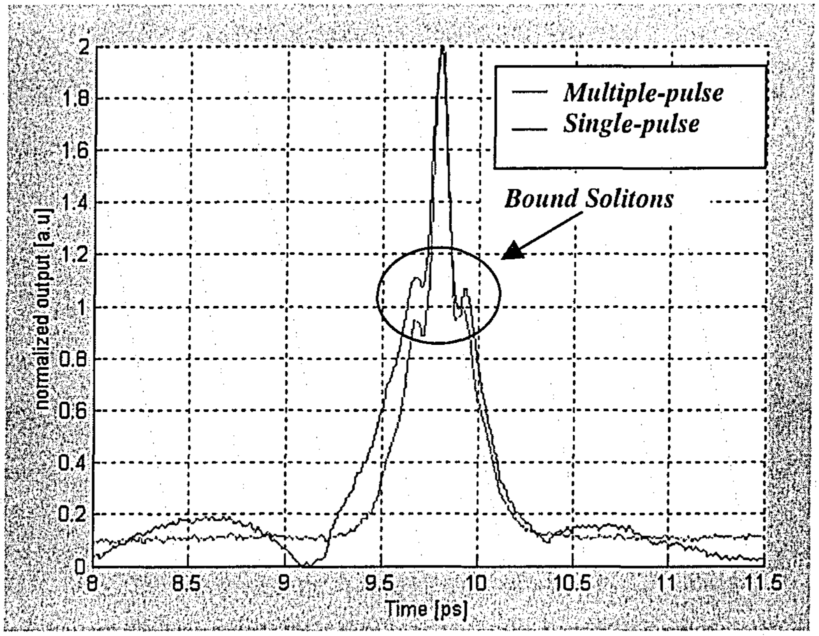

Fig. 5-16: Normalized intensity autocorrelation trace outlining similarity and nature of the pulse shapes for multiple-pulse and single-pulse mode of operation.

In order to produce bound solitons, it has been reported that the birefringence in the laser cavity must be low and the total cavity dispersion must be negative [79]. The dispersion of the laser cavity described above was estimated to be net positive, however this was only an approximation, as the exact dispersion of the EDF was not known. This is because the dispersion of EDF cannot be easily measured and was not provided by the manufacturer. Hence, it was approximated based on the numerical aperture and core diameter using a simple step index waveguide calculation discussed in Appendix A. Therefore, it is possible that the net cavity dispersion was negative. Furthermore, the cavity birefringence was not known accurately.

The bound-soliton state was further tested by adjusting the polarization controllers and varying the pump power. The intensity autocorrelation trace is shown in Fig. 5-17. Notice that the pulse width and separation of the side peaks were unchanged for different pump power, suggesting that the laser might be operating in the bound-soliton regime.

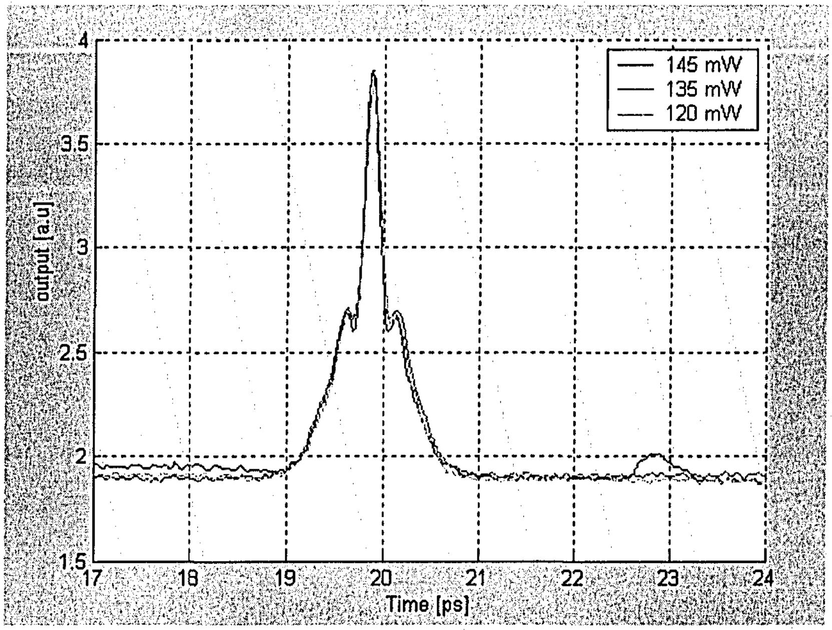

Fig. 5-17: Intensity autocorrelation of two-bound solitons for different power powers. The width of the center peak is approximately 200 fs.

The pump power was further reduced and the polarization controllers adjusted until a single pulse non-bound soliton mode of operation was obtained. The spectrum and time domain information is shown in Fig. 5-18. The corresponding autocorrelation traces are shown in Fig. 5-19. This resembles a typical autocorrelation trace for single-pulse mode of operation for a stretched pulse NPR laser [57]. The side peaks ("wings") on either side of the main peak were only a fraction of the height of the main peak and were not considered to contain a significant amount of power. The width of the main peak is almost identical to the width of the main peak in the bound-soliton case in Fig. 5-17.

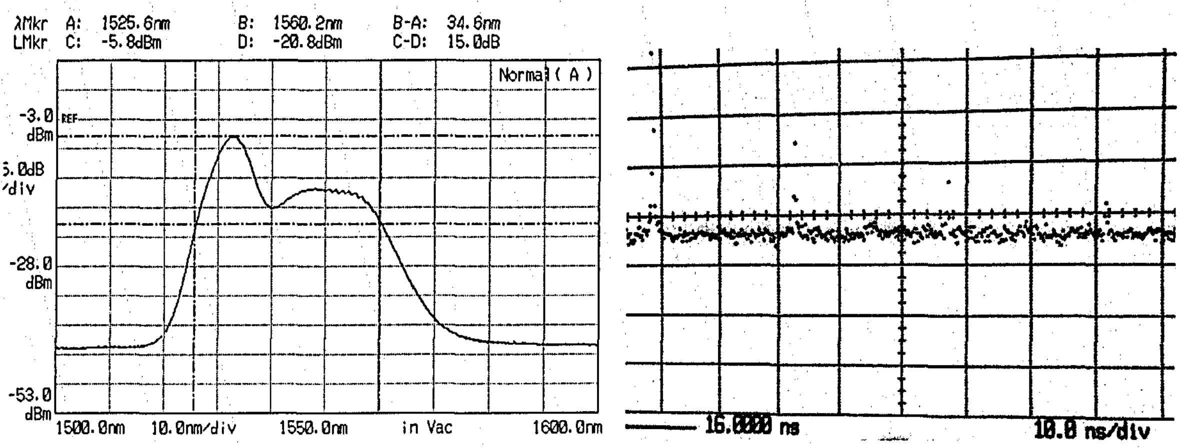

Fig. 5-18: Optical spectrum and time domain of the laser operating in a possible single non-bound soliton mode. Pump power = 75 mW.

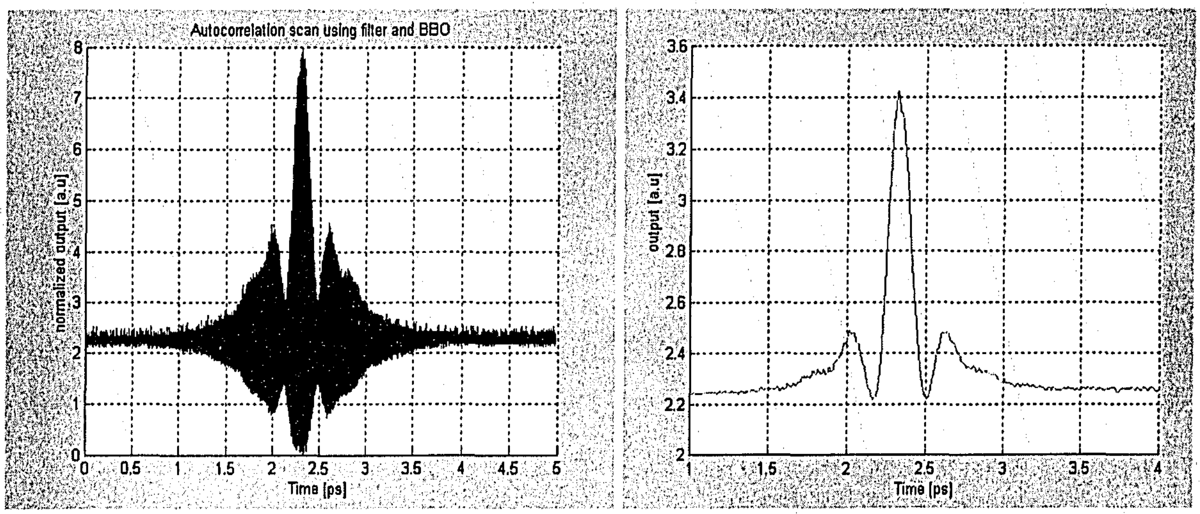

Fig. 5-19: A) Interferometric and intensity autocorrelation trace for single pulse regime. The width of the center peak is approximately 250 fs. Cavity contained 3 m of NUFERN555 EDF and net dispersion of 0.0016 ps^2.

The peak to background ratio of all of the interferometric autocorrelation scans thus far has been 4:1 and 2:1, instead of 8:1 and 3:1, which should be the case if the laser is operating in a short-pulse regime. This is indicative of the noise-like mode of operation discussed in Chapter 3. A feature of a noise like pulse is that the autocorrelation output gives a very narrow pulse, causing one to believe that femtosecond pulses have been obtained. However, the peak to background ratios and the output on the oscilloscope indicated that rather than producing femtosecond pulses the laser was producing pulses hundreds of picoseconds long as shown in Fig. 5-20. The pulse width shown in Fig. 5-20 is a good estimate of the actual pulse width as the bandwidth limit of the detector and scope was estimated to be approximately 100 ps. Associated with the noise-like mode of operation are pulses with low coherence length and broad spectra. Horowitz *et al.* [75] suggested that the 2:1 peak to background ratio of these pulses indicates that the power of the noise-like part of the pulse intensity is similar to the average pulse power, which leads to the conclusion that most of the pulse energy is noise-like and does not have any significant ordered structure. Gong *et al.* [73] attributed narrow pulses with a peak to background ratio of 2:1 to a noise-like pulse with the fine structure of a very narrow pulse. Further they assert that this fine structure has a very rapidly varying time jitter. Noise-like pulses have been produced in long and short cavities, as well as cavities with negative and positive dispersion. The only real consensus on this mode of operation is that it is related to the cavity birefringence. Horowitz and Silberberg [76] suggest the cavity birefringence has to be significant whereas Gong *et al.*[73] were able to produce noise-like pulses with low birefringence cavities. As mentioned earlier, the birefringence of our cavity is unknown and hence it is possible that the conditions in our laser are such that it produces only noise-like pulses.

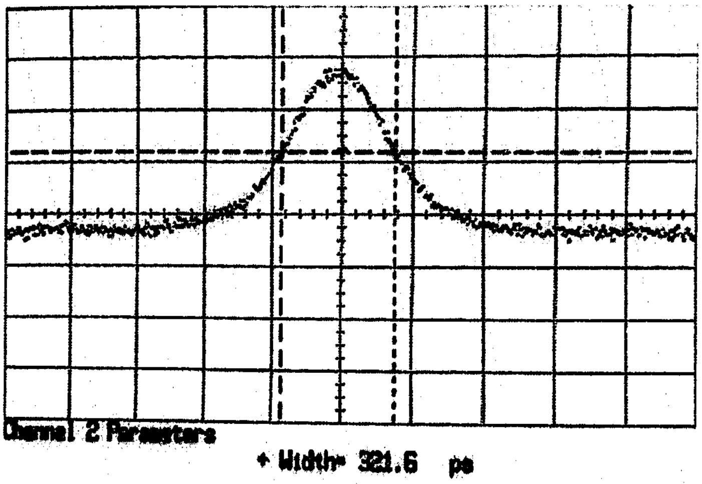

Fig. 5-20: Laser output as seen on the oscilloscope for a noise like pulse.

One interesting property of noise-like pulses is that they can propagate through hundreds of meters of fiber without any change to the narrow coherent peak in the autocorrelation trace. It was believed that this was because the phase distortion caused by the fiber dispersion was relatively weak compared with the initial noise of the pulses and therefore only has a small effect on the coherence [75]. This was tested here by adjusting the lengths of output fiber of the laser while monitoring the autocorrelation trace. The normalized intensity autocorrelation trace is shown is Fig. 5-21. Notice that even after propagating through 10 Km of fiber the width of the coherent spike remained unchanged. This provides strong evidence that the laser was operating in a noise-like regime. A 250 fs transform limited pulse propagating through 2 m of regular fiber would disperse to approximately 430 fs, through 7 m would disperse to 1.25 ps and through 10 km would disperse to 1.75 ns.

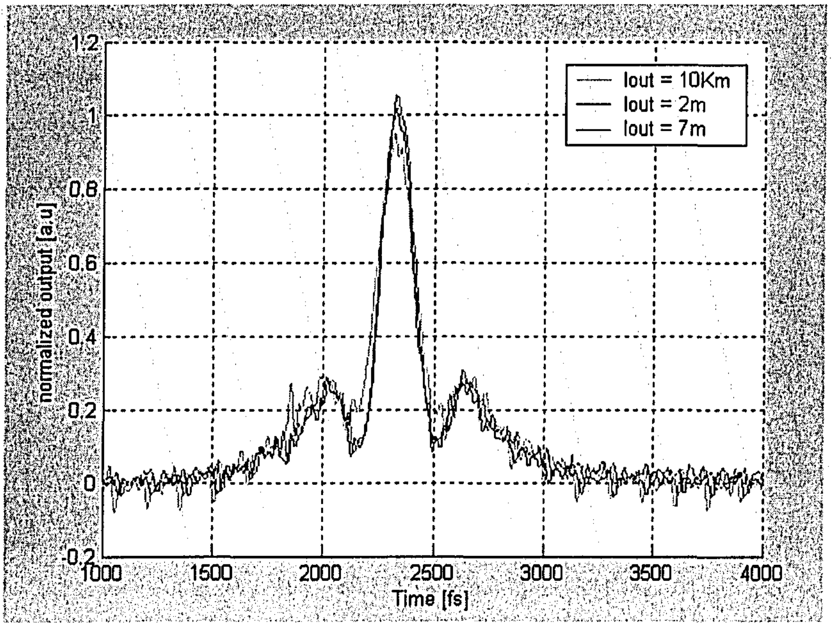

Fig. 5-21: Intensity autocorrelation trace of noise-like pulses after propagating through different lengths of fiber. The width of the center peak remains unchanged with a width of approximately 250 fs. Cavity contained 3 m of NUFERN555 EDF and net dispersion of 0.0016 ps^2.

For the laser described above, no combination of waveplate settings was found that produced short-single pulses. Hence the cavity was changed in an attempt to change the dispersion map and the birefringence. The cavity was changed to a 9 m cavity containing 5 m of NUFERN555 EDF, 2 m of SMF28 and 2 m of Flexcore1060. The net dispersion was estimated to be 0.005 ps^2, slightly higher than the previous cavity. Since this cavity was longer, the birefringence was assumed to be higher. However with a longer length of EDF it was hoped that the increased NPR might enable modelocking in the short-single pulse regime. Chang and Chi [74] theoretically demonstrated that most of the NPR occurs in the EDF where the intensity is high. Hence, increasing the length of EDF should increase the NPR and minimize the possibility of partial modelocking because of insufficient NPR. The optical spectrum and pulse width measured on the oscilloscope for the single pulse operation is shown in Fig. 5-22. The measured pulse width was approximately 250 ps, which was well below the bandwidth limit of the detection system. The autocorrelation trace is shown in Fig. 5-23. Notice that the peak to background ratios for the autocorrelation trace are still not 8:1, further indicating that the laser was still operating in the noise like regime.

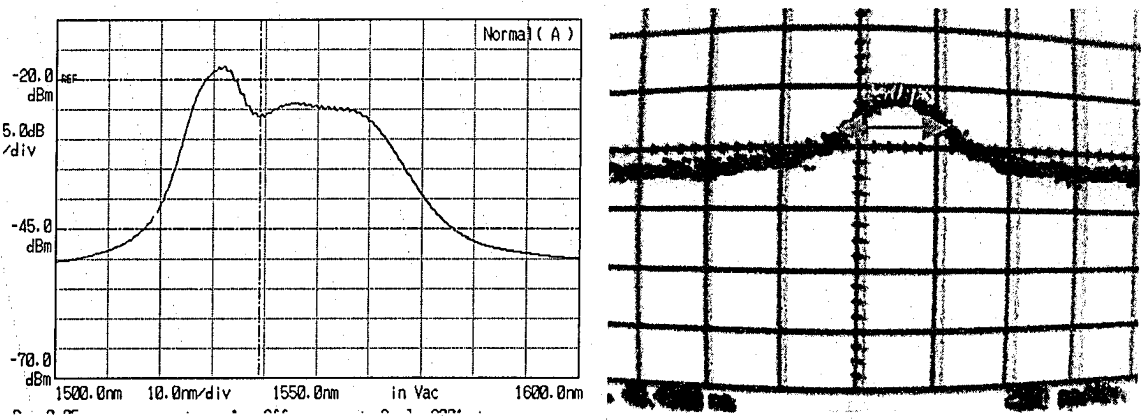

Fig. 5-22: Output of the laser as seen on the spectrum analyzer and the oscilloscope for a single pulse noise-like mode of operation. Cavity contained 5 m of NUFERN555 EDF and net dispersion of 0.005 ps^2. Pump power = 90 mW

The output of the laser was put through various lengths of SMF28 and the autocorrelation traces were monitored. As can be seen from Fig. 5-24, the width of the central peak does not change significantly for different lengths of output fiber. This shows that the fiber dispersion had very little effect on the pulse width. No combination of waveplate settings was found that would produce truly modelocked operation. With this cavity, the bound soliton state was also unobtainable. However, multiple pulses were easily obtained by increasing the pump power until the spectrum became unstable.

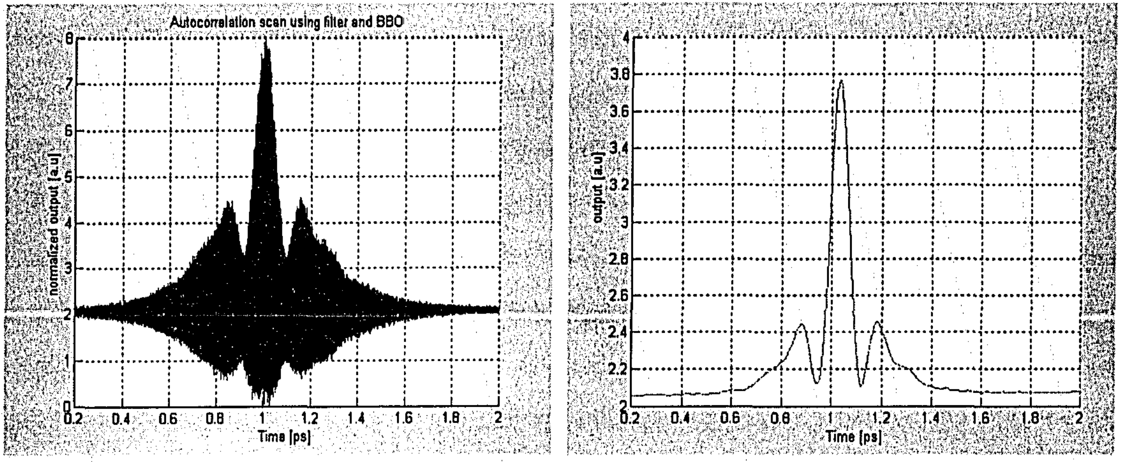

Fig. 5-23: Autocorrelation trace for a single pulse noise-like mode of operation for a cavity containing 5 m of NUFERN555 EDF and net dispersion of 0.005 ps^2.

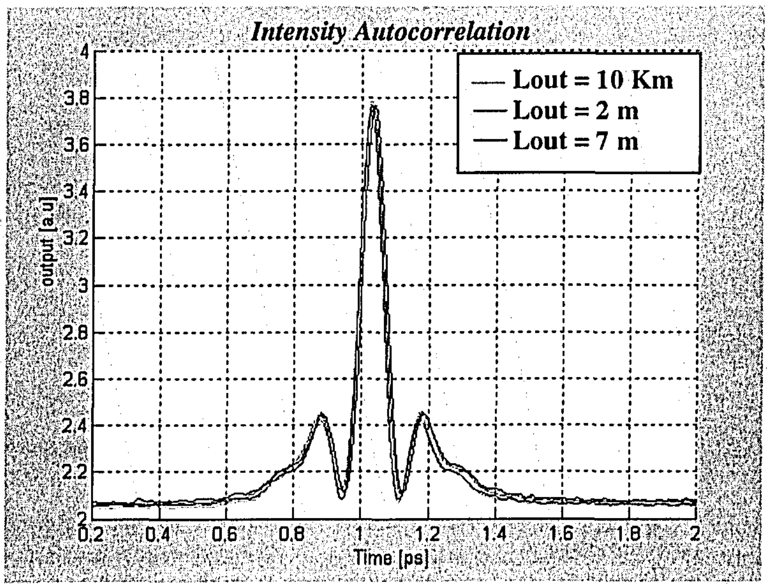

Fig. 5-24: Laser output after propagating through different lengths of output fibers.

The amount of SMF28 in the cavity was then increased to 3 m in another attempt to change the dispersion map (a net negative dispersion) and the output was monitored using the autocorrelator. Short-pulse mode of operation remained elusive. The amount of SMF28 was then reduced to 1 m and the autocorrelation trace was monitored as the polarization controllers were adjusted. Again only the noise-like mode of operation was obtained. It was suspected that the estimation for the dispersion and birefringence of the NUFERN555 EDF was not accurate enough to design a cavity that was capable of producing short pulses.

Using the NUFERN555 EDF the only stable mode of operation supported by the laser was the noise-like mode. This lead to the conclusion that the birefringence of this fiber was significant and that the dispersion is also much more positive than we have estimated. Hence a new cavity was constructed using a different type of EDF. The cavity contained 2 m NOI Er-123 EDF, 0.75 m of SMF28 and 0.5 m of Flexcor1060. The dispersion of the EDF was estimated to be approximately 0.0102 ps^2/m, making the net cavity dispersion approximately 0.004 ps^2.

Pulsed operation was obtained by carrying out the procedure outlined in Section 5.1.1. The pump power was increased to the point where there was no adjustment of the polarization controller that could produce a stable spectrum. It was then reduced slightly below that point. At this point the laser should be in a single pulse regime or perhaps the bound soliton state as discussed above. The laser output as seen on the spectrum analyzer and the oscilloscope is shown in Fig. 5-25. The spectrum and the pulse train are fairly stable in time.

From the output on the oscilloscope the laser does appear to be operating in the single pulse regime. However, looking at the autocorrelation trace in Fig. 5-26, it can be seen that the laser is actually operating in a mode that is often referred to as a bunch state [73]. The oscilloscope trace did not reveal this because of the bandwidth limitation of the detection system. In this state, the pulses are bunched together around the main pulse. This state is different from the bound soliton state as the height of the side peaks are not insignificant compared to the center peak. It was reported [73] that a reduction in the pump power should change this state to the single pulse state. The autocorrelation trace in Fig. 5-27 shows the autocorrelation trace when the pump power is reduced to 125 mW.

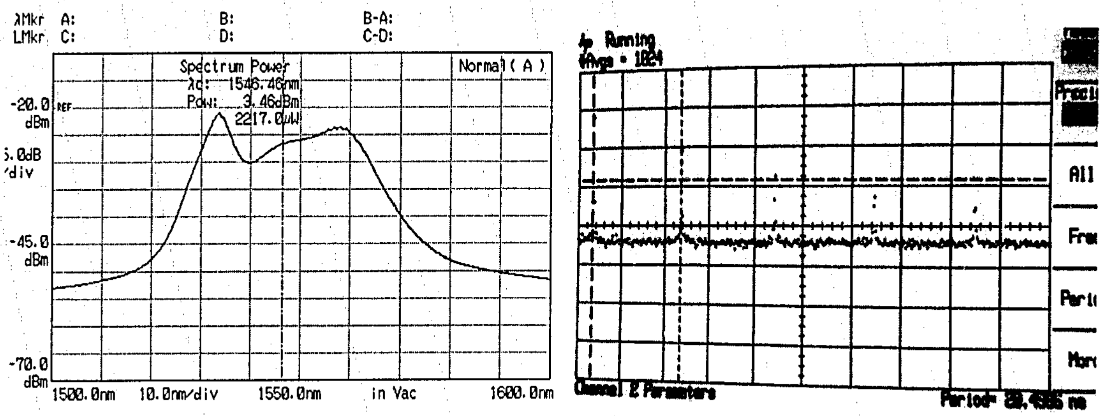

Fig. 5-25: Laser output as seen of the spectrum analyzer and the oscilloscope for a cavity containing 2 m of NOI Er-123 EDF. Pump power = 150 mW.

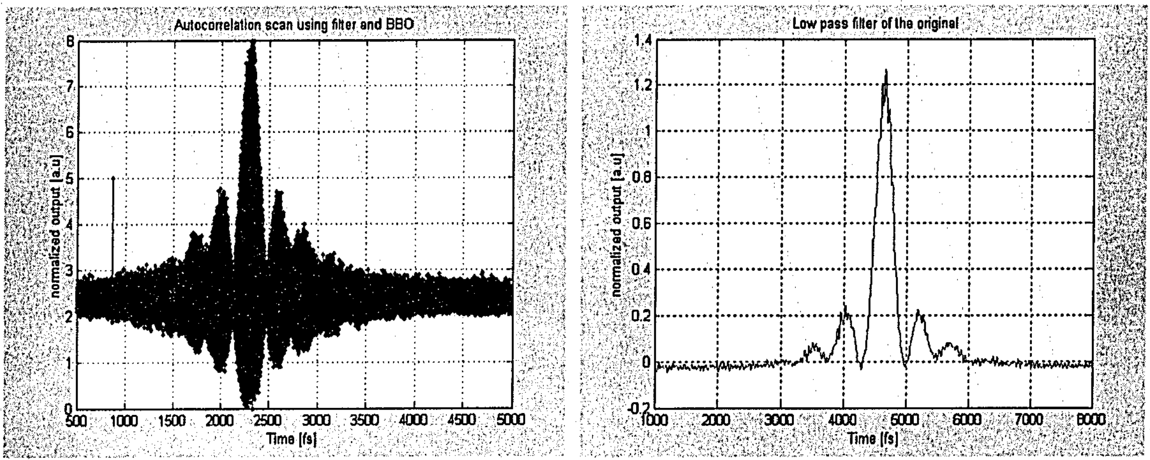

Fig. 5-26: Autocorrelation trace for bunched pulse state for pump power of 150 mW.

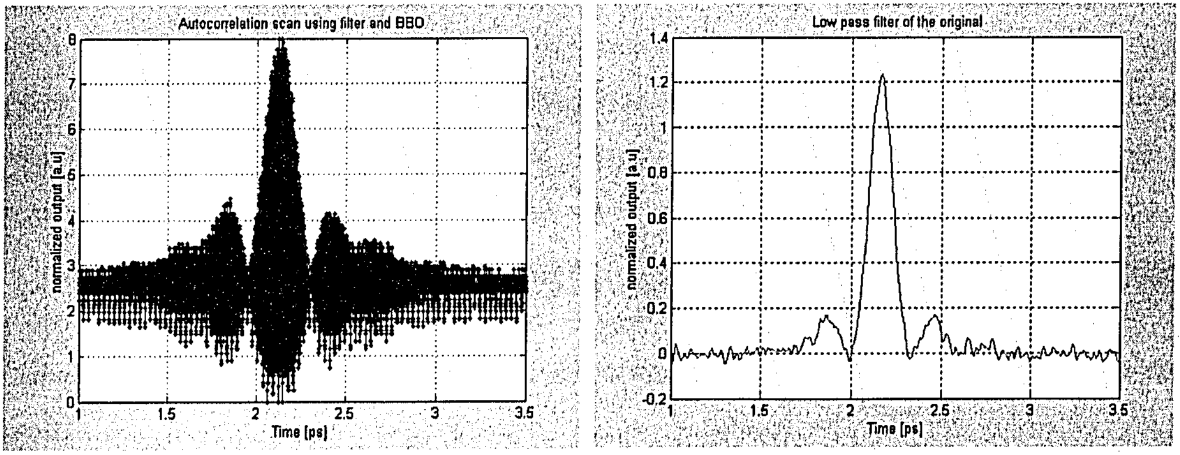

Fig. 5-27: Autocorrelation trace for single pulse state for pump power of 125 mW.

Notice that the laser was still operating in the noise-like mode. No combination of waveplate adjustments, cavity configuration, or pump power was found that produced a stable short-pulse regime. This might be due to the birefringence of the cavity, as discussed previously. In an attempt to reduce the birefringence, the cavity was shortened by reducing the length the EDF. A new cavity was constructed using 1 m of NOI Er-123-1 fiber, which was almost identical to the NOI Er-123 with the exception that it has a higher absorption coefficient (higher Er concentration) and hence the pump threshold was much higher. The cavity consisted of 1 m of NOI Er-123-1 EDF, 0.7 m of SMF28 and 0.5 m of Flexcor1060. The net cavity dispersion was approximately -0.0087 ps^2. This is the shortest cavity that could be constructed, limited by the pigtails on the isolator and WDM. The optical spectrum and pulse train is shown in Fig. 5-28. The corresponding autocorrelation trace is shown in Fig. 5-29. The average output power for this configuration was approximately 1 mW.

Reducing the pump power did not have a significant effect on the output of the laser, other than a reduction in the average power. For pump powers below 120 mW, the laser stopped lasing. For pump powers above 220 mW the laser entered the multiple-pulse regime.

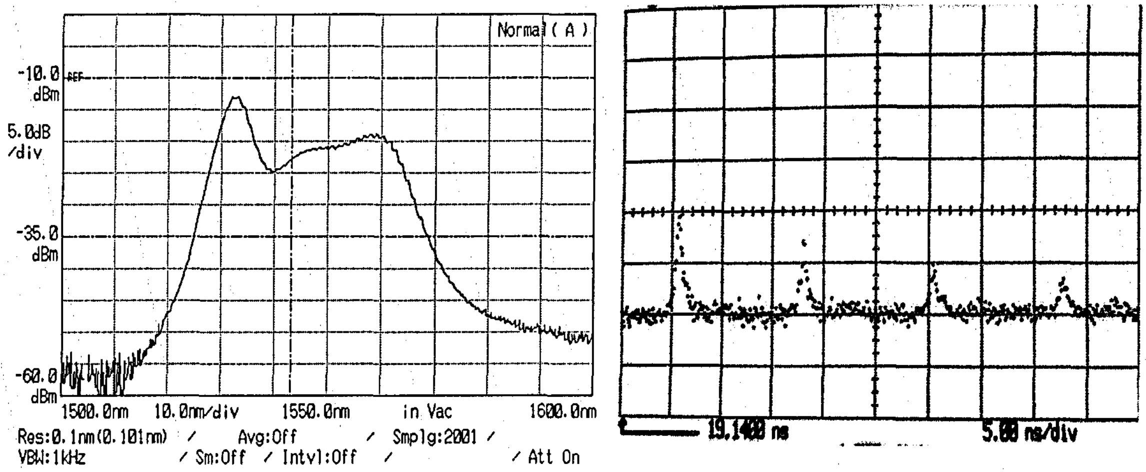

Fig. 5-28: Laser output as seen on the spectrum analyzer and oscilloscope for the single pulse regime. Pump power = 220 mW for cavity containing 1 m of NOI Er-123-1.

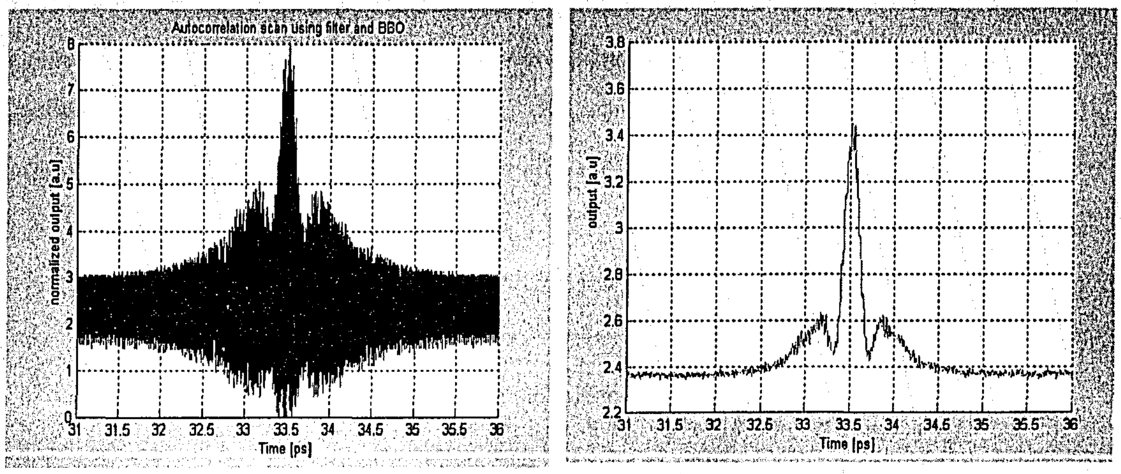

Fig. 5-29: Interferometric and Intensity autocorrelation trace for single pulse regime.

The noise-like and multiple-pulse modes were the only modes of operation obtainable for this cavity configuration. In an attempt to change the dispersion map, the amount of SMF28 in the cavity was increased to 3 m, for an estimated net cavity dispersion of – 0.059 ps^2. Pulsed operation was obtained by properly adjusting the polarization controllers. The pump power was then slowly increased until the spectrum became unstable. The laser should now be in a multiple-pulse, bound-soliton or bunched state. The optical spectrum and output as seen on the oscilloscope is shown in Fig. 5-30. It appeared as though the laser was operating in either a multiple bunched-soliton or multiple bound-soliton mode with pulse separation of approximately 5 ns. From the autocorrelation trace shown in Fig. 5-31 it appears as though it was the multiple bound state with three or perhaps four bound solitons. Varying the pump power and monitoring the autocorrelation trace confirmed this. Recall that variation in pump power should have very little effect on bound solitons. The intensity autocorrelation trace for varying pump powers is shown in Fig. 5-32. The pump power was varied from 200 mW to 140 mW. Over this range the optical spectrum was stable, i.e. there were no spikes in spectrum.

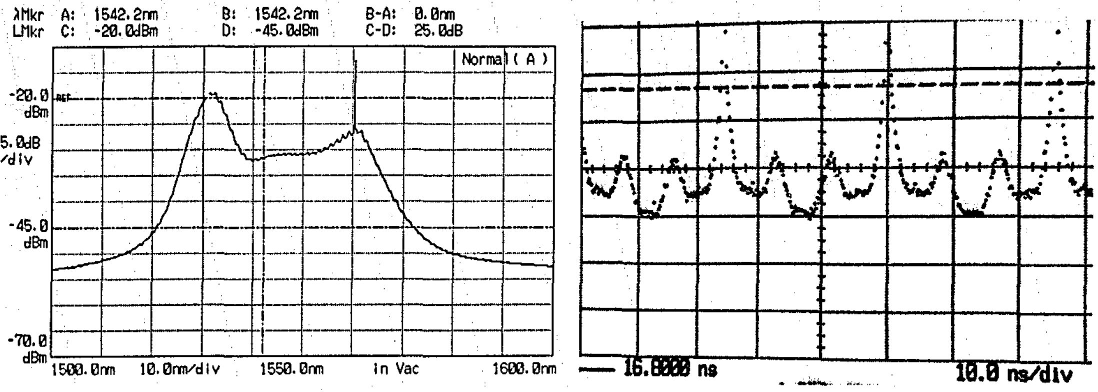

Fig. 5-30: Optical spectrum and oscilloscope picture for the 1 m of NOI Er-123-1 EDF cavity with a net dispersion of –0.059 ps^2. Pump power = 220 mW.

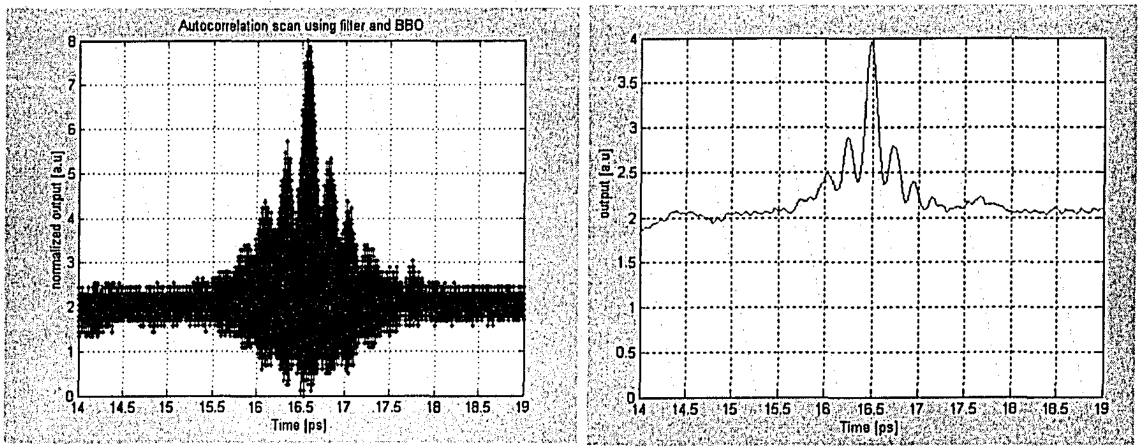

Fig. 5-31: Intensity and autocorrelation trace for 3 bound solitons. For the 1 m of NOI Er-123-1 EDF cavity with a net dispersion of –0.059 ps^2. Pump power = 220 mW.

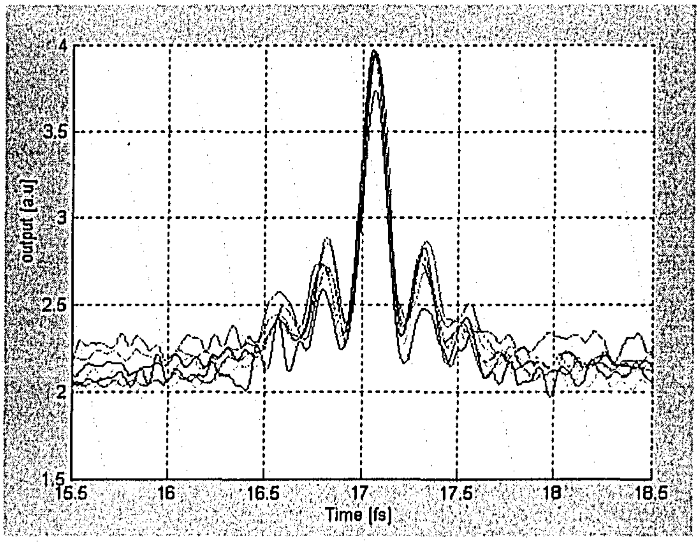

Fig. 5-32: Intensity autocorrelation trace of three bound solitons for pump powers varying from 200 mW to 140 mW.

For this cavity configuration and setting of the polarization controllers, the laser was apparently operating in the bound soliton regime. In an attempt to obtain the single pulse mode, the pump power was reduced to threshold and the polarization controllers readjusted to obtain modelocking. The spectrum and oscilloscope trace is shown in Fig. 5-33. Notice that the spectrum was completely different from the one in Fig. 5-30. This was an indication that the laser might be operating in a mode other than bound-soliton mode. The corresponding autocorrelation trace is shown in Fig. 5-34. In this mode of operation the average power was only 0.5 mW and the autocorrelation trace is noisy.

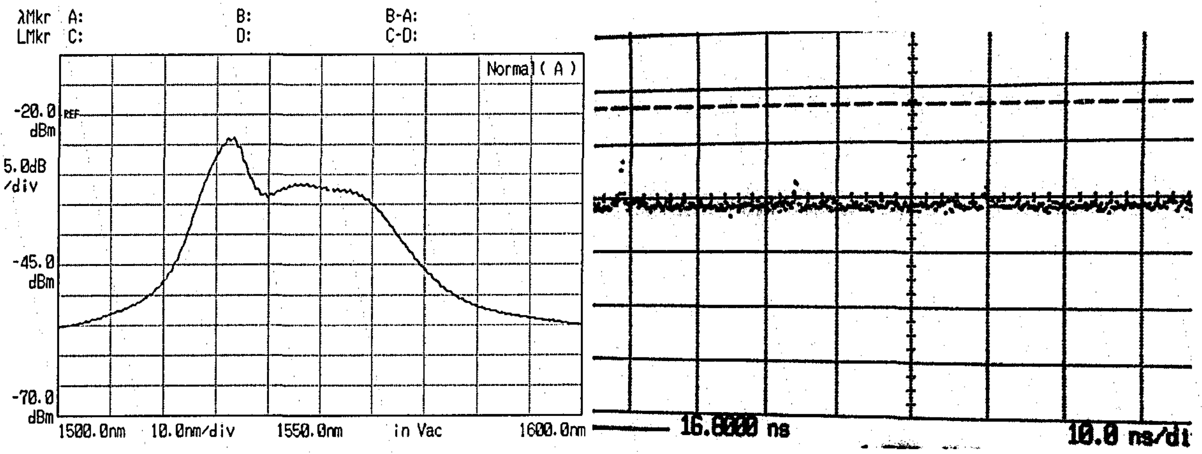

Fig. 5-33: Optical spectrum and oscilloscope picture for the laser operating in single pulse regime, for the 1 m of NOI Er-123-1 EDF cavity with a net dispersion of –0.059 ps^2. Pump power = 145 mW.

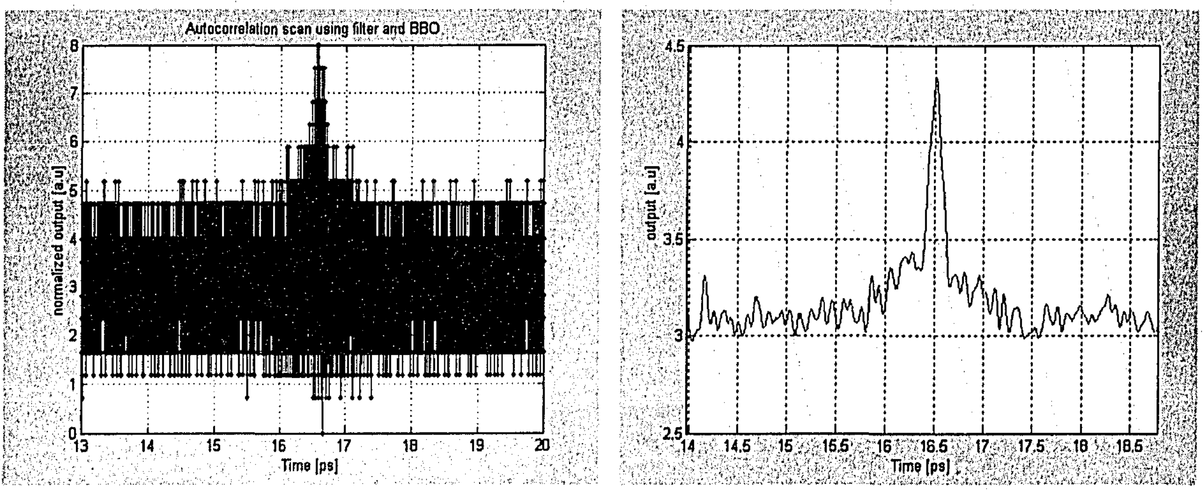

Fig. 5-34: Interferometric and intensity autocorrelation trace for the 1 m of NOI Er-123-1 EDF cavity with a net dispersion of –0.059 ps^2. Pump power = 145 mW.

Based on the autocorrelation trace it was difficult to conclude if this was truly a single pulse regime. What could be concluded was that the laser was not operating in the short-pulse mode but rather it was still operating in the noise like mode.

Usually the spectrum for bound solitons and bunched solitons is strongly modulated, reflecting the phase relationship between the pulses [77]-[79]. For the laser discussed in this section however, this was not the case. It was speculated that since this laser was operating in the noise-like mode, which is equivalent to the laser not being fully modelocked, the phase relationship between the modes was not very strong. Hence the spectra did not appear to be strongly modulated. It was not fully understood why full modelocking to obtain the short pulse mode could not be obtained for the cavities used. The unknown dispersion and birefringence of the fiber were believed to play a role. Also, there was limited precision possible when adjusting the PCs. The alignment of the fiber axis and the input polarization is reported crucial to obtaining modelocking [80]. Salhi *et al.* [80] theoretically demonstrated that the region of stable modelocking becomes extremely small as the angle between the eigenaxes of the SMF28 and EDF becomes large. This was demonstrated by Fig. 5-35 taken from [80] where θ_+ is the angle between the eigenaxes of the EDF and the "passing" axis of the polarizer and θ_- is the angle between the eigenaxes of the SMF28 and the "passing" axis of the polarizer. The passing axis of the polarizer refers to the transmission axis of the PBS. The figure shows the regions of operation when the angle (α) between the eigenaxes of the two fibers is 0 ° and 135 ° for a net cavity dispersion of 0.037 ps^2. The behaviour for a slightly different dispersion and α is shown in Fig. 5-36.

The modelocking regime was found to have the largest stable region when $\alpha = 0$, 90 or 180 °. Conversely the region was the smallest when $\alpha = 45$ and 135 °. Hence the modelocking regime is more efficient when the eigenaxes of the doped and undoped fibers are aligned, i.e. when $\alpha = 0$ or 90 °. When the GVD was reduced, modelocking was found to occur in a smaller region and the shape of the stable region is different from Fig. 5-35. These results illustrate that alignment of the fiber axes is crucial in order to obtain stable modelocking.

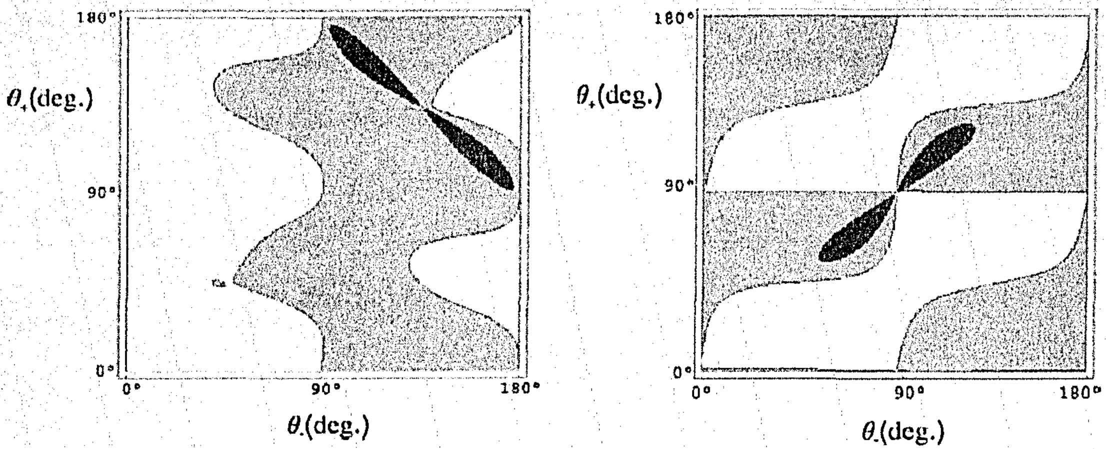

Fig. 5-35: Stability regions of the CW and the modelocked regimes in the plane $(\theta.\ \theta_+)$ for a total cavity dispersion of 0.037 ps^2 and (a) $\alpha = 0$ ° and (b) $\alpha = 135$ °. In the white region, the CW regime is stable, in the light gray region both the CW and the modelocked regimes are unstable; and in the dark gray region the modelocked regime is stable [80].

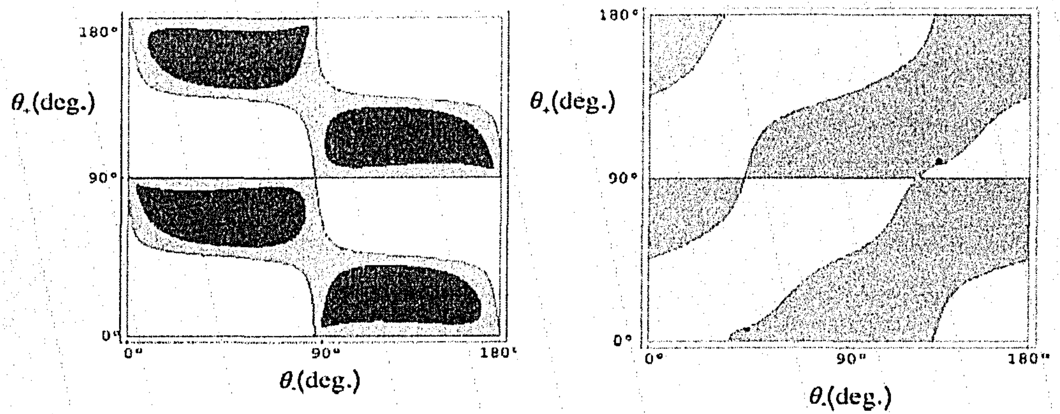

Fig. 5-36: Stability regions of the CW and the modelocked regimes in the plane $(\theta.\ \theta_+)$ for a total cavity dispersion of 0.011 ps^2 and (a) $\alpha = 5$ ° and (b) $\alpha = 89.5$ °. In the white region, the CW regime is stable, in the light gray region both the CW and the modelocked regimes are unstable; and in the dark gray region the modelocked grime is stable [80].

In an attempt to address the alignment problem, shorter lengths of SMF28 were tested using the alignment procedure outlined in Section 5.1.1. For the longer cavities shown in Table 5-1, the alignment process became extremely difficult because the isotropic assumption no longer holds. In an attempt to better align the fiber axes, in this case, a polarization controller was placed between the two sections of fiber. This added another degree of freedom to the alignment process, increasing the alignment difficulty. Modelocking in the short-pulse regime was still unobtainable.

5.1.5 Summary and discussion of results for Stretched pulse NPR laser

Although several experiments were performed, a short pulse mode of operation was not obtained. Long cavities “with little or no dispersion management” reportedly have a tendency to operate in the noise-like regime [57]. Hence the cavities in the experiments were kept relatively short and an attempt was made to balance the dispersion. However because the dispersion of the EDF was not known, it was difficult to conclude that the dispersion balance criterion was met. This, coupled with the fact that the birefringence of the EDF was unknown, made the design of the laser cavity extremely challenging. Another obstacle was the alignment of the fiber axes. There is no published work on how to experimentally align these lasers, but there are several theoretical studies that indicate the importance of the alignment of the fiber axes and the input state of polarization [71],[74],[80].

Similar to the experiment performed by Horowitz *et al.* [75], the effects of the birefringence combined with the gain response of the EDF were experimentally observed when the laser was operated in CW mode. By varying the polarization controller the lasing wavelength (frequency) could be varied between approximately 1535 nm and 1565 nm for the Nufern555 EDF as shown in Fig. 5-37, and between approximately 1555 nm to 1562 nm for the Er-123 EDF as shown in Fig. 5-38. As explained in [75], this tunability is attributed to the birefringence of the EDF. From this experiment we are able to conjecture that the birefringence of the Nufern555 EDF was much higher than that of the Er-123 EDF. This also might explain why the modelocked spectrum was different for different polarization controller settings as shown in Fig. 5-39. The non-Gaussian spectrum shape was believed to be due to the combined effect of GVD and SPM in the cavity. Further, the output was taken from the rejection port of the PBS after the EDF section, where the pulses are believed to be strongly chirped. All of these factors contribute to a non-Gaussian spectrum shape. Finally, these types of spectra are common for this type of laser [57].

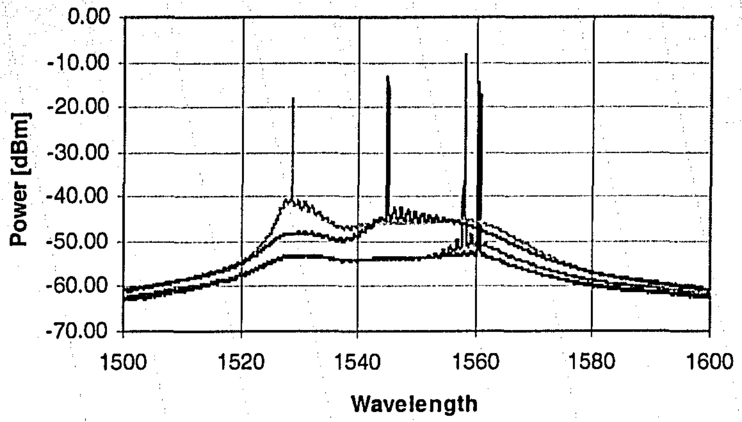

Fig. 5-37: CW spectra for varied settings of the polarization controllers for a cavity consisting of 3m of Nufern555 EDF.

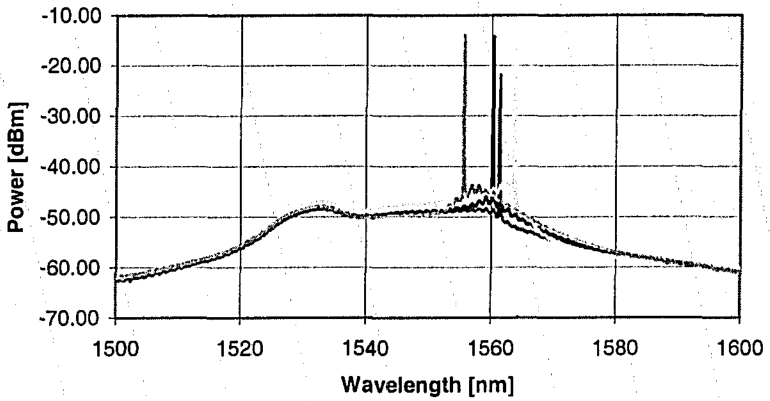

Fig. 5-38: CW spectra for varied settings of the polarization controllers for a cavity consisting of 1m of Er-123 EDF.

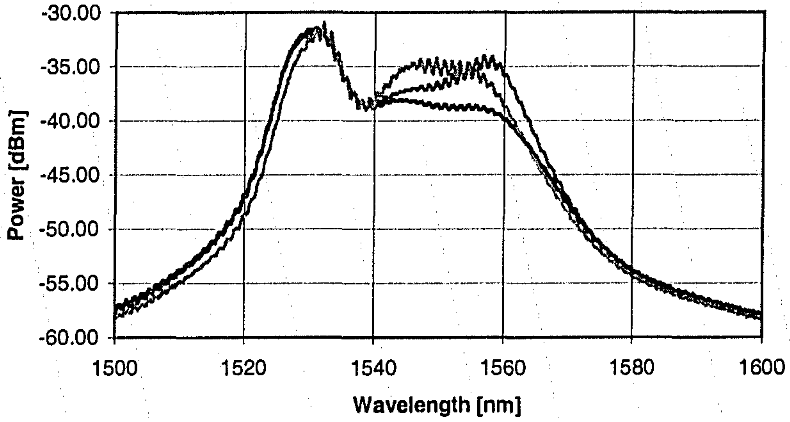

Fig. 5-39: Modelocked spectra for varied settings of the polarization controllers for a cavity consisting of 3 m of Er-123 EDF.

In summary, the only stable mode of operation for the laser discussed in this section was the noise-like mode. This mode of operation has many advantages over the conventional short pulse mode. The spectrum and pulse train were extremely stable over time. Adjusting the parameters of the cavity allowed control over some properties of noise-like pulses, such as average power and pulse duration. Horowitz and Silberberg previously demonstrated successful control of noise-like pulses [76]. They were able to obtain relatively intense noise-like pulses with a width of a few picoseconds. Lasers of this type could have applications in areas where low-coherence sources with broad spectra are needed. Unlike most sources of low-coherence light, these lasers can produce relatively high peak power in a well-defined pulse shape. Noise-like pulses have actually been used for interrogating an array of fiber gratings [83].

5.2 Stretched pulse figure-8 laser with NOLM

Additive pulse modelocking can also be obtained by using a NOLM as discussed in Chapter 3. This section discusses the results from an attempt to construct a stretched pulse NOLM laser. The schematic of the laser setup is shown in Fig. 5-40. This laser was different from the stretched pulse NPR laser discussed in Section 5.1, in the sense that it was an all fiber cavity and APM action was achieved by constructive/destructive interference effect of the counterpropagating pulses at the variable coupler. The cavity consisted of 2.25 m of Flexcor1060, 4.85 m of SMF28 and 2 m of NOI EDF (GVD = 0.058 ps^2/m), making the total cavity dispersion for both rings approximately -0.0065 ps^2.

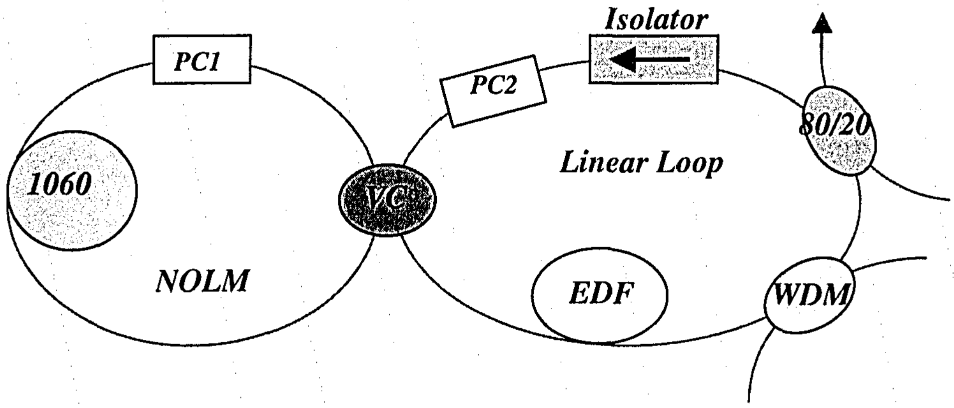

Fig. 5-40: Schematic of the experimental configuration for the stretched pulse figure-8 NOLM laser. PC1 and PC2 – polarization controllers, EDF – Erbium doped fiber, VC – Variable coupler, 1060 – Flexcor1060 fiber and WDM – Wavelength division multiplexed coupler.

5.2.1 Obtaining pulsed operation

Pulsed operation was obtained by adjusting the variable coupler so that the coupling ratio was close to 50/50 and subsequently adjusting the polarization controllers. Pulsed operation was obtained for relatively low pump power of approximately 20 mW. Since nonlinear polarization rotation does not play a role in this cavity configuration, no attempts were necessary to align the eigenaxes of the fibers. Usually for a cavity of this type some sort of external perturbation [81] or a semiconductor saturable absorber is needed inside the cavity [82] in order to initiate modelocking. For the laser discussed in this section the possibility of obtaining modelocking without employing either of these was investigated.

5.2.2 Modes of Operation

For pump powers above 20 mW the laser appeared to be working in the multiple-bound soliton regime. The optical spectrum and oscilloscope picture is shown in Fig. 5-41. The average output power for this configuration was approximately 0.25 mW, too low to perform an autocorrelation scan with our setup. For the polarization controller and coupling ratio settings described above, this was the only mode of operation obtainable.

From Fig. 5-41 it appeared that the laser was not operating in a stable short pulse regime. The spectrum is typical of a laser that was operating in the bound soliton regime or what is sometimes referred to as phase-locked soliton pairs [79]. From the time domain, it is clear that the laser is producing nanosecond pulses, suggesting that the laser was operating in the noise-like regime.

For a small adjustment of the variable coupler and the polarization controller, a multiple pulse mode, possibly the bunched soliton state, was obtained. The optical spectrum and oscilloscope picture is shown in Fig. 5-42. This mode was extremely unstable and the average output power was too random to obtain a proper autocorrelation trace. The pulses were separated by 1ns, too large a separation to say that this was the bound-soliton state. This mode also produced unstable nanosecond pulses.

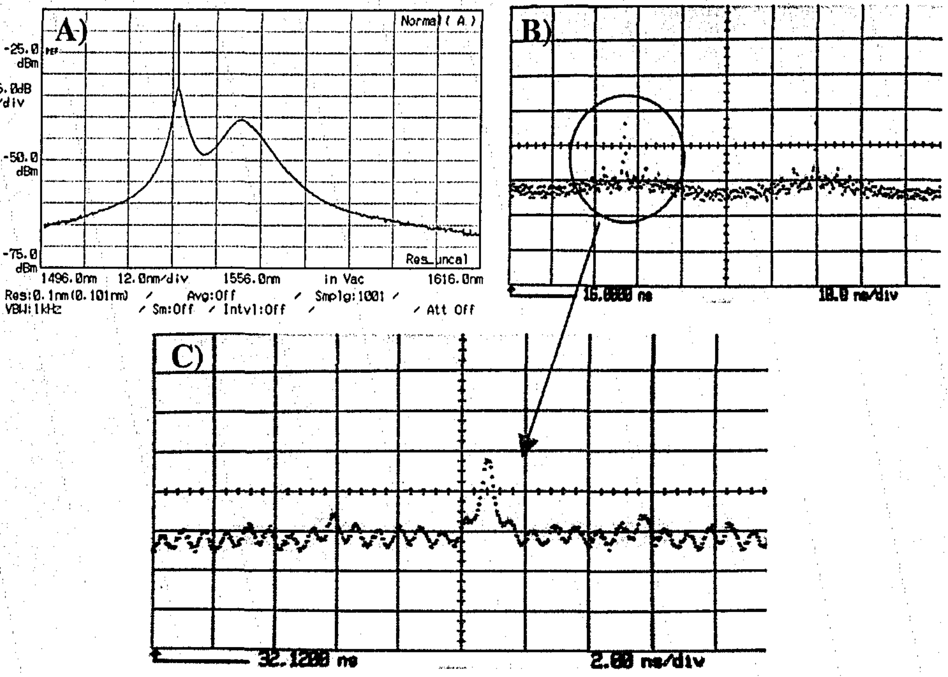

Fig. 5-41: Stretched pulse NOLM output for net cavity dispersion of –0.0065 ps^2 and pump power of 20 mW. A) Output spectrum, B) Time domain as seen on the oscilloscope, and C) Zoomed in on one of the pulses on the scope.

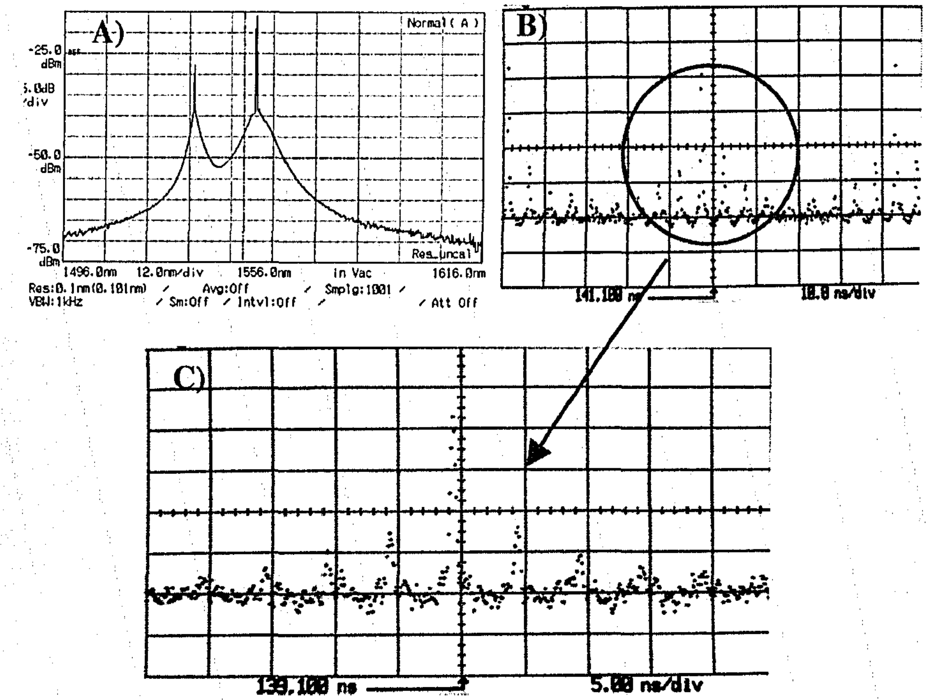

Fig. 5-42: Stretched pulse NOLM output for net cavity dispersion of –0.0065 ps^2 and pump power of 20 mW. A) Output spectrum, B) Time domain as seen on the oscilloscope, and C) Zoomed in on one of the pulses on the scope. The polarization controller and variable coupler setting were readjusted for this experiment.

The pump power was reduced and the polarization controllers adjusted until what appeared to be a single-pulse mode was obtained. The optical spectrum and oscilloscope picture are shown in Fig. 5-43.

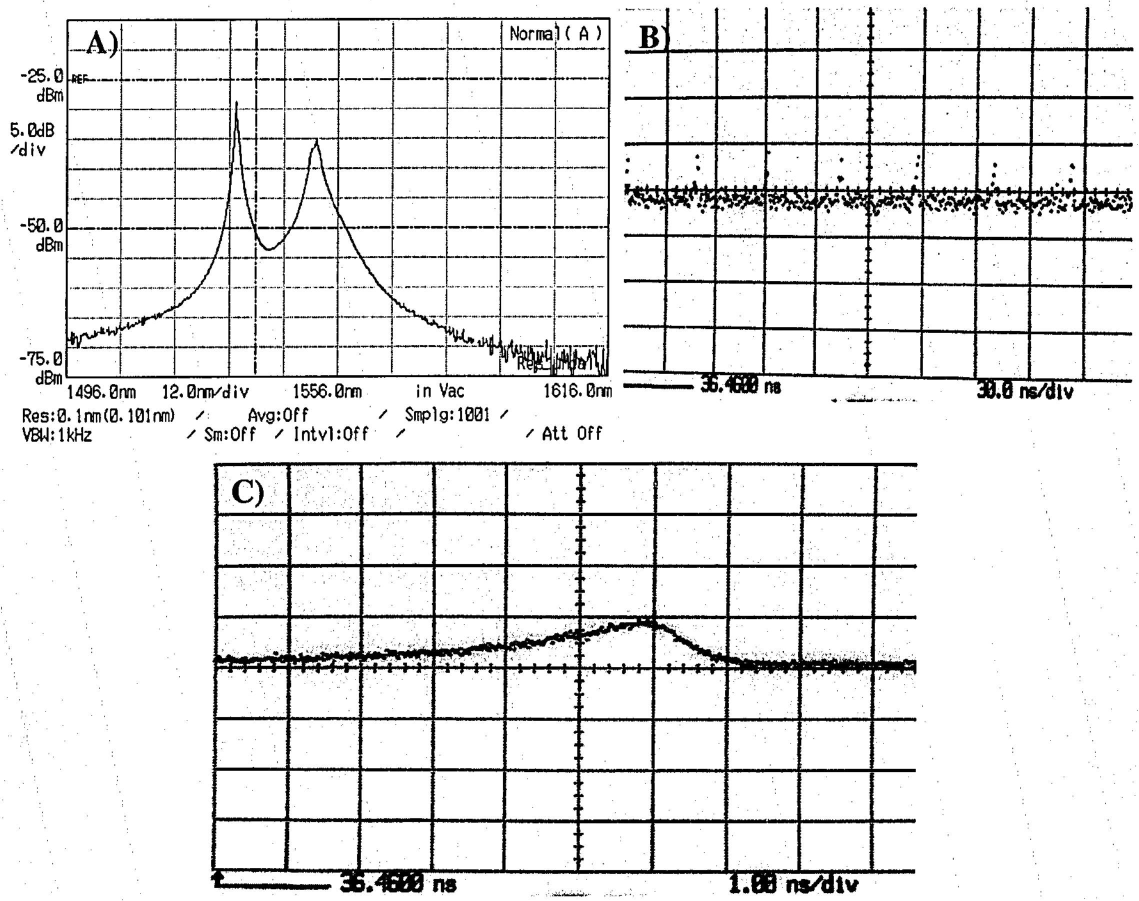

Fig. 5-43: Stretched pulse NOLM output for net cavity dispersion of –0.0065 ps^2 and pump power of 13 mW. A) Output spectrum, B) Time domain as seen on the oscilloscope, C) Zoomed in on one of the pulses on the scope.

The output shown in Fig. 5-43 was very interesting, particularly the oscilloscope trace. This was the first time a pulse of this nature was seen, where the rise time was longer than the fall time. At first glance this was thought to be due to slow saturable absorber shaping. This is not likely, however, as the saturable absorber action of these lasers is fast compared to the relaxation time of the gain medium. (The gain relaxation time for Er is approximately 1 ms). It was surmised that this shaping was more likely due to the fact that the laser was operating in the noise-like mode that had a very rapidly varying time jitter that tended to smear out the oscilloscope trace. Similar results were obtained by Gong *et. al.* for the noise-like mode of operation [73]. To verify that the laser was indeed operating in the noise-like mode an autocorrelation scan was performed and the output is shown in Fig. 5-44. The measured pulse width based on the autocorrelation traces is approximately 2 ps and the peak to background ratio is not 8:1, indicating that the laser was operating in the noise-like regime.

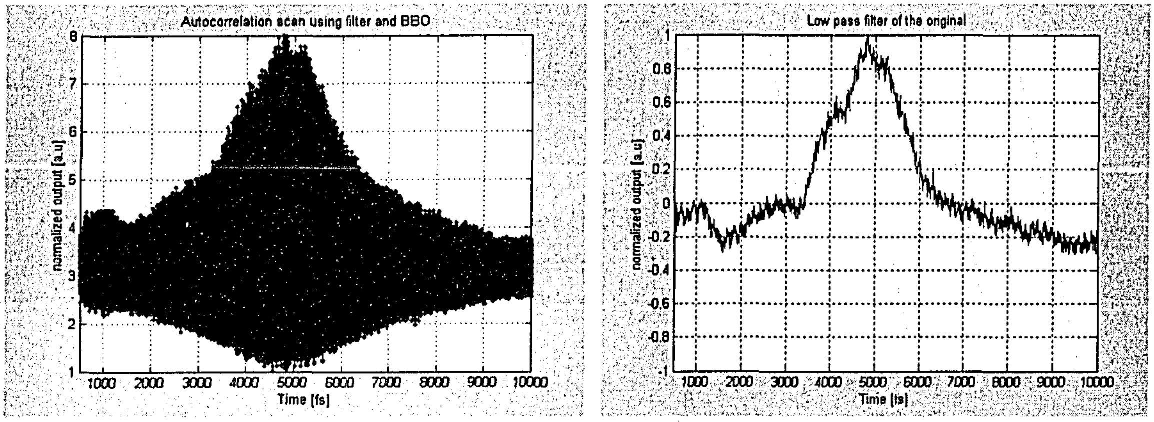

Fig. 5-44: Interferometric and Intensity autocorrelation trace for stretched pulse NOLM operating in the noise-like mode.

Several attempts were made to modelock the NOLM laser in the short pulse regime but without success. Various EDF, cavity lengths and net dispersion were tried but the short pulse mode was unobtainable. It was concluded that modelocking in the short pulse regime could not be obtained without the use of some sort of external perturbation or an actual saturable absorber to initiate modelocking.

5.3 Comparison of NOLM and NPR lasers

Stretched pulse NOLM lasers are said to be more stable against environmental affects than Stretched pulse NPR lasers. The increase stability is said to be due to the fact that the NOLM operation does not depend on polarization directly [82].

The NOLM laser has also been reported to produce pulses with clean smooth spectra compared to the spectra from the NPR laser [82]. The difference between the spectra was not very noticeable in the lasers discussed in this thesis. This was most likely due to the fact that the NOLM was not modelocked properly. Another advantage of the NOLM is that the pulses from the laser do not contain the "wings" as those from the stretched pulse laser [82]. This is noticeable when comparing the autocorrelation traces in Fig. 5-44 and Fig. 5-27. Pulses without "wings" and a clean smooth spectrum are attractive properties in lasers that are used for spectroscopic and characterization experiments.

5.4 Actively modelocked fiber ring laser

Active modelocking can be obtained by using an amplitude modulator as discussed in Chapter 3. This section discusses the results from the experimental realization of an actively modelocked fiber ring laser. The schematic of the laser setup is shown in Fig. 5-45. The cavity consisted of 9m of SMF28, 3 m of Flexcor1060 and 10 m of 3M EDF (GVD ~ 0.08 ps^2/m), making a 22m long cavity with a net dispersion of approximately 0.581 ps^2. The net cavity dispersion is much higher than those for the passive laser. As discussed in Chapter 3, higher dispersion can be beneficial in harmonically modelocked fiber lasers, enabling a stable tunable source [87].

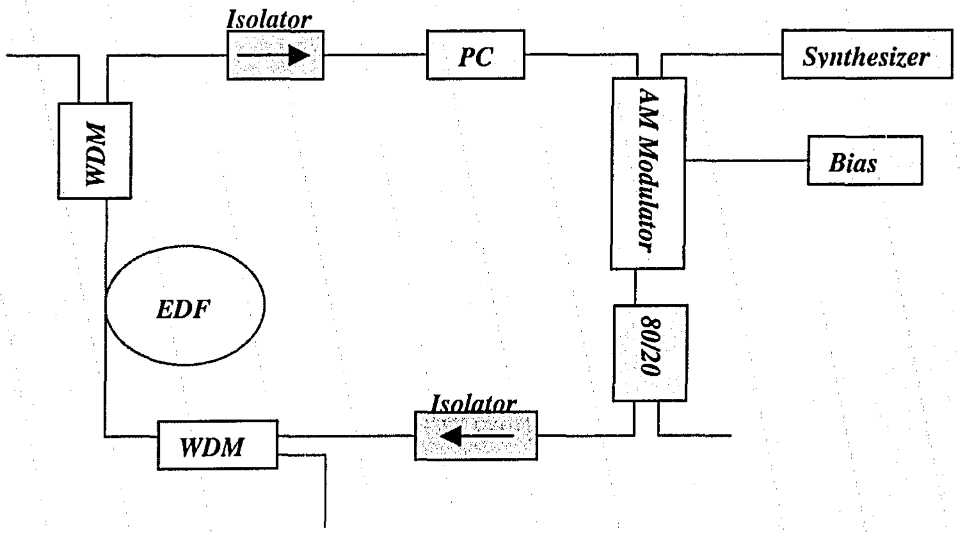

Fig. 5-45: Schematic of the experimental configuration for the actively modelocked fiber ring laser.

5.4.1 Obtaining modelocking and investigating the regimes of operation

Modelocking was obtained by setting the modulation frequency to the fundamental frequency of the cavity (or one of its harmonics) and subsequently adjusting the polarization controller and the modulator bias, to ensure that the intracavity loss was low. Modelocking was obtained for a relatively low pump power of approximately 25 mW, and with the modulator bias set to approximately 4.5 V. Fig. 5-46 shows the output spectrum and oscilloscope trace when the modulation frequency was set to 9.9723 GHz, which is close to the 1097th harmonic of the fundamental frequency (9.091 MHz). The measured pulse width was approximately 13.5 ps.

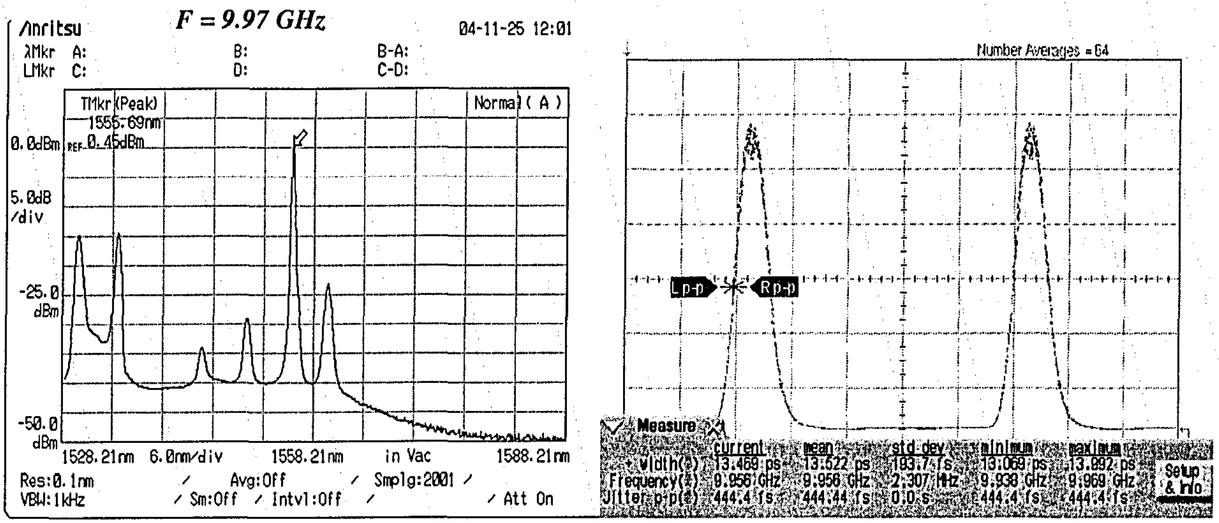

	current	mean	std dev	minimum	maximum
+ Width(2)	13.469 ps	13.522 ps	193.7 fs	13.069 ps	13.892 ps
Frequency(2)	9.956 GHz	9.956 GHz	2.307 MHz	9.938 GHz	9.969 GHz
Jitter p-p(2)	444.4 fs	444.44 fs	0.0 s	444.4 fs	444.4 fs

Fig. 5-46: Optical spectrum and oscilloscope trace for a harmonic actively modelocked fiber laser when the modulation frequency is set to the 1097th harmonic (9.97 GHz).

From the output spectrum it can be seen that the laser is operating in a multi-wavelength regime. This is not uncommon for long cavities with large positive dispersion [87]. In fact this can be exploited for obtaining tunable operation by adjusting the modulation frequency [86],[87]. For the laser discussed above, single wavelength operation was unobtainable regardless of the modulation frequency. However by changing the modulation frequency and the modulator bias, the number of wavelengths could be reduced and wavelength tunability was observed. This will be shown in the results that follow.

The output spectra when the laser is modulated at the 1012th and 1022nd harmonic are shown in Fig. 5-47. Notice that the laser is still operating in the multi-wavelength mode but the number of modes have been reduced to three. Also notice that the wavelengths have been shifted. The intensity autocorrelation and oscilloscope trace, when the laser is modulated at the 1012th harmonic, are shown in Fig. 5-48. The output is very similar when it is modulated at the 1022nd harmonic. The pulse width is measured to be approximately 10.5 ps for both the 1012th and 1022nd harmonic as shown in Fig. 5-48.

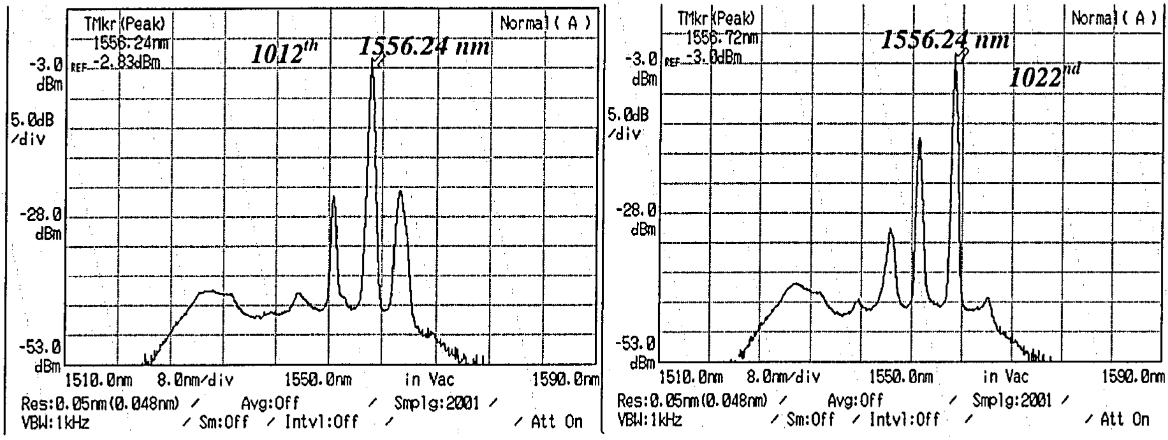

Fig. 5-47: Optical spectrum for a harmonic actively modelocked fiber laser when the modulation frequency is set to the 1012th and 1022nd harmonics, respectively.

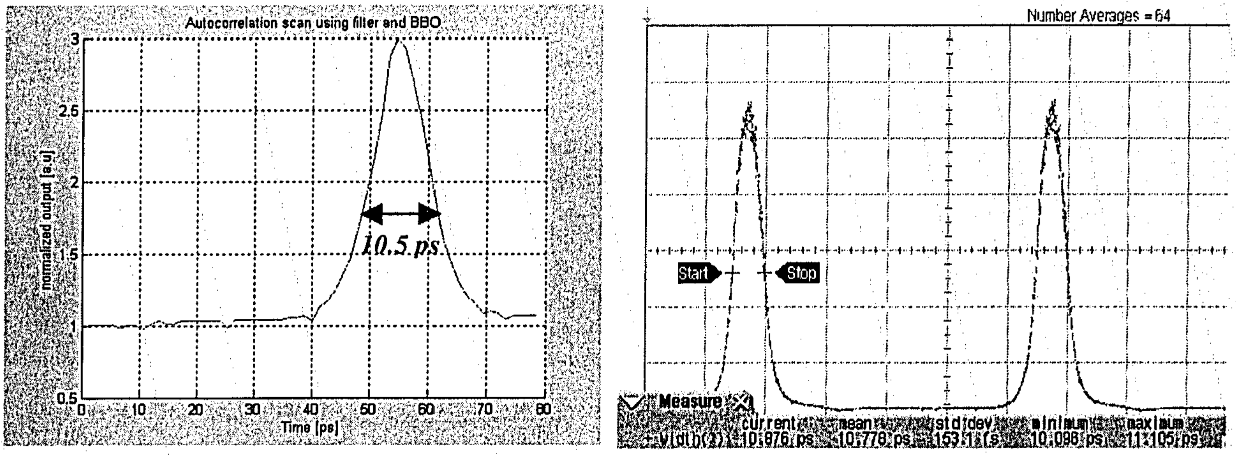

Fig. 5-48: Intensity autocorrelation and oscilloscope trace when the laser is modulated at the 1012th harmonic. The pulse width is approximately 10.5 ps.

After amplifying the laser using 5 m of 3M L-Band EDF, pulse splitting was observed as shown in Fig. 5-49. This is an indication that the laser output contained two or more synchronous pulse trains with different wavelengths. This confirms what is indicated by the optical spectrum shown in Fig. 5-47. Li and Chan [87] reported similar results for an actively modelocked fiber laser of this type, whose output was propagated through a length of highly dispersive fiber.

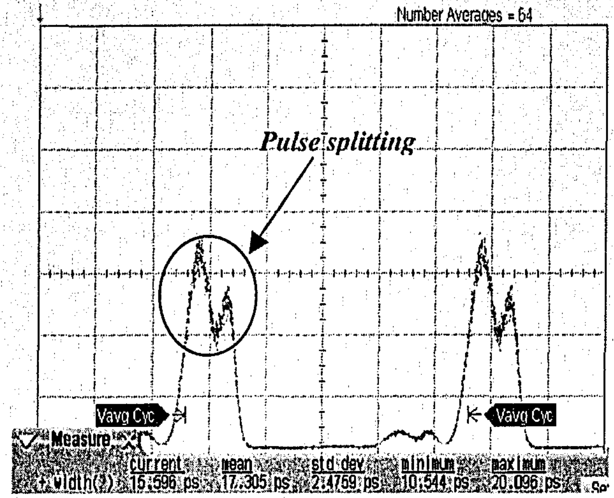

Fig. 5-49: Optical pulses after amplification for the laser modelocked at the 1012th harmonic

As mentioned earlier, single wavelength operation could not be obtained by simply changing the modulation frequency. To obtain single wavelength tunable operation, a JDS tunable bandpass filter (TB1500B) was inserted in the cavity. The optical spectrum and oscilloscope trace are shown in Fig. 5-50. The autocorrelation trace is shown in Fig. 5-51.

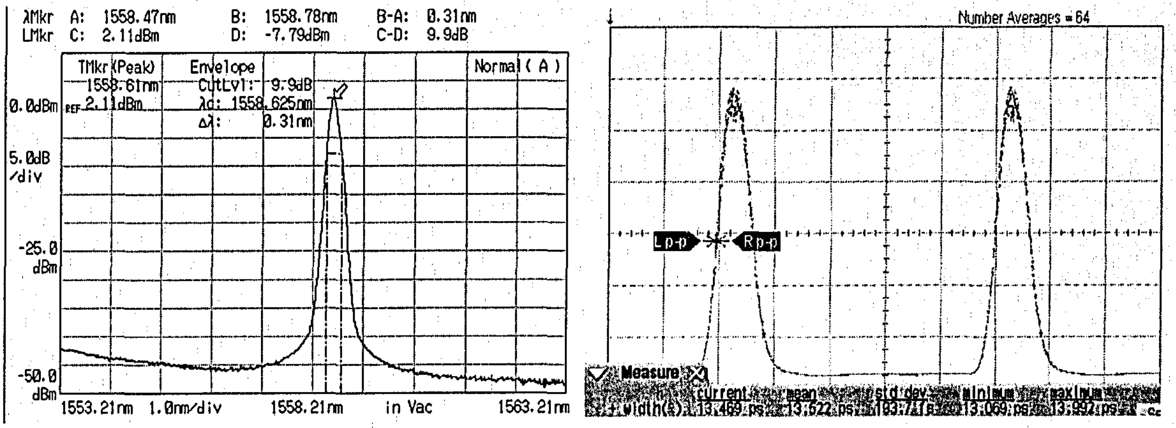

Fig. 5-50: Optical spectrum and oscilloscope trace for single wavelength operation and modulation at the1097th harmonic.

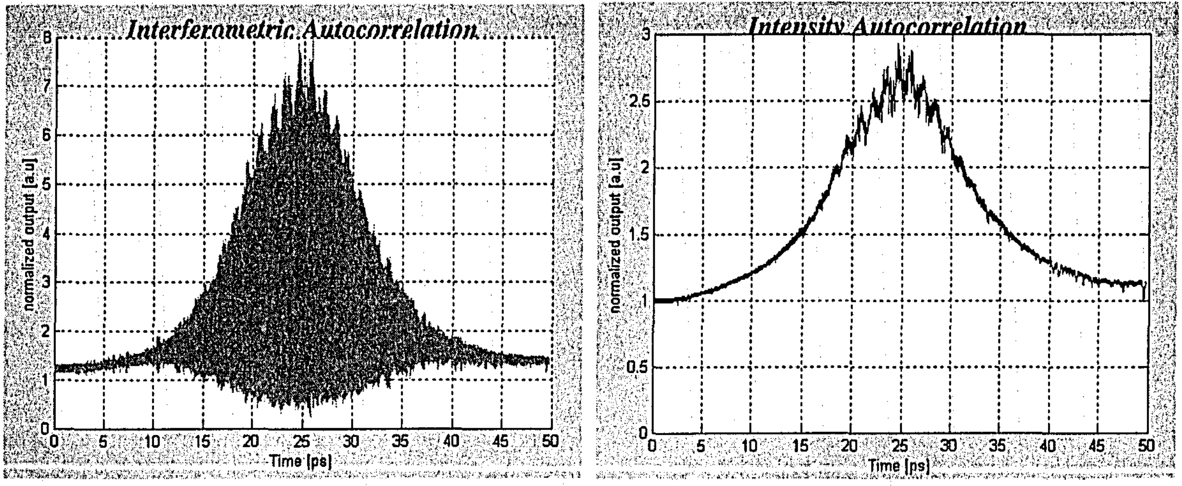

Fig. 5-51: Interferometric and Intensity autocorrelation for single wavelength operation. Pulse width is approximately 13 ps.

If a Gaussian pulse shape is assumed, the measured pulse width is approximately 13 ps. Using this pulse width and the spectral bandwidth of 0.31nm (Fig. 5-50), the time-bandwidth product is calculated to be approximately 0.503, which is very close to the ideal value of 0.441[64]. This reveals that the pulses are almost transform limited. It should be noted that this is the pulse width after propagating through 5m of SMF28 (chirp compensation) at the output of the laser. The chirp was further assessed by using the analysis technique discussed in Section 4.4.3. As can be seen from Fig. 5-52, comparing the two autocorrelation traces reveals very little difference. This provides evidence that the pulses were almost transform limited.

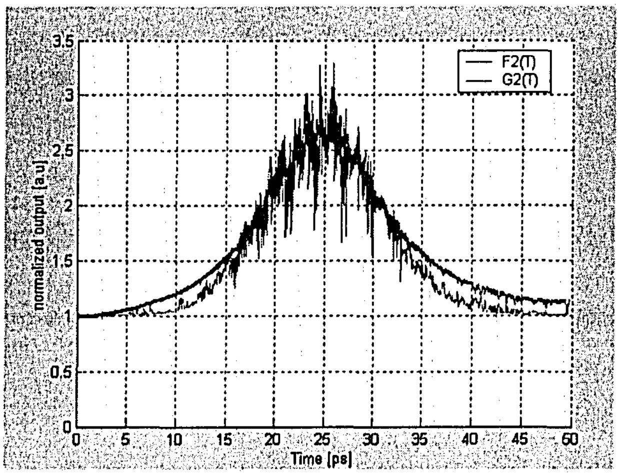

Fig. 5-52: Comparing filtered autocorrelation traces to test for chirp. (Refer to Section 4.4.3 for details).

The RF spectrum of the output after detection using a high-speed detector is shown in Fig. 5-53. Notice that only the 9.97 GHz component is visible in the 1.5 GHz span, which indicates uniform harmonic modelocking [88]. This figure also shows that pulse-to-pulse fluctuations, which should appear as noise components at harmonics of the fundamental frequency (9.09 MHz), were not observed. The laser remained stable over long periods of time. While the wavelength tended to drift, the pulse and spectral shape remained constant.

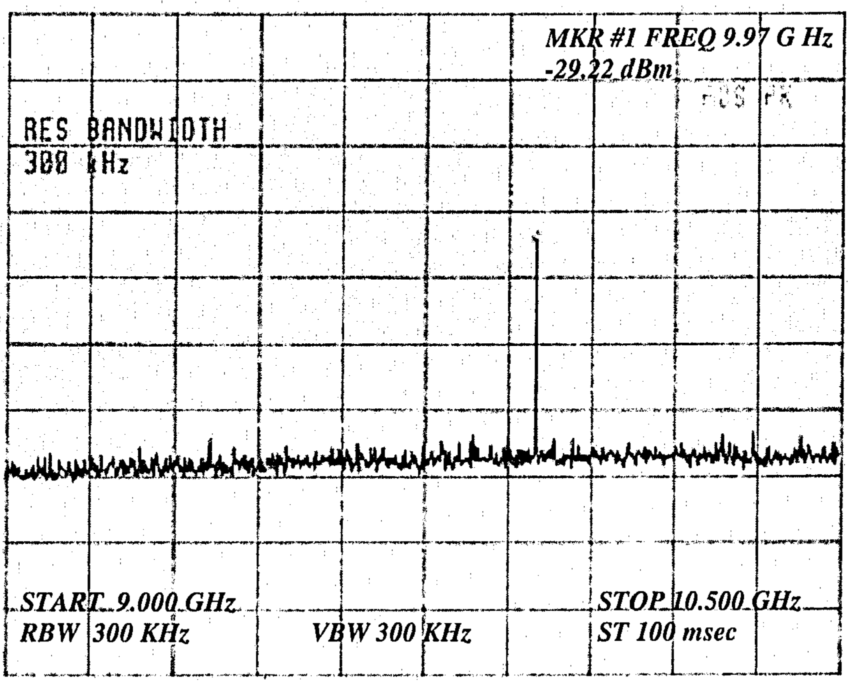

Fig. 5-53: Rf spectrum at 9.97 GHz on a 1.5 GHz span. The vertical scale is 10 dB/div

6 Conclusion

6.1 Summary of Results

This thesis presented the study of two stretched additive pulse modelocked EDF lasers, as well as an actively modelocked fiber laser. It also presented the development and test of an interferometric autocorrelator. The following are highlights of the achievements of this thesis with details to follow.

1. Various modes of pulsed operation were verified for both types of passively modelocked fiber laser investigated. Possible bound solitons, bunches of solitons and noise-like pulses were observed. The bound and bunched solitons were found to have discrete fixed soliton separation. The noise-like pulses were stable and found to have broad spectra.
2. A wavelength tunable, actively modelocked fiber laser that produced nearly transform limited pulses of ps duration was designed and implemented. Dispersion tuning of the center wavelength was successfully demonstrated under harmonic modelocking operation with an extinction of greater than 29 dB observed in the RF spectrum (Fig. 5-53).
3. An interferometric autocorrelator was designed and implemented. It was used to characterize the nature, duration, and chirp of the pulses emitted by the passively and actively modelocked lasers mentioned above.

With regards to the autocorrelator, various considerations for design and implementation were discussed. A silicon APD was characterized in order to determine its suitability for use as a two-photon absorber. From the characterization experiment it was found that the APD response was dominated by linear absorption and, as such, it was unsuitable as a two-photon absorber. A BBO second harmonic nonlinear crystal was subsequently tested and found to be more suitable.

The autocorrelator was used to measure pulses from the actively modelocked laser discussed in Chapter 5, and it was found to produce results that were in reasonable agreement with simulations, and with results measured by a sampling oscilloscope (see

Section 4.4.3). Furthermore, the autocorrelator could also be used in conjunction with filters to qualitatively investigate the chirp of a pulse.

For the passively modelocked fiber lasers, two cavity configurations were investigated; the stretched pulse ring cavity and a figure eight NOLM cavity. The main modes of pulsed operation were investigated for both cavities and it was found that the only stable mode of operation was the noise-like mode.

Although several experiments were performed, a short pulse mode of operation was not obtained for either of the passively modelocked fiber laser cavities. Long cavities "with little or no dispersion management" reportedly have a tendency to operate in the noise-like regime [57]. Hence in each experiment the cavities were kept relatively short and a concerted effort was made to balance the dispersion. Unfortunately, since the dispersion of the EDF was not known, it was difficult to conclude that the dispersion balance criterion was met. This, coupled with the fact that the birefringence of the EDF was unknown, made the design of the laser cavity extremely challenging. Another obstacle was the alignment of the fiber axes. There is no published work that outlines how to experimentally align these lasers, but there are several theoretical studies that indicate the importance of the alignment of the fiber axes and the input state of polarization [71],[74],[80].

For the actively modelocked laser, a dispersion-tuned harmonically modelocked cavity was selected. Multi-wavelength tunability was observed for varying modulation frequency. However, single-wavelength tunability was only observed after employing a tunable filter in the cavity. This could be attributed to the fact that the dispersion in the cavity was excessive. Li and Chan [87] suggest that in order to obtain single wavelength tunability at higher repetition rates, the cavity dispersion should be reduced. The laser was found to produce stable picosecond pulses in both the single and multiple-wavelength regimes.

Wavelength tunable pulsed sources can find applications in areas such as remote sensing, (with separate absorption measurements on two closely spaced wavelengths), or for the characterization of optical components in WDM systems.

Although it was hoped that a short pulse mode of operation would be obtained from the passively modelocked fiber lasers, the noise-like mode is not without its advantages. The spectrum and pulse train in this mode of operation were extremely stable over time. Adjusting the parameters of the cavity allowed control over some properties of noise-like pulses, such as average power and pulse duration. Lasers of this type could have applications in areas where low-coherence sources with board spectra are needed. Noise-like pulses have actually been used for interrogating an array of fiber gratings [83].

6.2 Future Research

The work discussed in this thesis is an essential stepping-stone in developing a modelocked femtosecond fiber ring laser system. However, there are many other experiments that need to be performed before a femtosecond source can be realized. This section discusses some suggestions for future work.

1. Before a stretched pulse modelocked fiber laser can be realized, the fiber birefringence and the dispersion of the EDF should be known. As discussed in Chapter 5, these parameters are essential in designing the laser cavity. There are experimental procedures for measuring these parameters, but they are not trivial. Sahsah *et al.* [89] and Dhliwayo *et al.* [90] outline two different procedures for measuring the birefringence. While Tiihonen [91] outlines a procedure for measuring the GVD of EDF.
2. Another important factor in obtaining short pulses is the alignment of the fiber axes, as discussed in Chapter 5. An experimental procedure for doing this might enable a step-by-step approach to obtaining modelocked operation. This would be an important contribution to the field of modelocked fiber lasers, as it would complement the theory that has been published previously in the literature.
3. It would be interesting to source and test a semiconductor saturable absorber, to investigate if reliable modelocking could be simplified in that case. The insertion of a semiconductor saturable absorber in the linear loop of the figure-8 laser, discussed in Chapter 3 and 5, should help in initiating self-starting to obtain modelocked operation [82].

4. The output chirp must be characterized and then externally compensated. Preliminary work towards this goal was briefly discussed in Chapters 4 and 5. When this task is completed, other optimizations such as external pulse compression and amplifications can be investigated. Chirped pulse amplification is a simple and effective means of amplifying the output of a laser.
5. Once the dispersion of the fibers is known with certainty, the dispersion characteristics of the laser could be investigated further. For example, the effect of total dispersion (both net negative and positive) on pulse width and spectral width could be investigated

Many additions to this list are possible, as fiber lasers are emerging as a practical alternative to bulk solid state lasers. The research that is presently being performed in this area is extensive, covering areas from nonlinearity management [57] to supercontiuum generation [61]. It is envisioned that in the near future, the performance of fiber lasers will surpass bulk solid-state lasers in many respects, as the research in this area continues to expand.

References

[1] T. H. Maiman, *Nature* (London) Vol. 187, pp. 493, 1960.

[2] W. M. Steen, *Laser Materials processing*, 2nd ed. 1998.

[3] J.E. Geusic, H. M Marcos & L. G Van Uitert, *Applied Physics Letters*, Vol. 4, pp. 182, 1964.

[4] R. W. Hellwarth, *Bull. Am. Phys. Soc.* Vol. 6, pp. 414, 1961.

[5] L. E. Hargrove, R. L. Fork, and M. A. Pollack, *Applied Physics Letters*, Vol. 5, pp. 4, 1964.

[6] H. W. Mocker, and R. J. Collins, *Applied Physics Letters,* Vol. 7, pp. 270, 1965.

[7] A. J. Demaria, D. A. Stetser, and H. Heinan, *Applied Physics Lett*ers, Vol. 8, pp. 174, 1966.

[8] C. V. Shank, and E. P. Ippen, *Applied Physics Letters*, Vol. 24, pp. 373, 1974.

[9] R.L. Fork, B.I. Greene, and C.V. Shank, *Applied Physics Letters*, Vol. 38, pp. 671, 1981.

[10] R.L. Fork, O. E. Martinez, and J.P. Gordon, *Optics Lett*ers, Vol. 9, pp. 150, 1984.

[11] J. A. Valdmanis, R. L. Fork, and J. P. Gordon, *Optics Lett*ers, Vol. 10, pp. 131, 1985.

[12] R. L. Fork, C. H. Brito Cruz, P. C. Becker, and C.V. Shank, *Optics Letters*, Vol. 12, pp. 483, 1987.

[13] L.F. Mollenauer, and R. H. Stolen, *Optics Lett*ers, Vol. 9, pp. 13, 1984.

[14] J. Mark, L.Y. Liu, K. L. Hall, H. A. Haus, and E.P. Ippen, *Optics Lett*ers, Vol. 14, pp. 48, 1989.

[15] E.P. Ippen, H. A. Haus, and L.Y. Liu, *Journal of the Optical Society of America. B. Optical Physics*, Vol. 6, pp. 1736, 1989.

[16] P.F. Moulton, *Journal of the Optical Society of America. B. Optical Physics*, Vol. 3, pp. 125, 1986.

[17] D.E. Spence, P.N. Kean, and W. Sibbett, *Optics Lett*ers, Vol. 16, pp. 42, 1991.

[18] I. D. Jung, F.X. Kartner, N. Matuschek, D.H. Sutter, F.M. Genud, G. Zhang, U.Keller, V. Scheuer, M. Tilsch, and T. Tschudi, *Optics Lett*ers, Vol. 22, pp. 1009, 1997.

[19] R.J. Mears, L. Reekie, S. B. Poole, and D. N. Payne, *Electronics Letters*. Vol. 22, pp. 159, 1986.

[20] E. Desurvire, "*Erbium Doped Fiber Amplifiers*", John Wiley & Sons, Inc., Hoboken, New Jersey, 2002.

[21] H. A. Haus, *Journal of Selected Topics in Quantum Electronics*, Vol. 6, pp. 1173, 2000.

[22] K. Tamura, E. P. Ippen, and H. A. Haus, *Applied Physics Letters,* Vol. 67, pp. 158, 1995.

[23] D. McMorrow, W.T. Lotshaw, and G.A. Kenny-Wallace, *IEEE Journal of Quantum Electronics*, Vol. 24, No. 2, pp. 443-454, 1988.

[24] S. Kinoshita, H. Ozawa, Y. Kanematsu, I. Tanaka, N. Sugimoto, and S. Fujiwara , *Review of Scientific Instruments*, Vol. 71, No.9, pp. 3317-3322, 2000.

[25] C. Florea, and K. A. Winick, *Journal of Lightwave Technology*, Vol.21, No. 1, pp. 246-252, 2003.

[26] K. Kawamura, T. Ogawa, N. Sarukura, M. Hirano, and H. Hosono, *Applied Physics B: Laser Optics*, Vol. 71, No. 1, pp 119-121, 2000.

[27] K. Kawamura, N. Sarukura, and M. Hirano, *Applied physics letters*, Vol. 78, No. 8, pp 1038-1040, 2001.

[28] K.Hirao, and K. Muira, *Journal of Non-Crystalline Solids*, Vol. 239, pp. 91-95, 1998.

[29] M. Asobe, T.Kanamori, and K. Kudodera, *IEEE Journal of Quantum Electronics*, Vol. 29, No. 8, pp. 2325-2333, 1993.

[30] B.J. Eggleton, R.E. slusher, J.B. Judkins, J.B. Stark, and A.M. Vengsarkar, *Optics Letters*, Vol. 22, No. 12, pp. 883-885,1997.

[31] H.M. Keller, S. Pereira, and J.E. Sipe, *Optics Communications*, Vol. 170, pp. 35-40, 1999.

[32] M. Asobe, T. Ohara, I. Yokohama, and T. Kaino, *Electronics Letters,* Vol. 32, pp. 1396-1399, 1996

[33] B. Mikulla, L. Leng, S. Sears, B.C. Collings, M. Arend, and K. Bergman, *IEEE Photonics Technology Letters*, Vol. 11, No. 4, pp 418-420, 1999.

[34] G. Keiser, "*Optical Fiber Communications*", Third Edition, McGraw Hill, 2000.

[35] J.T. Verdeyen, "*Laser Electronics*", Third Edition, Prentice Hall, 1995.

[36] P.R. Morkel, G. Cowle, and D.N. Payne, *Electronics Letters,* Vol. 26, No. 10, pp. 632-634, 1990.

[37] A. Ghatak, and K. Thyagarajan, "*Introduction to Fiber Optics*", Cambridge University Press, 2000.

[38] G.P. Agrawal, "*Nonlinear Fiber Optics*", Second Edition, Academic Press, 1995.

[39] B.E.A. Saleh, and M.C. Teich, "*Fundamentals of Photonics*", Wiley-Interscience, 1991.

[40] I.N. Duling III, "*Compact sources of Ultrashort Pulses*", Cambridge University Press, Ch. 5, 1995.

[41] R.W. Boyd, "*Nonlinear Optics*", Academic Press, 1992.

[42] A.E. Siegman, and D.J. Kuizenga, *IEEE Journal of Quantum Electronics*, Vol. QE-6, No.12, pp. 803-808, 1970.

[43] H.A. Haus, *Journal of Applied Physics,* Vol. 46, No. 7, pp. 3049-3058, 1975.

[44] H.A. Haus, *IEEE Journal of Quantum Electronics*. Vol. QE-11, No. 9, pp. 736-746, 1975.

[45] M.Zirngibl, L.W. Stulz, J. Stone, J. Hugi, D. DiGiovanni, and P.B. Hansen, *Electronics Letters*, Vol. 27, No. 19, pp.1734-1732, 1991.

[46] E.A. De Souza, C.E. Soccolich, W. Pleibel, R.H. Simpson, and D.J. DiGiovanni, *Electronics Letters*, Vo. 29, No. 5, pp. 447-449, 1993.

[47] D.J. Richardson, R.I. Laming, D.N. Payne, M.W. Phillips, and V. J. Matsas, *Electronics Letters*, Vol. 27, No. 9, pp. 730-732, 1991.

[48] J. Mark, L. Y. Liu, K.L. Hall, H.A. Haus, and E.P. Ippen, *Optics Letters,* Vol.14, No. 1, pp. 48-50, 1989.

[49] D. Meshulach, Y. Barad, and Y. Silberberg, *Journal of the Optical Society of America B. Optical Phys*ics, Vol. 14, No. 8, pp. 2122-2125, 1997.

[50] G. Shaulov, "Modeling of mode-locked fiber lasers", PHD Thesis, Rensselaer Polytechnic Institute, Troy New York, 1998.

[51] K.Tamura, C.R. Doerr, L.E. Nelson, E.P. Ippen, and H.A. Haus, *Optics Letters,* Vol. 19, pp. 46-48, 1994.

[52] K.Tamura, J. Jocobson, E.P. Ippen, H.A. Haus, and J.G.Fujimoto, *Optics Letters,* Vol. 18, pp. 220-223, 1993.

[53] L.E. Nelson, D.J. Jones, K. Tamura, H.A. Haus, and E.P. Ippen, *Applied Physics B,* Vol. 65, pp. 277-294, 1997.

[54] D.D. Clegg, R. DeCorby, C. Haugen, and V. Hughes, "Miniature 1550 nm autocorrelator-01", *TRLabs, Internal Report*, 2002.

[55] D.T. Reid and W. Sibbett, *Engineering and Lab Notes, Applied Optics*, Vol. 37, No. 34, pp. 8142, 1998.

[56] C. Xu, J.M. Roth, W.H. Knox, and K. Bergman, *Electronics Letters,* Vol. 38, No. 2, pp. 86-88, 2002.

[57] F.O. Ilday and F. W. Wise, *Journal of the Optical Society of America B. Optical Phys*ics, Vol. 19, No. 3, pp. 470-476, 2002.

[58] K.S. Abedin, J.T. Gopinath, L.A. Jiang, M.E. Grein, H.A. Haus, and E.P. Ippen, *Optics Letters,* Vol. 27, No. 20, pp. 1758-1760, 2002.

[59] K. Tamura, E.P. Ippen, H.A. Haus, and L.E. Nelson, *Optics Letters,* Vol. 18, No. 13, pp. 1080-1082, 1993.

[60] G.P. Agrawal, "*Applications in Nonlinear Fiber Optics*" Academic press, 2001.

[61] J.W. Nicholson, A.D. Yablon, P.S. Westbrook, K.S.Feder, and M.F.Yan, *Optics Express*, Vol. 12, No. 13, pp. 3025-3033, 2004.

[62] K. Kikuchi, *Electronics Letters*, Vol. 34, No.1, pp.123-125, 1998.

[63] C. Rulliere (Ed.), " *Femtosecond Laser Pulses*", Springer, New York, 1998.

[64] J.C. Diels, and W. Rudolph, " *Ultrashort Laser Pulse Phenomena*", Academic Press, 1996.

[65] M.E. Fermann, F. Haberl, M. Hofer, and H. Hochreiter, *Optics Letters*, Vol. 15, No. 13, pp. 752-754, 1990.

[66] L.E. Nelson, D.J. Jones, K. Tamura, H.A. Haus, and E.P. Ippen, *Applied Physics B*, Vol. 65, pp. 277-294, 1997.

[67] H.A. Haus, E.P. Ippen, and K. Tamura, *Journal of Quantum Electronics*, Vol. 30, No. 1, pp. 220-208, 1994.

[68] A.B. Grudinin, S. Gray, *Journal of the Optical Society of America. B. Optical Phys*ics, Vol. 14, No. 1, pp. 144-154, 1997.

[69] H.A. Haus, K. Tamura, L.E. Nelson, and E.P. Ippen, *Journal of Quantum Electronics*, Vol. 31, No. 3, pp. 591-598, 1995.

[70] E.A. Kuzin, J.A. Andrade-Lucio, B.Ibarra-Escamilla, R.Rojas-Laguna, and J.Sanchez-Mondragon, *Optics Communication*, Vol. 144, pp. 60-64, 1997.

[71] I.N. Duling, III, *Electronics Letters*, Vol. 27, No. 6, pp. 544-545, 1991.

[72] A. Yariv, "*Quantum Electronics*", John Wiley and Sons, 3rd edition, 1989.

[73] Y.D. Gong, P. Shum, D.Y. Tang, C.LU, X. Guo, V. Paulose, W.S. Man, and H.Y.Tam., *Optics and Laser Technology*, Vol. 36, Pg. 299-307, 2004.

[74] C.W. Chang, and S. Chi, *Journal of Modern Optics*, Vol. 46, No. 9, Pg. 1431-1442, 1999.

[75] M. Horowitz, Y. Barad, and Y. Silberberg, *Optics Letters*, Vol. 22, No.11, Pg. 799-801, 1997.

[76] M. Horowitz, and Y. Silberberg, *IEEE Photonics Technology Letters*, Vol. 10, No.10, Pg. 1389-1391, 1998.

[77] Ph. Grelu, J. Beal, and J. M. Soto-Crespo, *Optics Express*, Vol. 11, No. 18, Pg. 2238-2242, 2003.

[78] D.Y. Tang, W.S. Man, H.Y. Tan, and P.D. Drummond, *Physical Review A*, Vol. 64, No. 033814, Pg. 1-3, 2001.

[79] Ph. Grelu, F. Belhache, F. Gutty, and J.M. Soto-Crespo, *Optics Letters*, Vol. 27, No. 11, Pg. 966-968, 2002.

[80] M. Salhi, H. Leblond, and F. Sanchez, *Physical Review A*, Vol. 68, No.033815, Pg. 1-7, 2003.

[81] S. Wu, J. Strait, R.L. Fork, and T.F. Morse, *Optics Letters*, Vol. 18, No. 17, Pg. 1444-1446, 1993.

[82] F.O. Ilday, F. Wise, and T. Sosnowski, *Optics Letters*, Vol. 27, No. 17, Pg. 1531-1533, 2002.

[83] M.A. Putnam, M.L. Dennis, I.N. Duling, III, C.G. Askin, and E.J. Friebele, *Optics Letters*, Vol. 23, No.2, Pg. 138-140, 1998.

[84] V.V. Afanazjev, B.A. Malomed, and P.L. Chu, *Physical Review E*, Vol. 56, No. 5, Pg. 6020, 1997.

[85] A.E. Siegman, "*Lasers*", University Science Books, Sausalito, California, 1986.

[86] C.Shu, and Y. Zhao, *IEEE Photonics Technology Letters*, Vol. 10, No. 8, Pg. 1106-1108, 1998.

[87] S. Li, and K.T. Chan, *Applied Physics Letters*, Vol. 72, No. 16, Pg. 1954-1956, 1998.

[88] K. Tamura and M.Nakazawa, *Optics Letters*, Vol. 21, No. 24, Pg. 1984-1986, 1996.

[89] H. Sahsah, S. Djendli, and J. Mohin, *Measurement Science and Technology*, Vol. 11, Pg. N46-N50, 2000.

[90] J. Dhliwayo, A. Zhang, R. Nathoo, *Optical Engineering*, Vol. 42, No, 7, Pg. 1896-1900, 2003.

[91] M. Tiihonen, "Msc. Thesis", Royal Institute of Technology, Sweden, and Hariot Watt University, Scotland, January 2002.

[92] A.D. Kim, J.N. Kutz, and D.J. Muraki, *Journal of Quantum Electronics*, Vol. 36, No. 4, Pg. 465-471, 2000.

[93] J.C. Diels, J.J. Fontaine, I. C. McMichael, and F. Simoni, *Applied Optics*, Vol. 24, No. 9, Pg. 1270-1282, 1985.

Appendix A

A.1. Three level lasing model

As discussed in section 2.1, the generation of light in an EDF can be described using a three level lasing model. Fig. A.1 shows a simplified energy level diagram for such a model. This sections covers the mathematical analysis of this model.

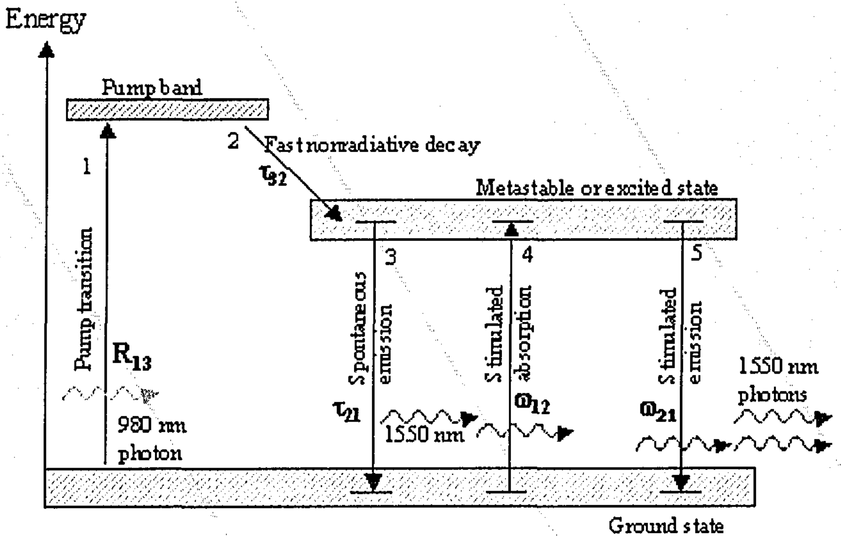

Fig. A-0-1: Simplified energy-level diagram of various transition processes of Er^{3+} ions in silica glass [34]

Mathematically, the total number of erbium ions N_T (ions/cm^3) will be distributed in an amount N_i in each energy level E_i and can be represented by the following rate equations[35]:

$$\frac{\partial N_1}{\partial t} = -(R_{13} + \omega_{12})N_1 + (\omega_{21} + \frac{1}{\tau_{21}})N_2 \qquad \textbf{(A.1.1)}$$

$$\frac{\partial N_2}{\partial t} = \omega_{12}N_1 - (\omega_{21} + \frac{1}{\tau_{21}})N_2 + \frac{N_3}{\tau_{32}} \qquad \textbf{(A.1.2)}$$

$$\frac{\partial N_3}{\partial t} = R_{13}N_1 - \frac{N_3}{\tau_{32}} \qquad \textbf{(A.1.3)}$$

Where:

R_{13} = rate at which the ions are pumped from E_1 to E_3

ω_{12} & ω_{21} = stimulated absorption emission rates, respectively

$1/\tau_{21}$ = rate of spontaneous emission from E_2 to E_1

$1/\tau_{32}$ = rate at which the ions decay from E_3 to E_2

$$R_{13} = \frac{\sigma_p}{h\nu_p} I_p \tag{A.1.4}$$

$$\omega_{12} = \frac{\sigma_a}{h\nu_s} I_s \tag{A.1.5}$$

$$\omega_{21} = \frac{\sigma_e}{h\nu_s} I_s \tag{A.1. 6}$$

σ_p = absorption cross-section (cm^2) at the pump wavelength

σ_a = absorption cross-section (cm^2) at the signal wavelength

σ_e = emission cross-section (cm^2) at the signal wavelength

I_s = signal intensity (W/cm^2)

I_p = pump intensity (W/cm^2)

$h\nu_s$ = energy (J) in a single signal photon

$h\nu_p$ = energy (J) in a single pump photon

If the $1/\tau_{32}$ rate is large relative to the other transition rates, there will be a low density of ions in the N_3 level. In that case, the steady state solutions for N_1 and N_2 can be obtained analytically. The number of ions in these states is critical, as their relative difference influences the expected level of absorption or amplification of 1550 nm light.

$$N_1 \approx N_T \left[\frac{\omega_{21} + \frac{1}{\tau_{21}}}{\omega_{21} + \omega_{12} + R_{13} + \frac{1}{\tau_{21}}} \right] \tag{A.1.7}$$

$$N_2 \approx N_T \left[\frac{\omega_{21} + R_{13}}{\omega_{21} + \omega_{12} + R_{13} + \frac{1}{\tau_{21}}} \right] \quad \textbf{(A.1.8)}$$

A.2. Characteristics of light pulses

Light propagates in the form of waves. In free space, light waves travel with a speed *c*. In a medium with refractive index n, light waves travel with a reduced phase velocity of *c/n*. Consider the monochromatic plane wave whose complex representation of the electric field is given by [63]:

$$E(t) = \mathrm{Re}(E_0 e^{(i\omega_0 t)}) \quad \textbf{(A.2.1)}$$

The time representation of the field is a cosine function that extends over all time. An optical pulse is a wave of finite duration; a mathematical representation of a light pulse can be constructed by multiplying (A.2.1) by an envelope function. Multiplying by a Gaussian function forms a Gaussian pulse, represented by:

$$E(t) = \mathrm{Re}(E_0 e^{(-(t/\tau_G)^2 + i\omega_0 t)}) \quad \textbf{(A.2.2)}$$

where τ_G is the shape factor of the Gaussian envelope and is related to the pulse duration (FWHM) τ_p by the following relation:

$$\tau_G = \tau_p / \sqrt{2 \ln 2} \quad \textbf{(A.2.3)}$$

The pulse duration or pulse width is defined as the full width at half maximum (FWHM) of the intensity profile and the spectral width $\Delta\omega_p$ as the FWHM of the spectral intensity. The temporal and spectral characteristics of the field are related to each other through Fourier transforms; hence the spectral width or bandwidth and pulse width cannot vary independently of each other. There is a minimum duration-bandwidth product [64]:

$$\Delta\omega_p\tau_p \geq 2\pi c_B \tag{A.2.4}$$

C_B is a numerical constant that varies depending on the pulse shape. For a Gaussian pulse, C_B is 0.441. The equality holds for pulses without frequency modulation (unchirped), which are called "bandwidth limited", or "Fourier or transform limited" pulses. Such pulses exhibit the shortest possible duration at a given spectral width. If there is a frequency variation across the pulse, its spectrum will contain additional spectral components and the simple equality given in (A.2.4) cannot be used. Rather a modified version of (A.2.4) that takes chirp into account must be used. Refer to [64] for more details.

A.3. Polarization of light

Many effects in optics depend on the management or manipulation of the polarization of light. For an x-polarized wave propagating along the z-direction, the electric field is confined along the x-coordinate. The electric field can be written in the form:

$$E = \hat{x} E_0 \cos(\omega t - kz + \theta) \tag{A.3.1}$$

where ω is the angular frequency, θ is the phase shift and k is the propagation constant. In a dielectric medium, k is given by:

$$k = \frac{\omega n}{c} \tag{A.3.2}$$

Now consider the superposition of two plane waves of equal amplitude, one polarized in the x-direction and the other in the y-direction, with a phase difference of $\pi/2$ between them.

$$E_1 = E_0 \hat{x} \cos(\omega t - kz) \tag{A.3.3}$$

$$E_2 = E_0 \hat{y} \cos(\omega t - kz - \pi/2) \tag{A.3.4}$$

The resultant electric field would be:

$$E = E_0[\hat{x}\cos(\omega t - kz) + \hat{y}\sin(\omega t - kz) \tag{A.3.5}$$

which describes a right circularly polarized (RCP) wave (Fig. A.2)

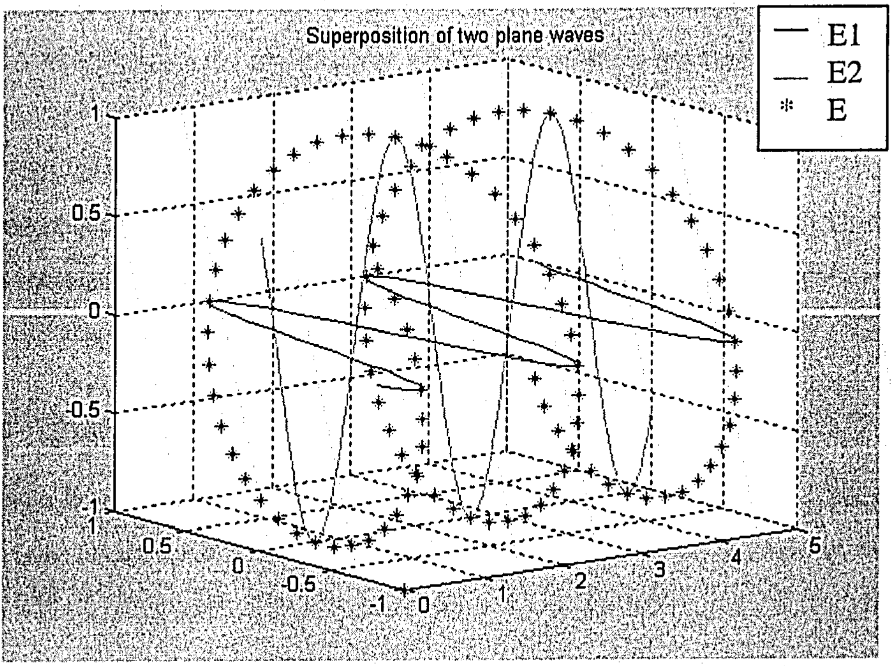

Fig. A-2: The superposition of two plane waves producing a circularly polarized wave. The blue represents equation A.3.3, the green represents equation A.3.4 and the red represents equation A.3.5.

In general, the superposition of two waves with:

$$E = E_0\hat{x}\cos(\omega t - kz) \text{ and } E = E_0\hat{y}\cos(\omega t - kz - \phi) \tag{A.3.6}$$

will represent an elliptically polarized wave. Fig. A.3 shows two different elliptically polarized waves. Fig.A-3(a) represents a left elliptically polarized and Fig.A-3(b) represents a right elliptically polarized wave.

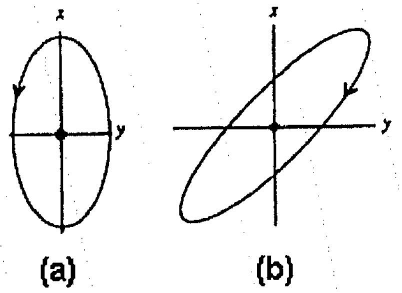

Fig. A-3: Two different elliptical states of polarization represented by equation (2.4.6) with (a) E_1 = 1/2E_0 and $\phi = -\pi/2$, and (b) $E_1 = E_0$ and $\phi = \pi/3$ [37].

A.4. Sagnac interferometer

A fiber Sagnac interferometer consists of a 2X2 coupler with two output ports connected by a length of optical fiber. Such a setup is shown in Fig. A.4. There are two main types of Sagnac interferometer; namely the nonlinear-optical loop mirror (NOLM) and the nonlinear-amplifying loop mirror (NALM). This section discusses the operation of these interferometers.

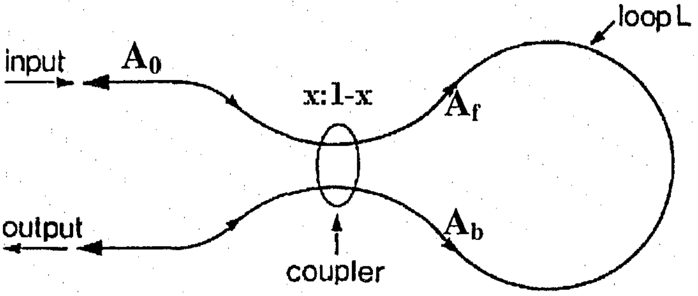

Fig. A-4: A fiber Sagnac interferometer, A_0=input amplitude, A_f= amplitude of forward propagating field, A_b= amplitude of backwards propagating field.

An input field is split into two counterpropagating fields at the coupler. If the coupler splitting ratio is x:1-x, then a fraction, x ,of the input power P_0 travels through the fiber loop in the clockwise direction, and the remaining fraction, 1-x, propagates in the counterclockwise direction through the loop.

To analyze the light propagation in the loop, the amplitude of the optical field is used instead of power. The amplitude is related to power via $A_0 = \sqrt{P_0}$. The powers of the forward and backward propagating fields are $P_f = xP_0$ and $P_b = (1-x)P_0$ respectively. The corresponding field amplitudes are given by [60]:

$$A_f = \sqrt{P_f} = \sqrt{xP_0} = \sqrt{x}A_0 \tag{A.4.1}$$

$$A_b = \sqrt{-P_b} = \sqrt{-(1-x)P_0} = i\sqrt{1-x}A_0 \tag{A.4.2}$$

Note that the backwards propagating field experiences a π/2 phase shift at the coupler when it crosses into the sagnac loop.

The output of the interferometer is in the form of a reflected and transmitted field. The reflected field exits via the input port that delivered the initial input power while the transmitted field exits via the other input port. The amplitude of these fields can be easily calculated if nonlinear effects are ignored and the splitting ratio of the coupler remains constant. The amplitude of the reflected field is given by:

$$\begin{aligned} A_r &= \sqrt{x}A_b + i\sqrt{1-x}A_f \\ A_r &= 2i\sqrt{x(1-x)}A_0 \end{aligned} \tag{A.4.3}$$

and the amplitude of the transmitted field is given by:

$$\begin{aligned} A_t &= \sqrt{x}A_f + i\sqrt{1-x}A_b \\ A_t &= (2x-1)A_0 \end{aligned} \tag{A.4.3}$$

Notice that the transmitted field retains the same phase as the input field, while the reflected beam is out of phase by $\pi/2$. These equations govern the linear behavior of the Sagnac interferometer. In reality, nonlinear effects, namely self phase modulation (SPM) and cross phase modulation (XPM) must be taken into consideration in the analysis. The forward and backward-propagating fields reaching the coupler at the end of the fiber loop become:

$$\begin{aligned} A_f' &= A_f \exp[i\phi_0 + i\gamma(|A_f|^2 + 2|A_b|^2)L] \\ A_b' &= A_b \exp[i\phi_0 + i\gamma(|A_b|^2 + 2|A_f|^2)L] \end{aligned} \tag{A.4.4}$$

where L is the length of the fiber loop, ϕ_0 is the linear phase shift due to due to dispersion, given by:

$$\phi_0 = \beta L = \frac{\omega n}{c} L \tag{A.4.5}$$

and $\gamma(|A_b|^2 + 2|A_f|^2)$ is the nonlinear phase shift due to XPM and SPM. The magnitude of the XPM-induced phase shift is twice that of the SPM-induced phase shift.

$$\gamma = \frac{2\pi n_2}{\lambda A_{eff}} \tag{A.4.6}$$

where n_2 is the nonlinear index coefficient, L is the effective propagation distance, λ is the wavelength of the light, ω is the angular frequency, n is the linear refractive index, *c* is the speed of light and A_{eff} is the effective fiber core area.

The reflected and transmitted fields exiting the loop are:

$$\begin{aligned} A_r &= \sqrt{x}A_b' + i\sqrt{1-x}A_f' \\ A_t &= \sqrt{x}A_f' + i\sqrt{1-x}A_b' \end{aligned} \tag{A.4.7}$$

and the transmittivity can be defined as:

$$\begin{aligned} T &\equiv \frac{|A_t|^2}{|A_0|^2} \\ T &= 1-2x(1-x)\{1+\cos[(1-2x)\gamma|A_0|^2 L]\} \end{aligned} \tag{A.4.8}$$

If $x = 0.5$, the transmittivity is zero and the Sagnac interferometer acts as a perfect mirror, reflecting 100% of the input radiation. For $x \neq 0.5$, the transmittivity becomes a function of the input power and reaches 100% whenever the following relation is satisfied:

$$(1-2x)\gamma|A_0|^2 L = (2m-1)\pi \tag{A.4.9}$$

where *m* is an integer.

A Sagnac interferometer that operates in this fashion by taking advantage of fiber nonlinearity is called a nonlinear-optical loop mirror (NOLM). If an amplifier is placed inside the NOLM, for instance, near one end of the loop as shown in Fig.A-5 and a 0.5:0.5 coupler is used, this modified NOLM is called a nonlinear-amplifying loop mirror (NALM). The asymmetric positioning of the amplifier leads to a different phase shift for the forward-propagating pulse than for the backward-propagating pulse. The basic operating principles are the same as the NOLM but the analysis changes slightly.

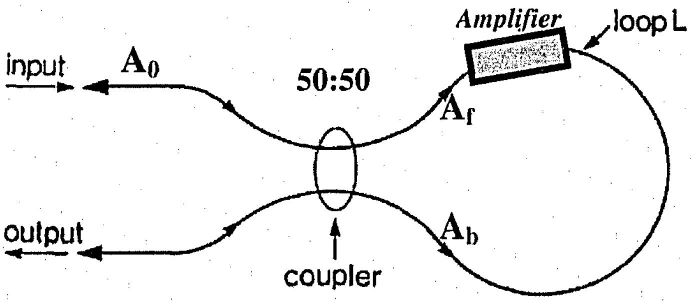

Fig. A-5: Basic parts of a NALM. A_0 is the input signal, A_f is the forward propagating signal and A_b is the backwards-propagating signal. The coupler is a 50:50 coupler.

If it is assumed that the forward propagating wave is amplified by a factor G, then A_f has be to be multiplied by $\sqrt{G}$. Therefore equation (A.2.4) becomes:

$$\begin{aligned} A_f' &= \sqrt{G}A_f \exp[i\phi_0 + i\gamma(|\sqrt{G}A_f|^2 + 2|A_b|^2)L] \\ A_b' &= A_b \exp[i\phi_0 + i\gamma(|A_b|^2 + 2|\sqrt{G}A_f|^2)L] \end{aligned} \quad \textbf{(A.4.10)}$$

and the transmittivity is now given by:

$$T = 1 - 2x(1-x)\{1 + \cos(1-x-Gx)\gamma|A_0|^2 L \quad \textbf{(A.4.11)}$$

The condition for complete transmission is obtained by replacing *(1-2x)* with *(1-x-Gx)* in equation (A.4.9). For $x = 0.5$ and $m = 1$ and noting that $|A_0|^2 = P_0$, complete transmission is obtained when:

$$P_0 = \frac{2\pi}{[(G-1)\gamma L]} \quad \textbf{(A.4.12)}$$

A.5. Dispersion calculations

As discussed in section 2.3, dispersion in a medium results in temporal broadening of a pulse that propagates through the medium. We also saw, in section 3.1, that dispersion balance is essential in the operation of a stretched pulsed laser, hence it is important to calculate the dispersion for each length of fiber used in the laser cavity. This section discusses a few methods for calculating fiber dispersion.

The dispersion coefficient for SMF28 fiber is commonly given on the datasheet in terms of wavelength as D_λ = 17 ps/nm-km. It is however convenient to express this in terms of frequency, using the following relationship[34][39]:

$$D_\nu = \frac{-\lambda_0^2 D_\lambda}{2\pi C_0} \rightarrow [ps^2/km] \quad \textbf{(A.5.1)}$$

where λ_0 is the wavelength and C_0 is the speed of light in vacuum. Using this relationship the dispersion of SMF28 is calculated to be –22 ps^2/km.

The dispersion for EDF fiber is seldom listed on the datasheet and as such must be estimated based on the core radius (a), the numerical aperture (NA) and the cutoff wavelength of the fiber (λ). Using these parameters and the following relationship[37], the dispersion for EDF can be approximated.

$$D_w = \frac{-n_2\Delta}{\lambda}\left[V\frac{d^2(bV)}{dV^2}\right] \rightarrow [ps/(km-nm)] \qquad \textbf{(A.5.2)}$$

where D_w is the waveguide dispersion, n_2 is the index of the cladding, λ is the cutoff wavelength, V is the normalized waveguide parameter, given by $(2\pi/\lambda)aNA$, Δ is defined as $\Delta \equiv (n_1 - n_2)/n_1$, n_1 is the index of the core, and $d^2(bV)/dV^2$ can be found in the plot from [37]. Using this relationship, equation (A.5.1) and the parameters given for the NUFERN EDF555 fiber, the dispersion was estimated to be approximately 12.7 ps^2/km.

Sometimes the dispersion information is given in terms of the slope of the dispersion (S_0) at the zero dispersion wavelength (λ_0). In this case the dispersion can be calculated using the following relationship [34]:

$$D_\lambda = \frac{\lambda S_0}{4}\left[1-\left(\frac{\lambda_0}{\lambda}\right)^4\right] \rightarrow [ps/(km-nm)] \qquad \textbf{(A.5.3)}$$

where λ is the wavelength of interest, λ_0 is the zero dispersion wavelength of the fiber and S_0 is the slope at the zero dispersion wavelength.

A.6. Two-photon absorption (TPA)

If the nonlinear index of refraction (n_2) given in (2.4.2) is a complex number and has a non-zero imaginary part, then this leads to an intensity dependent absorption coefficient. This is called two-photon absorption. This process has been discussed mathematically in most nonlinear optics and quantum electronics books [41],[72]. In this section a brief and simple explanation is given based on quantum electronics.

If we have a semiconductor material with an energy gap of E_g, then a single photon of energy $h\upsilon \geq E_g$, where h is Planck's constant and υ is the frequency of the light, is able to generate a single electron-hole pair and therefore we see a linear absorption in the material (Fig. A-6 (a)). Now suppose the energy of the photon is lower such that $h\upsilon \leq E_g \geq 2h\upsilon$. In this case one photon is not able to promote an electron from the valence band to the conduction band. However, a single electron hole-pair may be created by the instantaneous absorption of two photons (Fig. 6 (b)) if the photons arrive at the same time (and place) on the sample. As illustrated schematically, the absorption takes place by using the energy from the first photon to take the electron to a virtual state and almost simultaneously moving it to the final state by means of a second photon.

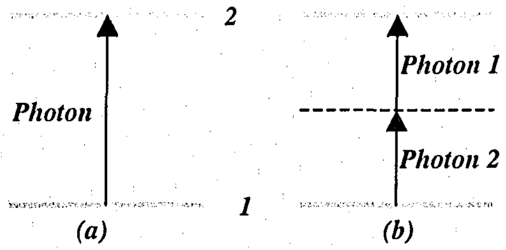

Fig. A-6: The absorption of photons in a two-level system, (a) linear (single-photon) absorption and (b) two-photon absorption.

Since tow photons are required, the rate of absorption scales with the square of the photon arrival rate (i.e. the square of the intensity) The two-photon absorption coefficient (β) gives the change in intensity (I) of a beam as it travels through a medium of length (z).

$$\beta = \frac{1}{I^2}\frac{dI}{dz} \tag{A.6.1}$$

A.7. Autocorrelation calculations

In an autocorrelator, the output from the two-photon absorption or second harmonic process is given by [62]

$$S_2(\tau) = 1 + 2G_2(\tau) + 4\mathrm{Re}[F_1(\tau)\exp(-i\omega_0\tau)] + \mathrm{Re}[F_2(\tau)\exp(-2i\omega_0\tau)] \tag{A.7.1}$$

where τ is the delay, $G_2(\tau)$ is the intensity autocorrelation and is given by: $G_2(\tau) = \langle |E(t)|^2 |E(t-\tau)|^2 \rangle$, where $E(t)$ is the complex amplitude of the signal pulse. $F_1(\tau)$ and $F_2(\tau)$ is given by:

$$F_1(\tau)=\frac{1}{2}\langle(|E(t)|^2+|E(t-\tau)|^2\ E(t)E^*(t-t))\rangle$$
$$F_2(\tau)=\langle E^2(t)E^{*2}(t-\tau)\rangle \tag{A.7.2}$$

The output from the linear absorption process is given by:

$$S_1(\tau)=1+\mathrm{Re}[G_1(\tau)\exp(-i\omega_0\tau)]$$
$$G_1(\tau)=\langle E(t)E^*(t-\tau)\rangle \tag{A.7.3}$$

If both linear and nonlinear detection are simultaneously present, the output from the interferometric autocorrelation is a superposition of $S_1(\tau)$ and $S_2(\tau)$. $G_2(\tau)$ and $F_2(\tau)$ are the quantities of interest. It can be shown that the information on the pulse width is included in $G_2(\tau)$ and the chirp information is contained in $F_2(\tau)$[62].

In summary output from the interferometric autocorrelation scan is given by [62]

$$S(\tau)=S_1(\tau)+S_2(\tau)$$
$$S(\tau)=1+\mathrm{Re}[G_1(\tau)\exp(-i\omega_0\tau)]+2G_2(\tau)+4\mathrm{Re}[(F_1(\tau)\exp(-i\omega_0\tau)]+\mathrm{Re}[F_2(\tau)\exp(-2i\omega_0\tau)] \tag{A.7.4}$$
$$S(\tau)=1+G_1(\tau)\cos(\omega_0\tau)+2G_2(\tau)+4F_1(\tau)\cos(\omega_0\tau)+F_2(\tau)\cos(2\omega_0\tau)$$

The derivation details and simplifications of these equations are as follows:

The linear or first order autocorrelation is given by[93]

$$S_1(\tau)=\frac{\int_{-\infty}^{\infty}|E(t)+E(t-\tau)|^2\,dt}{2\int|E(t)|^2\,dt}$$

$$\textit{where}$$
$$\int|E(t)|^2\,dt=1$$
$$\textit{therefore}:$$
$$S_1(\tau)=\cancelto{1/2}{\frac{\int_{-\infty}^{\infty}|E(t)|^2dt}{2\int_{-\infty}^{\infty}|E(t)|^2dt}}+\frac{2\int_{-\infty}^{\infty}E(t)E(t-\tau)dt}{2\int_{-\infty}^{\infty}|E(t)|^2dt}+\cancelto{1/2}{\frac{\int_{-\infty}^{\infty}|E(t-\tau)|^2dt}{2\int_{-\infty}^{\infty}|E(t)|^2dt}} \tag{A.7.5}$$
$$S_1(\tau)=1+\int_{-\infty}^{\infty}E(t)E(t-\tau)dt$$

Similarly the fringe average or intensity autocorrelation is given by:

$$G_2(\tau)=\frac{\int_{-\infty}^{\infty}|E^2(t)E^2(t-\tau)|dt}{\int_{-\infty}^{\infty}|E^2(t)|^2\,dt} \tag{A.7.6}$$

Or for the assumption of normalized fields:

$$G_2(\tau)=\int_{-\infty}^{\infty}|E^2(t)E^2(t-\tau)|dt \tag{A.7.7}$$

The normalized second order interferometric autocorrelation is given by:

$$S_2(\tau)=\frac{\int_{-\infty}^{\infty}|\{E(t)+E(t-\tau)\}^2|^2\,dt}{2\int_{-\infty}^{\infty}|E^2(\tau)|^2\,dt}$$

$$S_2(\tau)=1+4\int_{-\infty}^{\infty}E^3(t)E(t-\tau)dt+3\int_{-\infty}^{\infty}E^2(t)E^2(t-\tau)dt \tag{A.7.8}$$

$$S_2(\tau)=1+4\int_{-\infty}^{\infty}E^3(t)E(t-\tau)dt+3G_2(\tau)$$

Note for an unchirped pulse $G_2(\tau) = F_2(\tau)$. For a train of ***unchirped*** Gaussian pulses with frequency distribution $F(\Delta\omega)$ around a center frequency ω_0, the first and second order autocorrelation becomes:

$$\begin{aligned} S_1(\tau)&=1+\left\{\int_{-\infty}^{\infty}E(t)E(t-\tau)dt\right\}\cos(\omega_0\tau)\\ S_2(\tau)&=1+2G_2(\tau)\left\{4\int_{-\infty}^{\infty}E^3(t)E(t-\tau)dt\right\}\cos(\omega_0\tau)+G_2(\tau)\cos(2\omega_0\tau)\end{aligned} \tag{A.7.9}$$

A.8. Calculations for BBO crystal.

For the calculations made in this section the following assumptions are made, no pump depletion, negative uniaxial crystal $n_e^{\omega} < n_o^{\omega}$ and class 3m crystal.

The following data was taken from the datasheet for Newlight BBO.

Sellmeier equations: (λ in μm) :

$$n_o^2 = 2.7359 + \frac{0.01878}{(\lambda^2 - 0.01822)} - 0.01354\lambda^2$$
$$n_e^2 = 2.3753 + \frac{0.01224}{(\lambda^2 - 0.01667)} - 0.01516\lambda^2 \quad \textbf{(A.8.1)}$$

Using these yields the following indices for λ = 1.550 μm and λ/2 = 0.775 μm

$$\begin{aligned} n_o^{\omega} &= 1.65 \\ n_0^{2\omega} &= 1.66 \\ n_e^{\omega} &= 1.53 \\ n_e^{2\omega} &= 1.54 \end{aligned} \quad \textbf{(A.8.2)}$$

The nonlinear coefficients are:

$$\begin{aligned} d_{11} &= 5.8 d_{36}(KDP) \\ d_{36}(KDP) &= 0.39 pm/v \\ d_{11} &= 2.262 pm/v \\ d_{31} &= 0.05 d_{11} = 0.01131 pm/v \\ d_{22} &< 0.05 d_{11} < 0.01131 pm/v \end{aligned} \quad \textbf{(A.8.3)}$$

A.8.1. Calculation of crystal length

Assuming a Gaussian beam and confocal focusing, the crystal length can be calculated. It is shown the confocal focusing gives the best conversion efficiency[41] since the interaction length is almost the whole length of the crystal. The maximum conversion is obtained when $L = 2\ Z_0$, where Z_0 is the distance in which the beam cross-sectional area doubles relative to its value at the waist.

$$Z_0 = \frac{\pi n \omega_0^2}{\lambda} \quad \textbf{(A.8.4)}$$

For our setup $\omega_0 = 36$ μm, $n = 1.5$, $\lambda = 1.55$ μm, which leads to **L = 7.8 mm.**

A.8.2. Phase matching

Perfect phase matching requires the $n^{2\omega} = n^{\omega}$. If the two waves are of different types, one extraordinary and the other ordinary, this condition can be satisfied. If $n_e^{2\omega} < n_0^{\omega}$ there exists an angle θ_m for which $n_e^{2\omega} = n_0^{\omega}$. Thus, a fundamental beam at ω launched along θ_m as an ordinary ray, will generate a second harmonic beam along the same axis as an extraordinary ray. For a negative uniaxial crystal, the phase matching angle is defined as:

$$Sin^2(\theta_m) = \frac{(n_0^{\omega})^2 - (n_0^{2\omega})}{(n_e^{2\omega}) - (n_0^{2\omega})} \qquad \textbf{(A.8.5)}$$

For BB0, this angle is calculated to be approximately **20 degrees.**

A.8.3. Efficiency

Assuming a Gaussian beam and perfect phase matching ($n^{\omega} \cong n^{2\omega}$) with no pump depletion, the efficiency of the SHG can be calculated for the optimized length of crystal. $L \cong 2Z_0$.

$$\eta_{2\omega} = \frac{P^{2\omega}}{P^{\omega}} = \frac{2Z\omega_1^2 d^2}{c^2 n_2 n_1^2} \frac{P^{\omega}}{\pi\omega_o^2} L^2 \frac{\sin^2(\Delta KL/2)}{(\Delta KL/2)^2}$$

$$where: \qquad \textbf{(A.8.9)}$$

$$\frac{\sin^2(\Delta KL/2)}{(\Delta KL/2)^2} \cong 1$$

Note: $Z =$ characteristic impedance of free space = 377 Ω.

d = *deff*, the effective nonlinear coefficient which is defined as the direction of the wave vector in a direction specified by spherical coordinated (θ and ϕ), referenced to the crystalline axis.

Typically for type I BBO crystals, the cut is θ = 22.8° and ϕ = 0° and *deff* is defined as:

$$\begin{aligned} d_{eff} &= d_{31}\sin\theta + (d_{11}\cos 3\phi - d_{22}\sin\phi)\cos\theta \\ for\phi &= 0 \\ d_{eff} &= d_{31}\sin\theta + d_{11}\cos\theta \\ d_{eff} &\approx 2.129\,pm/v \end{aligned} \tag{A.8.10}$$

Now if birefringence is taken into account, the θ is replaced by (θ-ρ), where ρ is the birefringence walk-off angle which is approximately 3.2° for BBO. The effective nonlinear coefficient becomes 2.08 pm/v.

Using these parameters and the length calculated above, the efficiency is found to be **$2*10^{-4}$ P^{ω}**. The dependence of the crystal efficiency on the phase matching angle, crystal length and spot size is shown in the figures below.

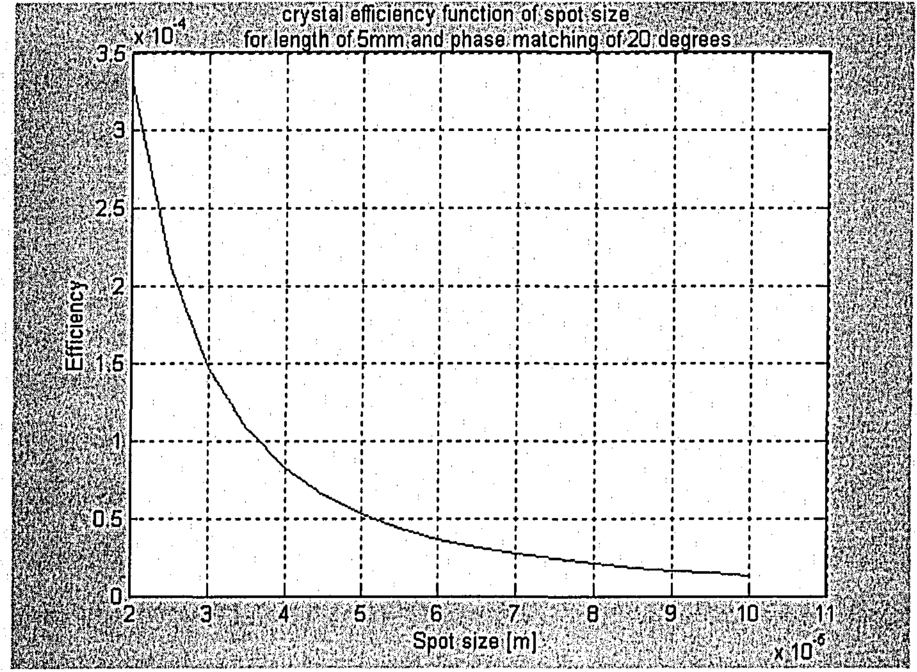

Fig. A-7: Crystal efficiency as a function of spot size

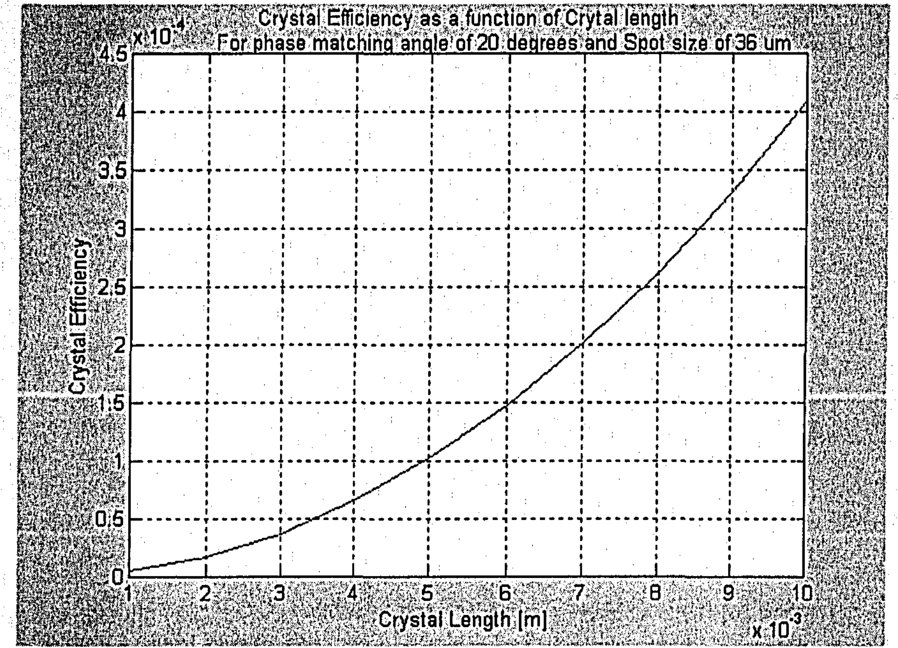

Fig. A-8: Crystal efficiency as a function of crystal length.

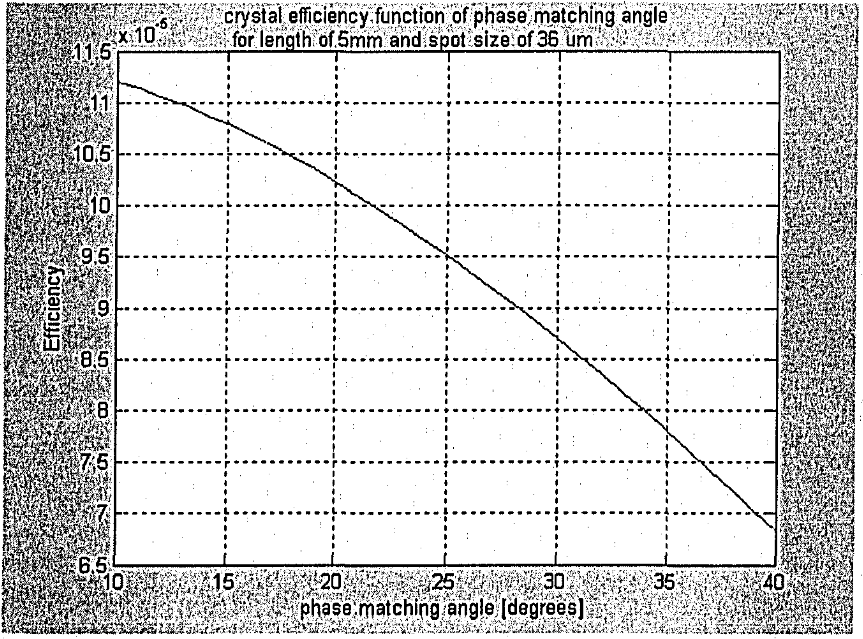

Fig. A-9: Crystal efficiency as a function of phase matching angle.

Appendix B

B.1. Code for first and second order autocorrelation.

```
%%%% Generates a Gaussian pulse %%%%%%%%
clear all
a = 1;                                  % unbalance between the two arms
A = 0;                                  % chirp parameter
f = 32;                                 % frequency = 32HZ
Wo = 2*pi*f;
T_S = 1/(2*2*pi*f);                     % sampling period
F_S = 1/(T_S);                          % sampling rate
t = [-150:T_S:150];                     % setting up the time axis
t0 = 50;                                % pulse width
tg = t0/sqrt(2*log(2));
x = exp(-(1+i*A)*(t./tg).^2);           % chirped pulse

figure(1)
plot (t,x);
ylabel('amplitude')
title('Gaussian function')
xlabel('Time (sec)')
grid


%%%% Calculate the signal S1(tao) and G1(tao) which is due to linear
absorption (First order autocorrelationG1(tao) = < E(t)E*(t-tao)>,
which is just the autocorrelation function xcorrin matlab. %%%%

G1 = xcorr(x,conj(x));                       %% xcorr delays by all tao
G1 = G1./length(x);                          %% Normalized the y axis.

tao=1:length(G1);
S1 = 1 + real(G1.*exp(-j*f*2*pi.*tao.*T_S));

ttt1 = -(length(G1)-1)/2:-1;                 %% Setting up the time axis
ttt2 = 0:length(G1)/2;                       %% so that the the signal
peaks at zero delay
tt = [ttt1,ttt2]*T_S;

figure(2);
plot(tt,G1);
title('G1');
grid

figure(3);
plot(tt,S1);
title('S1');
grid


%%% Calculate F2(Tao) which is the second order autocorrealation
function %%%
```

```
F2 = xcorr((x).^2,conj((a.*x).^2));          %% xcorr delays by all tao
F2 = F2./length(x);                           %% normalizse the y axis

figure(4);
plot(tt,F2);
title('F2');
grid


%%%% calculate F1(tao), this requires some manipulation of the equation


E3 = abs(x.*conj(x)).*x;
F1 = xcorr(E3,a.*x);
F1 = F1./length(x);

figure(5);
plot(tt,F1);
title('F1');
grid


%%%%% Calculate G2(tao) %%%

G2 = xcorr(abs(x).^2,abs(a.*x).^2);             %% xcorr delays by all tao
G2 = G2./length(x);                              %% Normalized the y axis.

figure(6);
plot(tt,G2);
title('G2');
grid


%%%% Calculate S2(tao) %%%%

tao = 1:length(G2);
S2 = 1+ 2.*G2+ 4.*real(F1.*exp(-j*f*2*pi.*tao.*T_S))+ real(F2.*exp(-
j*f*4*pi.*tao.*T_S));

figure(7);
plot(tt,S2);
title('S2');
ylim([0.8,1.8])
grid
```

B.2. Code for dispersion and chirp

```
% Temporal broadening of a Gaussian pulse using equation from Ghatak
% ch.15 and 6
% Using the values given in Ghatak, the temporal variation of the
% Electric field of an optical pulse is calculated for varying values
% of Z.

%%%%%%%%%%%%%%%%%%%%%%%%%%%%%%%%%%%%%%%%%%%%%%%%%%%%%%
%% constants %%
%%%%%%%%%%%%%%%%%%%%%%%%%%%%%%%%%%%%%%%%%%%%%%%%%%%%%%
```

```
Eo = 1;                       % Amplitude
lamdao = 0.85e-6;             % center wavelenght[m]
wo =0.217;                    % center frequency [rads/fs]
ko = 1.11e7;                  % propagation constant
vg = 2.04e-7;                 % group velocity[m/fs]
To = 50;                      % initial pulse width in [fs]
alpha = 3.26e5;               % units [fs^2/m]
Z =0 ;                        % propagation distance [m]. This is varied from
                              % 0 to L
t = [-800:5:1000];            % time

%%%%%%%%%%%%%%%%%%%%%%%%%%%%%%%%%%%%%%%%%%%%%%%%%%%%%%%%%%%%
%% Equations %%
%%%%%%%%%%%%%%%%%%%%%%%%%%%%%%%%%%%%%%%%%%%%%%%%%%%%%%%%%%%%

sigma = (2*alpha*Z)/To^2;              % unitless
k = sigma/((1+sigma^2)*To^2);          % units [fs^-2]
tz = sqrt(To^2*(1+sigma^2));           % units [fs]

phizt = (wo.*t)+(k.*(t-Z/vg).^2)-(1/2*atan(sigma));

Ezt = (Eo/(1+sigma^2)^(1/4)).*exp(-((t-Z/vg).^2)./tz^2).*exp(i.*(phizt-
ko*Z));

Y = real(Ezt);
t1 = t./To;

%%%%%%%%%%%%%%%%%%%%%%%%%%%%%%%%%%%%%%%%%%%%%%%%%%%%%%%%%%%%
%%plot%
%%%%%%%%%%%%%%%%%%%%%%%%%%%%%%%%%%%%%%%%%%%%%%%%%%%%%%%%%%%%

plot(t1,Y);
grid on;
ylim([-1,1]);
```

B.3. Dispersion compensation

```
% Dispersion compensation of a gaussian pulse
% After propagating through a section fo fiber, the input pulse becomes
% broadened and chirped. If this chirped pulse is then propagated
% through a section of fiber of length L' and dispersion α' then the
% output pulse can be recompressed.
% in this simulation the L' is varied for different length os smf28 to
% see the effects.

lamda0 = 1550;                % wavelenght [nm]
D = 1.27e4;                   % Dispersion Coefficient of NEFERN EDF
                              % [fs^2/m]
Dprime = -2.2e4;              % Dispersion coefficient of reg. fiber
                              % [fs^2/m]
L =1;                         % lenght of smf28 [m]
Lprime = 0;                   % Lenght of EDF [m]
E0 = -1;
```

```
t=[-1000:9.5:1000];
To = 100;                        % pulse with in fs
wo = 1.22;                       % frequency [rads/fs]

E =
(E0*(sqrt(To^2/(To^2+2*i*(D*L+Dprime*Lprime))))).*exp(i.*wo.*t).*exp(-
t.^2./(To^2+2*i*(D*L+Dprime*Lprime)));

Y = real(E);
plot(t,Y);
```